Miniaturized Ultrasonic Transducers for Wearable and Implantable Applications

by

Alp Timuçin Toymuş

A Dissertation Submitted to the
Graduate School of Sciences and Engineering
in Partial Fulfillment of the Requirements for
the Degree of

Doctor of Philosophy

in

Mechanical Engineering

KOÇ ÜNİVERSİTESİ

June 11, 2025

Miniaturized Ultrasonic Transducers for Wearable and Implantable Applications

Koç University

Graduate School of Sciences and Engineering

This is to certify that I have examined this copy of a doctoral dissertation by

Alp Timuçin Toymuş

and have found that it is complete and satisfactory in all respects,

and that any and all revisions required by the final

examining committee have been made.

Committee Members:

Assist. Prof. Levent Beker (Advisor)

Prof. Erdem Alaca

Assist. Prof. Murat Kuşcu

Assist. Prof. Erdinç Tatar

Assist. Prof. Hasan Uluşan

Date: ______________________

To my parents Suna and Kazım,

my little brother Gökberk,

and my one & only Ecem...

ABSTRACT

Miniaturized Ultrasonic Transducers for Wearable and Implantable Applications
Alp Timuçin Toymuş
Doctor of Philosophy in Mechanical Engineering
June 11, 2025

While skin-integrated electronics have revolutionized healthcare by enabling continuous monitoring, extracting critical physiological information from deeper within the body remains a significant challenge for existing wearable and implantable devices. This dissertation demonstrates how decades-old ultrasound technology can be effectively integrated into wearable and implantable medical devices to access information hidden beneath the skin.

We first evaluated state-of-the-art ultrasonic transducer technologies through fabrication and characterization of single element piezoelectric transducers (bulk PZT versus PVDF-TrFE-based PMUTs) to assess their feasibility for wearable applications. Building on this foundation, we developed a fully integrated wearable ultrasonic patch for continuous bladder volume monitoring, featuring efficient air-backed transducers with a 6 dB bandwidth of 37.9%. These air-backed transducers with precisely laser-micromachined matching layers enabled accurate measurements even with low driving voltages (± 15 V), offering a important advantage for long-term use with batteries. The device was initially validated in-vitro with a mean relative error of 14.85% across various shaped flasks mimicking diverse bladder geometries in clinical scenarios, followed by in-vivo measurements on five healthy volunteers with a mean relative error of 11.17% across various bladder shapes and volumes ranging from 100 to 800 mL.

To further improve the wearability and user comfort, we introduced electronics-free ultrasonic tags, drastically reducing on-body footprint by relocating the electronics and battery off-body. This allowed for an on-body footprint as low as 0.5 cm^2, a major advantage compared to the latest wearable ultrasound devices that often exceed 25 cm^2 in total size, with transducers covering only a very small por-

tion of that area. Furthermore, such an inductively coupled approach enabled the development of a smart ultrasonic contact lens for ophthalmologic ultrasound for the first time.

Lastly, to extend the functionality of wearable ultrasonic devices beyond traditional diagnostics, we established an ultrasound-based passive communication method for medical implants, utilizing simple pulse-echo measurements. The proof-of-concept 1 cm^2 ultrasonic antenna revealed a 168 Hz/pF shift at a 100 Hz measurement rate during in-vitro underwater measurements.

The devices and methodologies presented in this dissertation establish a foundational framework for next-generation wearable ultrasound in deep tissue health monitoring.

ÖZETÇE

Doktora Tez Başlığı
Alp Timuçin Toymuş
Makine Mühendisliği, Doktora
11 Haziran 2025

Vücutla uyumlu elektronikler, sürekli takibi mümkün kılarak sağlık hizmetlerinde devrim yaratmış olsa da, vücudun daha derinlerinden kritik fizyolojik bilgi elde etmek, mevcut giyilebilir ve implante edilebilir cihazlar için önemli bir zorluk olmaya devam etmektedir. Bu tez, onlarca yıllık ultrason teknolojisinin, cildin altında gizli bilgilere erişmek için giyilebilir ve implante edilebilir tıbbi cihazlara nasıl etkili bir şekilde entegre edilebileceğini göstermektedir.

İlk olarak, giyilebilir uygulamalar için uygunluklarını değerlendirmek amacıyla, tek elemanlı piezoelektrik dönüştürücülerin (PZT plaka ve PVDF-TrFE PMUT'lar) üretimi ve karakterizasyonlarıyla en güncel ultrasonik dönüştürücü teknolojilerini değerlendirdik. Bu temelin üzerine inşa ederek, sürekli mesane hacmi izleme için, 6 dB bant genişliği %37,9 olan verimli hava destekli dönüştürücülere sahip, tamamen entegre giyilebilir bir ultrasonik yama geliştirdik. Hassas lazerle işlenmiş eşleştirme katmanlarına sahip bu hava destekli dönüştürücüler, düşük sürüş voltajlarında (± 15 V) bile doğru ölçümler sağlayarak, pillerle uzun süreli kullanım için önemli bir avantaj sunmaktadır. Cihaz, klinik senaryolardaki çeşitli mesane geometrilerini taklit eden farklı şekilli şişelerde in-vitro olarak %14,85 ortalama bağıl hata ile, ardından 100 ila 800 mL arasında değişen çeşitli mesane şekilleri ve hacimleriyle beş sağlıklı gönüllü üzerinde in-vivo ölçümlerde %11,17 ortalama bağıl hata ile başlangıçta doğrulandı.

Giyilebilirliği ve kullanıcı konforunu daha da iyileştirmek amacıyla, elektronik içermeyen yeni ultrasonik etiketler geliştirdik; bu, elektronik aksam ve bataryayı vücut dışına taşıyarak vücut üzerindeki alanı önemli ölçüde azalttı. Ultrasonik etiketlerin kapladığı 0,5 cm^2 gibi düşük bir alan, dönüştürücülerin çok küçük bir kısmını kapladığı toplam boyutu 25 cm^2'yi aşan en yeni giyilebilir ultrason cihazlarına kıyasla büyük bir avantajı vurgulamaktadır. Bu sayede oftalmolojik ultrason

için akıllı bir ultrasonik kontakt lensin ilk kez geliştirilmesi mümkün oldu.

Son olarak, giyilebilir ultrasonik cihazların işlevselliğini geleneksel teşhisin ötesine taşımak amacıyla, basit puls-eko ölçümleri kullanarak tıbbi implantlar için ultrason tabanlı pasif bir iletişim yöntemi geliştirdik. Kanıt niteliğindeki 1 cm^2 ultrasonik anten, su altı ölçümleri sırasında 100 Hz ölçüm hızında 168 Hz/pF'lik bir kayma gösterdi.

Bu tezde sunulan cihazlar ve metodolojiler, derin doku sağlığı takibinde yeni nesil giyilebilir ultrason için temel bir çerçeve oluşturmaktadır.

ACKNOWLEDGMENTS

I am very grateful to my supervisor Dr. Levent Beker, who first got me hooked on pursuing full-time research, for giving me the opportunity to work on such an exciting research area, and for his continuous guidance throughout my thesis. I would like to extend gratitude to my thesis committee members Prof. Dr. Erdem Alaca, Dr. Murat Kuşcu, Dr. Erdinç Tatar and Dr. Hasan Uluşan for their support for my dissertation. I would also like to thank to Prof. Dr İskender Yılgör and Emel Yılgör for always having the time to share their invaluable experiences and knowledge. Similarly, I would like to thank to Prof Dr. Hayrettin Köymen, Assoc. Prof. Dr. Baki Karaböce, Dr. Burak Eminoğlu, Dr. Sedat Pala and Dinçay Akçören for their time and support. I learned a lot from them.

I am also deeply grateful to the doctors at Koç University Hospital, who patiently considered our ideas and provided invaluable feedback. Specifically, I wish to thank Prof. Dr. Tufan Tarcan and Assoc. Prof. Dr. Ersin Köseoğlu for their fruitful collaboration on the continuous bladder volume project, and Prof. Dr. Murat Hasanreisoğlu and his team for their insightful discussions on contact lenses.

I would also like to thank to many people from Koç for supporting my work. In particular, thanks to KUYTAM and KUBAM teams; to all Metin Research Group; to Dr. Aziz Koyuncuoğlu, Çağla Selalmaz, Dr. Onur Şenel, Dr. Burak Birkan and Tan Şimşek from n2STAR. Special thanks to Dr. Çağdaş Dağ for the exciting NMR discussions, delicious watermelons and coffees we had together.

I am also very grateful to Dr. Emin İstif, Taher Abbasiasl, Fariborz Mirlou, Abdülkadir Yasin Atik, Emine Bardakçı, Özgür Deniz Temel, Maide Miray Albay, Deniz Aktaş, Dr. Ritu Das, Süleyman Yasin Peker, Dr. Evren Fatih Arkan, and all other current and past members of the BMDL group for their support and friendship.

I was financially supported by TUBITAK BIDEB 2211-A Scholarship during this dissertation. In addition, the projects received funding from TUBITAK through 2232 (grant no. 118C295) and 1002 (grant no. 124E724), and from European Research Council (grant no. 101043119 and 101189448).

There are some people who made this graduate journey so fun. I would like to thank Seçkin Akıncı Hocam for teaching me everything I know about microfabrication and all the conversations we had together. I would also like to thank to Umut Can Yener for the his friendship. I was very lucky to work with him.

When I returned to Turkey, my biggest motivation was being close to my family and friends. I am extremely grateful to my parents Suna and Kazım Toymuş and my younger brother Gökberk Toymuş for their lifetime support. I am also very thankful to my long-time friends & brothers Ömer Abim, Ustam, Hükümdarım, Peren, Balp, Poyraz, Çoban, Tola, Çakmak and Merjoe. Special thanks to El Ziya and Saygın for their friendship and for the imported piezoceramics.

Finally,

Some signals only make sense
when two transducers are in perfect resonance.
Alone, each echo drifts—
half a thought, a question unanswered.
But together, interference becomes harmony,
and noise becomes meaning.
To the one whose frequency matches my own:
the tide continues, but only if you shift by four....

TABLE OF CONTENTS

LIST OF TABLES

LIST OF FIGURES

ABBREVIATIONS

AWG	Arbitrary Waveform Generator
BVD	Butterworth Van Dyke
CMOS	Complementary Metal-Oxide Semiconductors
CMUT	Capacitive Micromachined Ultrasound Transducer
DMF	Dimethylformamide
DRIE	Deep Reactive Ion Etching
ECM	Equivalent Circuit Model
FFT	Fast Fourier Transform
FEM	Finite Element Modeling
ICP	Inductively Coupled Plasma
LDV	Laser Doppler Vibrometer
LIA	Lock-in Amplifier
LUTD	Lower Urinary Tract Dysfunction
PCB	Printed Circuit Board
PECVD	Plasma Enhanced Chemical Vapor Deposition
PDMS	Polydimethylsiloxane
PMUT	Piezoelectric Micromachined Ultrasound Transducer
PVDF-TrFE	Polyvinylidene Fluoride Trifluoroethylene
PZT	Lead Zirconate Titanate
RIE	Reactive Ion Etching
SNR	Signal to Noise Ratio
SPICE	Simulation Program with Integrated Circuit Emphasis
T/R	Transmit and Receive
TOF	Time of Flight
VNA	Vector Network Analyzer

Chapter 1

INTRODUCTION

Over the last decades, the world's population has rapidly grown, placing a huge demand on healthcare systems globally. Traditional symptomatic medicine approaches, which are based on infrequent clinical visits and intermittent measurements, do not provide timely and actionable information. This has led to the emergence of proactive medicine with continuous health monitoring as a key tool to manage chronic diseases, enable early diagnosis, and improve overall quality of life. To truly enable personalized proactive care, the development of new technologies capable of providing continuous and clinically relevant health data is urgently needed [Gambhir et al., 2021].

In order to meet this need, recent advances in soft materials, flexible substrates, and miniaturized sensors have enabled the development of skin-integrated electronics, revolutionizing healthcare through wearables that monitor a range of health parameters. Such devices range from conformal, skin-integrated electronic systems to minimally invasive and fully implantable devices for real-time and continuous monitoring of various health parameters which enable the dynamic capture of physiological, thermal, mechanical, and biochemical information [Koydemir and Ozcan, 2018].

Nevertheless, these devices have mainly focused on surface-level data and missed the critical information from deeper within the body [Lin et al., 2022]. To address this gap, wearable ultrasound technology is a rapidly emerging research field. Despite the promising advancements, the adaptation and translation of these devices remain in their early stages. This is mainly due to the complexity of ultrasound imaging, where the need for high sampling rates and processing speed can lead to significant power consumption, often reaching several hundred milliwatts [Lin et al., 2023]. Moreover, the reliance on bulky batteries to power up such circuits presents a grand challenge, requiring frequent replacements and dependence on external sources for recharging.

Addressing these limitations is crucial for unlocking the full potential of wearable ultrasound technology for continuous health monitoring. In this dissertation, we will investigate how decades-old ultrasound technology can be effectively integrated into wearable devices for health monitoring applications, including a demonstrated potential for communication capabilities with implantable medical devices to access information hidden beneath the skin.

1.1 Conventional Medical Ultrasound

The core advantage of ultrasound technology is the use of safe and biocompatible sound waves to visualize internal organs and assess physiological processes, unlike the ionizing radiation used in X-rays or CT scans.

The working principle of an ultrasound system is based on the transmission of sound waves into the body and the detection of their interaction with tissues. As the name suggests, ultrasound implies the use of frequencies that are higher than the audible range (greater than 20 kHz), and most commonly between 1-10 MHz depending on the clinical application and depth and resolution requirements.

While the pulse-echo technique is the basis for diagnostic ultrasound imaging, whereby images are created according to the amplitude of the received (reflected) sound waves, sophisticated signal processing schemes within ultrasound systems can allow for various investigations based on different principles, such as blood flow measurements based on Doppler frequency shifts.

At its core, an ultrasound system consists of several key building blocks for the generation, transmission, reception, and processing of ultrasonic signals. As shown in Figure 1.1, the system can be broadly divided into 4 main sections:

- **Control Unit & Power Management:** This module is the command unit

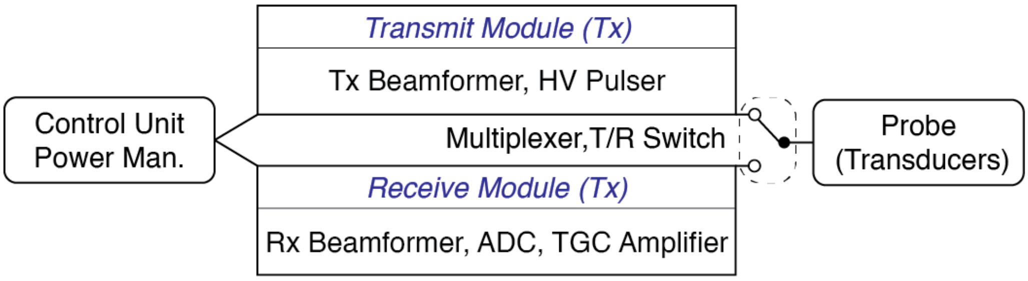

Figure 1.1: Simplified ultrasound system architecture.

of the ultrasound systems. It orchestrates the overall operation, controls the timing of transmit and receive cycles and respective switch operation and provides the necessary power and supply levels to other modules. Depending on the architecture the module is also responsible for data & information transfer.

- **Transmit Module (Tx):** This module is responsible for generating the electrical signals to drive the transducer and produce ultrasound waves. It includes a High-Voltage (HV) Pulser and might also include a Transmit (Tx) Beamformer. The HV Pulser generates high-voltage electrical pulses to drive the transducers. The Tx Beamformer is used to apply time-delays and amplitude apodization to these high-voltage pulses before they reach individual elements within the transducer array. By controlling these timing and amplitude variations across the array, the system can electronically steer and focus the transmitted ultrasound beam.

- **Probe (Transducers):** Probe is the interface between the rest of the ultrasound system and the patient, which is responsible for converting the electrical energy into ultrasound waves during transmission and vica-versa during reception. The probe contains an array of ultrasonic transducer elements which are responsible from this transduction process based on various mechanisms. Various types of probes are customized for specific applications and frequencies.

- **Multiplexer and T/R Switch:** Based on the inputs from the control unit, this module is responsible from the connection of the individual transducer elements to the either the transmit or the receive circuitry. The Transmit/Receive (T/R) switch protects the sensitive low-voltage receiver circuitry from the high-voltages generated in the transmit module during the transmission. Multiplexers are used for addressing the individual transducer elements during transmission and reception phases.

- **Receive Module (Rx):** Lastly, this module captures and processes the weak electrical signals from the transducer elements during reception of echo signals. These signals are typically amplified by Time-Gain Compensation (TGC) amplifiers, which adjust the gain based on the time of flight of the signals. The analog-to-digital converter then converts these analog electrical signals into digital data that can be further processed. Finally, similar to their Tx counterparts, receive (Rx) beamformers apply specific delays and weighting to these signals, allowing for electronic steering and focusing of the receive sensitivity.

The digital data captured by the Receive Module is then subjected to various digital signal processing steps, which depend on the specific ultrasound modality being used (e.g., forming an anatomical image from pulse-echo data or calculating frequency shifts for Doppler information). This processed data is then prepared for display, allowing clinicians to interpret the results in real-time.

Given that the probe and its transducer elements are the essential link to the body through electro-acoustic conversion, it is critical to understand and investigate various transducer technologies for a better evaluation of their adaptability and suitability for wearable and implantable applications.

1.1.1 Piezoelectricity

Due to the dominance of piezoelectric phenomenon in transducer technologies, it is important to establish the foundations of the piezoelectricity. Piezoelectric materials have the ability to mechanically deform when an electric field is applied, and conversely, to generate electric charge when subjected to mechanical deformation. The constitutive equations mathematically describe these coupling by relating the mechanical state of the material to its electrical state [Cochran, 2012].

For a conventional dielectric material with permittivity $\boldsymbol{\epsilon}$ [F/m], electric displacement $\mathbf{D}$ [C/m^2] is related to the electric field $\mathbf{E}$ [V/m] by:

$$\mathbf{D} = \boldsymbol{\epsilon}\mathbf{E} \tag{1.1}$$

In a 1D model of a simple piezoelectric material, electrical polarization $\mathbf{P}$ is related to the strain $\mathbf{S}$ through the piezoelectric stress constant $\mathbf{e}$ [C/m^2]:

$$\mathbf{P} = \mathbf{e}\mathbf{S} \tag{1.2}$$

Therefore, combining (2.5) and (2.6) for a piezoelectric material results with:

$$\begin{aligned} \mathbf{D} &= \boldsymbol{\epsilon}^s\mathbf{E} + \mathbf{P} \\ \mathbf{D} &= \boldsymbol{\epsilon}^s\mathbf{E} + \mathbf{e}\mathbf{S} \end{aligned} \tag{1.3}$$

where $\boldsymbol{\epsilon}^s$ is the permittivity at constant strain. By following a similar procedure, the stress $\mathbf{T}$ [N/m^2] can be expressed as:

$$\mathbf{T} = \mathbf{c}^s\mathbf{S} - \mathbf{e}\mathbf{E} \tag{1.4}$$

where $\mathbf{c}^s$ is the elastic stiffness at constant electric field. These two simple equations describe the fundamental principles of the linear piezoelectric effect. The first equation shows that the electric displacement ($\mathbf{D}$) depends on both the applied electric field ($\mathbf{E}$) and the experienced strain ($\mathbf{S}$) due to an applied stress. The second equation highlight that the stress ($\mathbf{T}$) is related to the strain ($\mathbf{S}$) and the electric field ($\mathbf{E}$). These expressions for $\mathbf{D}$ and $\mathbf{T}$ relate the electrical and mechanical variables in piezoelectric materials, and are expressed in three dimensions by tensors and matrices.

A widely utilized figure-of-merit for the piezoelectric material is the electromechanical coupling coefficient k, which relates the energy delivered to the load to the total energy stored. The efficiency of the intrinsic electromechanical energy conversion by a material is commonly referred to as k^2 [Cochran, 2012].

The performance of a transducer is fundamentally governed by the properties of the piezoelectric material used. An ideal material should offer high piezoelectric coefficients, a suitable dielectric constant, low dielectric and mechanical losses, a high electromechanical coupling factor, good temperature and stress stability, and be manufacturable at a reasonable cost. Historically, lead zirconate titanate (PZT) has been the most widely used piezomaterial as it meets the majority of the desired properties. For applications with top-tier performance requirements demanding even higher piezoelectric coefficients, single-crystals have garnered interest due to their unprecedented piezoelectric coefficients, despite their lower Curie temperature and high costs. On the other hand, piezopolymers might offer interesting properties where only the receive performance of the transducer is critical (e.g. hydrophones) or mechanical flexibility is needed, which cannot be achieved with the rigid and brittle piezoceramics and single crystals. Key properties of selected piezoelectric materials are shown in Table 1.1 [Cochran, 2012].

Table 1.1: Properties of selected piezoelectric materials.

Property (Unit)	PZT-5H	PVDF	PMN-PT
Type of material	'Soft' ceramic	Polymer	Single crystal
Coupling coefficient (k_t)	0.52	0.19	0.57
Coupling coefficient (k_{33})	0.75	0.13	0.90
Piezo. strain constant (d_{33}) ($\mathrm{pC\,N^{-1}}$)	590	25	1400
Piezo. voltage constant (g_{33}) ($\mathrm{mV\,m\,N^{-1}}$)	20	230	30
Stiffness (c_{33}^{E}) ($\mathrm{GN\,m^{-2}}$)	160	8.5	140
Density (ρ) ($\mathrm{kg\,m^{-3}}$)	7500	1800	8000
Longitudinal speed (c_L) ($\mathrm{m\,s^{-1}}$)	4600	2200	4040
Acoustic impedance ($Z = \rho c$) (MRayl)	34	3.9	32
Electrical loss tangent ($\tan\delta$)	0.02	0.3	0.01
Relative permittivity ($\epsilon_{33}^{T}/\epsilon_0$)	3430	8.4	3950
Curie temperature (T_c) (°C)	250	120	150

1.1.2 Types of Transducers

Ultrasound waves can be generated by various methods, including piezoelectricity, electrostatic forces and magnetostriction. To date, piezoelectricity has been the predominant mechanism for ultrasound wave generation, where certain materials have the ability to generate electric charge when subjected to a mechanical stress through the direct piezoelectric effect, and to undergo mechanical deformation when an electric field applied, namely, the indirect piezoelectric effect. When coupled with a careful structural design and a medium of interest, this electromechanic conversion can further be utilized for acoustic wave generation, making the transducers responsible for an electroacoustic transduction mechanism.

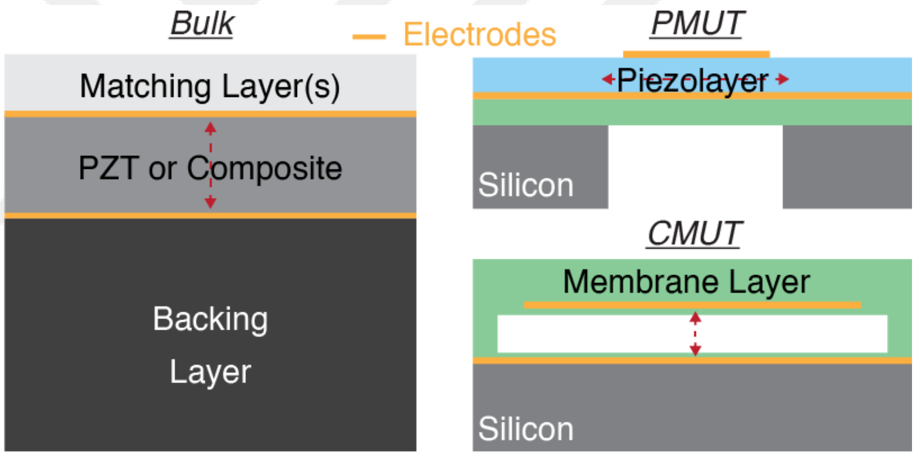

Figure 1.2: Types of transducers used in diagnostic ultrasound: Bulk, PMUTs, CMUTs.

The most common ultrasonic transducers utilize bulk piezoelectric materials, primarily piezoceramics or their piezocomposites. Among these, PZT ceramics have been a key material in this technology. Ultrasound waves can be generated in a basic form by dicing bulk PZT pieces into the desired geometry and sandwiching them with electrodes. Due to historical interest, decades of optimization, and the demand for high performance, bulk piezoelectric transducers represent a mature technology for electroacoustic transduction and are used in the majority of medical ultrasound probes. However, challenges remain, particularly in fabricating very high-frequency transducers (where elements become extremely small and fragile), creating arrays with a high number of elements requiring precise spacing and numerous electrical interconnects, using passive layers (e.g. acoustic matching and backing layers) to control the bandwidth and achieving seamless integration with complex drive/receive electronics [Shung and Zippuro, 1996].

Over the last two decades, MEMS-based micromachined ultrasonic transducers (MUTs) have emerged as transformative alternatives to overcome the challenges of bulk piezoelectric technologies such as labor-intensive fabrication processes, CMOS-compatibility and the bulky structure with the need for additional layers for acoustical matching and backing layers. MUTs utilize lithographically defined thin membranes and operate via either capacitive (CMUT) or piezoelectric (PMUT) transduction mechanisms, both of which have attracted significant research interest and are illustrated in Figure 1.2. CMUTs, which rely on electrostatic forces for operation, offer broad bandwidth and are suitable for applications requiring dense array integration [Joseph et al., 2021]. However, the small gap required for electrostatic actuation in CMUTs introduces additional fabrication challenges [Gijsenbergh et al., 2019], while their non-linear characteristics raise concerns about the acoustic power output needed for deep imaging applications [Sadeghpour et al., 2022]. Additionally, the dependence on high DC bias voltages creates electrical interfacing issues and limits their practicality [Moisello et al., 2024]. In contrast, PMUTs utilize piezoelectric thin films and offer lower power requirements, greater design flexibility, and a simpler fabrication process [Moisello et al., 2024]. These advantages position PMUTs as a promising alternative for next-generation ultrasonic transducers [Roy et al., 2023], [Wong et al., 2024].

1.2 Wearable Ultrasound

Wearable ultrasonic transducers emerged as a transformative technology in the field of wearable medical devices. Unlike conventional ultrasound probes, these wearable devices have significantly smaller form factors, enhancing portability and ease of use. By leveraging cutting-edge materials and engineering, they could offer performance levels that are on par with conventional ultrasound probes. In addition, the flexibility of these devices enable the conformability on the skin and seamless integration into patients' lives [Huang et al., 2024]. Within a remarkably short time span, the demonstrated applications for wearable ultrasonic devices include conventional ultrasonography-based imaging, stimuli-responsive drug delivery, neuromodulation and wireless power transfer to and communication with medical implants [Zhang et al., 2023]. Despite the focus of this dissertation on diagnostics and communication applications; the developed technological platforms are also applicable to therapeutics and power transfer (Figure 1.3).

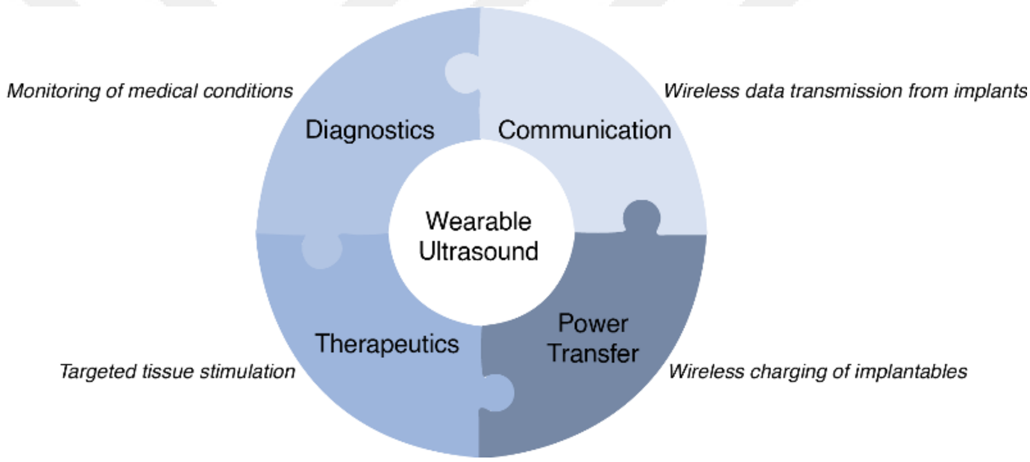

Figure 1.3: Application fields of wearable ultrasound technology.

1.2.1 Motivation in Diagnostics

Ultrasound imaging technology has become an indispensable tool in clinical procedures over the last few decades, owing to its cost-effectiveness, safety, versatility and convenience. However, conventional ultrasound probes have been characterized by their bulky sizes, dependency on skilled operators and clinicians, and their confinement to clinical settings to provide snapshots of the health conditions of the patients. These inherent limitations have attracted researchers for potential innovations in the field and have led to recent breakthroughs in materials design and advanced fabrication techniques [Lin et al., 2023]. These achievements have given rise to a new era in ultrasound technology: the development of wearable ultrasound devices.

One of the most important characteristics of wearable ultrasound technology is its ability to remain in a fixed position on the body without requiring constant manual intervention from an operator. This not only eliminates the need for skilled personnel to hold the device in place but also opens up new possibilities for prolonged and uninterrupted monitoring. Patients could benefit from continuous ultrasound monitoring without being tethered to a stationary device or constrained by the limitations of operator availability. The ability to seamlessly integrate ultrasound technology into wearable devices has the potential to revolutionize healthcare delivery, offering personalized and proactive solutions for patients while simultaneously alleviating burdens on healthcare providers and clinical researchers [Huang et al., 2024].

1.2.2 State-of-the-Art in Wearables

Although the idea of and the interest in flexible/conformal is not new, the field has witnessed significant advancements over the past five years [Huang et al., 2024]. As can be expected, these works build upon conventional ultrasound technologies by adapting them to meet the unique requirements of wearables such as skin conformability, biocompatibility, and low weight [Zhang et al., 2024].

Early efforts in wearable ultrasound primarily focused on amplitude-mode (A-mode) ultrasound. This technique involves transmitting ultrasonic pulses and receiving echo signals from individual transducer elements. A pioneering example came from the Xu group at UCSD, who developed an island-bridge structure combining rigid piezoelements with serpentine electrical interconnects and stretchable silicone layers. This innovative design led to the first demonstration of wearable blood pressure monitoring [Wang et al., 2018]. Subsequently, a similar device architecture was adapted by another group to create a wearable Doppler device for carotid artery blood flow monitoring [Wang et al., 2021b]. Building on these foundational advancements, the Xu group at UCSD leveraged their inherently flexible and stretchable ultrasonic devices to report a range of exciting applications, including continued progress in blood pressure monitoring [Zhou et al., 2024b], cardiac imaging [Hu et al., 2023a], and most recently, transcranial volumetric imaging [Zhou et al., 2024a]. Table 1.2 provides an overview of the most recent works in this field.

Despite these advancements, devices based on flexible and stretchable ultrasonic transducer arrays faced two significant challenges. Firstly, they often encountered resolution issues and image artifacts. These problems arise because the exact positions of transducers on dynamic and curvilinear skin surfaces are difficult to ascertain when the device conforms to the body. While researchers have explored solutions like 3D scanning or advanced correction algorithms in proof-of-concept studies, these approaches limit practicality and scalability, and increase device complexity [Wang et al., 2022]. More importantly, even with conformal transducers, nearly all of these demonstrations relied on wired connections to benchtop equipment for high voltage excitation, low voltage receive and subsequent signal processing, severely limiting their potential for true wearability and continuous monitoring.

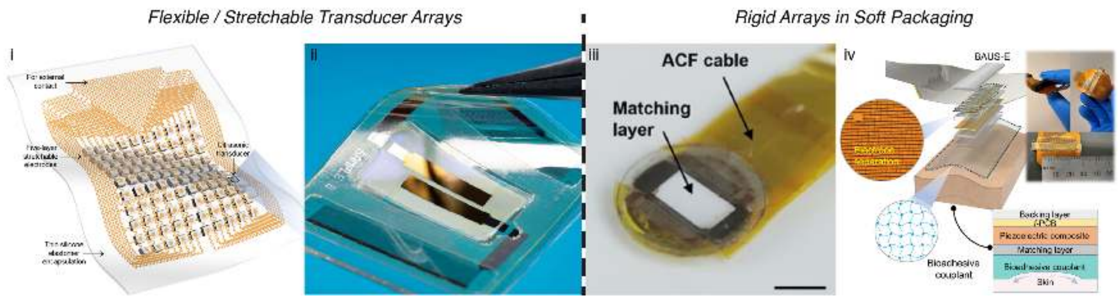

Figure 1.4: Selected representative transducer architectures: (i) Island-bridge structure of UCSD [Hu et al., 2018], (ii) Piezopolymer based fully flexible structure from TNO [van Neer et al., 2024], (iii) Rigid probe structure embedded in soft silicone from MIT-1 [Du et al., 2023], (iv) Rigid probe embedded in soft silicone and bioadhesive hydrogels from MIT-2 [Liu et al., 2024a]. All images are produced with the license creative commons attribution 4.0 (CC BY 4.0).

To address the element-localization problem, two research groups from MIT proposed using rigid transducer arrays encased in soft, biocompatible packaging. One demonstration included a conformable breast patch designed to monitor breast cysts and tumors. This device featured a unique design tailored to the breast's geometry and a movable rigid probe; however, it still required wired connections to an external benchtop instrument and an operator to manually navigate the device across the breast surface [Du et al., 2023]. The same research group also developed a conformable patch for continuous bladder volume monitoring [Zhang et al., 2024]. Although this device resolved the operator dependency for examination, it was bulky (approximately 20x10 cm), still required wired connections, and lacked autonomous algorithms for bladder volume calculations. The second MIT group pursued a similar approach, developing a wearable imaging patch that combined a rigid transducer array with a soft bio-adhesive for long-term organ imaging [Wang et al., 2022]. They successfully demonstrated B-mode imaging of the heart, lungs, and stomach and later extended this technology to ultrasound elastography for liver stiffness monitoring [Liu et al., 2024a]. While these devices showed improved performance due to the rigid transducer array, they all still required external equipment for operation and signal processing, rendering them incapable of continuous, throughout-the-day monitoring.

Very recently, the UCSD group proposed a significant step towards solving the grand challenge of wired connections. They developed a wearable electronics board that enables wireless operation and incorporates machine-learning algorithms for data analysis. However, their demonstrations have so far focused on blood pressure [Lin et al., 2023] and muscle activity monitoring [Gao et al., 2024], and have not yet achieved continuous monitoring of deep organs like the bladder volume, as previously demonstrated with benchtop connections. A fully wearable device was also demonstrated by a group in Shenzhen, however, the device was designed for therapeutic applications and not capable of diagnostics [Zou et al., 2024]. Moreover, compared to the transducer footprints of ~ 1 cm^2, the footprint of the board can take up to ~ 25 cm^2, harming long-term wearability and user comfort.

In conclusion, despite notable advancements in conformal transducer architectures, most current wearable ultrasonic devices used for diagnostics still necessitate external connections to benchtop instruments for operation. This critical limita-

Table 1.2: Recent wearable ultrasound transducer demonstrations.

Integration	Applications	Group
Wired to benchtop	Bladder volume	MIT-1 [Zhang et al., 2024]
	Blood pressure, imaging	TNO [van Neer et al., 2024]
	Elastography	MIT-2 [Liu et al., 2024a]
	Organ imaging	MIT-2 [Wang et al., 2022]
	Breast imaging	MIT-1 [Du et al., 2023]
	Doppler	Tsinghua [Wang et al., 2021b]
	Cardiac imaging	UCSD [Hu et al., 2023a]
	Blood pressure	UCSD [Zhou et al., 2024b]
	Transcranial monitoring	UCSD [Zhou et al., 2024a]
On-body electronics	Sonodynamic therapy	Shenzhen [Zou et al., 2024]
	Blood pressure, diaphragm	UCSD [Lin et al., 2023]
	Diaphragm, muscle	UCSD [Gao et al., 2024]

tion restricts their full wearability and prevents them from providing continuous ultrasonic monitoring.

1.2.3 Potential for Communication with Medical Implants

In modern healthcare, implantable medical devices play a vital role in monitoring clinical conditions and delivering targeted therapies to patients. These implants fall into two general categories: wired and wireless solutions, each with unique benefits and drawbacks. Wired implants, such as defibrillators and pacemakers, require external connections via open wounds, increasing the risk of infection and contamination. On the other hand, wireless alternatives—such as neuro stimulators and glucose monitors—have attracted greater interest due to their capacity to reduce these complications and offer continuous monitoring and assistance [Boutry et al., 2019].

While EM-based techniques serve as the primary method for both data transmission and energy delivery in most wireless implantable medical devices, it comes with its drawbacks. Customized receiving units for sensors limit scalability, while concerns about safety regulations for electromagnetic waves in the GHz range and tissue absorption persist [Maini et al., 2024]. These factors also impact the depth at which the implantable device can effectively communicate with an external interrogator. A new era of implantable medical devices has emerged to address the limitations associated with electromagnetic coupling, harnessing the power of ultrasound (US) instead of EM waves. This approach offers several advantages, including higher power levels and deeper tissue penetration without posing harm to the patient. Unlike EM waves, US enables wireless power and data transfer through pressure waves with millimeter and submillimeter wavelengths, making it well-suited for miniaturized implants. For instance, while 2-GHz EM waves have a wavelength of 25 mm, 2-MHz US waves have a much shorter wavelength of 0.75 mm, facilitating efficient coupling to small implants [Sonmezoglu et al., 2021].

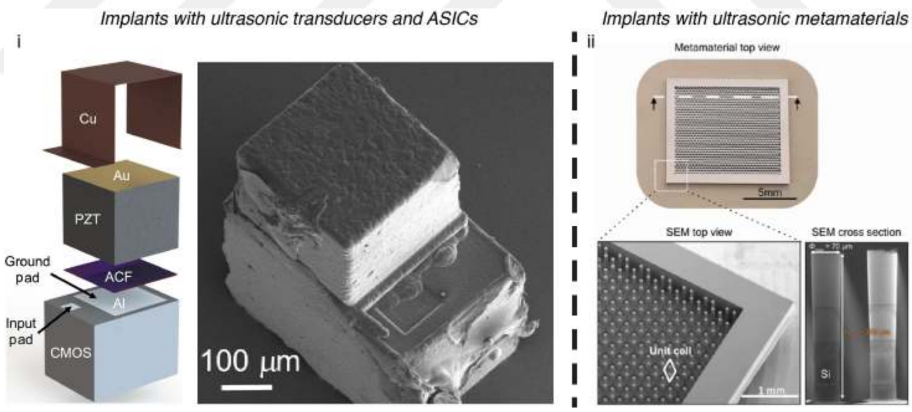

Figure 1.5: Selected representative implant architectures: (i) Piezoelement with ASIC for temperature sensing from Columbia [Shi et al., 2021], (ii) Micromachined Si based ultrasonic metamaterial from ETH Zurich [Maini et al., 2024]. All images are produced with the license creative commons attribution 4.0 (CC BY 4.0).

Building upon these advantages, a new generation of implants has emerged, utilizing ultrasound for both power delivery and communication. Among these, three primary architectures can be distinguished: first, implants that employ piezoelements for data and power transfer, with application-specific integrated circuits managing control and regulation; second, implants designed as stimuli-responsive acoustic metamaterials, which enable remote sensing by altering their reflection coefficient in response to changes in a physical parameter; and third, ASIC-free passive load-coupled piezoelements, an emerging approach that leverages variations in acoustic reflection coefficients of the piezoelement based on changes in the electrical impedance of the load. A brief overview of the notable works are provided in Table 1.3.

Table 1.3: State-of-the-art implant strategies with ultrasonic communication.

Architecture	Applications	Group
Piezo & ASIC	Neural recordings	UC Berkeley [Seo et al., 2016]
	Neural stimulator	UC Berkeley [Piech et al., 2020]
	Temperature sensing	Columbia [Shi et al., 2021]
	O_2 sensing	UC Berkeley [Sonmezoglu et al., 2021]
	Gastric recordings	PennState [Meng and Kiani, 2019]
Metastructures	Glucose sensing	Utah Uni. [Farhoudi et al., 2021]
	Temperature sensing	ETH Zurich [Maini et al., 2024]
	pH sensing	Northwestern [Liu et al., 2024b]
	Strain sensing	Huazhong [Tian et al., 2025]
	Press., Temp., pH sensing	Huazhong [Tang et al., 2024]
Piezo & Passive Load	Pressure sensing	Max Planck [Mutlu et al., 2022]
	Pressure sensing	Tsinghua [Wang et al., 2025]

Despite the diversity in these architectural approaches and various successful demonstrations, significant challenges persist. Firstly, ASIC-based solutions inherently require complex CMOS designs, which complicate fabrication and increase overall system complexity. While metamaterial implants aim to address these issues, their highly application-specific nature often prohibits general applicability, necessitating case-by-case material selection and specific physical designs for each scenario. Although the emerging piezoelectric and passive load-based interrogation method offers a platform that appears to resolve these challenges and present broader applicability, current demonstrations primarily utilize amplitude modulation. This modulation scheme is highly susceptible to misalignments, variations in the intermediate acoustic medium, and changes in the distance between the external transducer and the implant.

An ideal sensing solution would therefore eliminate the need for active components, provide scalable fabrication and wide applicability, and offer robust operation capabilities irrespective of environmental or positional factors.

1.3 Objectives

The central goal of this thesis is to advance the field of wearable ultrasound technologies for next-generation deep tissue monitoring by circumventing the need for high-performance electronics and extensive power. The specific objectives of this work are as follows:

- Evaluation of the state-of-the-art ultrasonic transducer technologies and their feasibility from a wearable device perspective by:

  ∗ Design and modeling using established techniques,

  ∗ Fabricating and characterizing single element prototypes of selected technologies.

- Engineering of devices and methodologies that overcome the complexities associated with conventional ultrasound imaging such as number of channels, power-hungry processing electronics and need for operators by:

  ∗ Developing an efficient system architecture that eliminates power hungry electronics and utilizes low-loss ultrasonic transducers,

  ∗ Developing a method to eliminate the need for on-body electronic board and battery.

- Validation of the developed wearable technologies by:

  ∗ In-vitro laboratory setups underwater,

∗ In-vivo on healthy volunteers against gold standard measurements.

- Move beyond the conventional diagnostic functionality of the wearable ultrasound technology by:

∗ Proposing an ultrasonic communication method with medical implants,

∗ Design and modeling of the ultrasonic communication link,

∗ In-vitro demonstration of the proposed link with integration potential to wearable ultrasound.

1.4 Structure

This work consists of six chapters and is organized as follows:

- Chapter 2 investigates the choice of transducer technology used throughout the thesis through the comparative design, fabrication and characterization of single element piezoelectric transducers.[1]

- Chapter 3 details the development of a fully wearable ultrasonic device for continuous and autonomous bladder volume measurements, covering from the clinical need to system engineering to in vitro and in vivo demonstrations.[2]

- Chapter 4 introduces an inductively coupled ultrasonic measurement approach that enhances user comfort by moving integrated circuits and batteries to an external reader. The chapter details the design, modeling, fabrication, characterization, and in vivo applications of the ultrasonic tag concept. [3]

- Chapter 5 details the development of an ultrasound-based passive communication method with medical implants, serving the same goal as Chapter 3,

[1] Adapted in part from [Toymus et al., 2022]

[2] Adapted in part from [Toymus et al., 2024]

[3] Adapted in part from [Beker et al., 2025]

which is to relocate the integrated circuits and batteries to an external reader. The chapter builts on the previous work of the research group and introduces design, equivalent circuit modeling and in vitro demonstration.[4]

- Chapter 6 concludes this work and points out the future steps for the developed platforms.

[4] Adapted in part from [Yener et al., 2025]

Chapter 2

DESIGN, FABRICATION AND PRELIMINARY CHARACTERIZATION OF PIEZOELECTRIC ULTRASONIC TRANSDUCERS

2.1 Introduction

Given the maturity of the bulk piezoelectric transducer technology and low-voltage operation capabilities of PMUTs unlike the high bias voltage required by CMUTs, this chapter will focus on the piezoelectric transducers (both bulk and PMUTs). We will detail the rationale behind the selection of transducer technologies developed in the following chapters. Used materials and fabrication methods are presented for the both types of piezoelectric ultrasonic transducers, along with preliminary characterization methods and respective results for single-element configurations.

2.2 Bulk Piezo Transducer

At the core of modern ultrasound technologies is the ultrasound probe, most of which consists of an array of hundreds of ultrasonic transducers made up of bulk piezoelectric elements. Typically, these transducers utilize high performance piezoceramics which are mainly based on PZT and its composites.

In addition to the piezoelectric coefficients, the acoustic impedance of the materials also significantly affects the performance of the ultrasonic transducers [Shung and Zippuro, 1996]. The specific acoustic impedance value of a medium is related to the opposition of the medium to the propagation of the sound wave, and can be represented as:

$$Z = \rho \cdot c \tag{2.1}$$

where ρ is the density of the medium in kg/m^3 and c is the speed of sound in m/s. The unit of specific acoustic impedance is Rayl (or kg/m^{2}s).

When an acoustic wave travelling in a medium encounters another medium with a different specific acoustic impedance, the incident acoustic wave gets divided into transmitted and reflected waves. The specific acoustic impedance mismatch between these two media directly affects what portion of the incident wave gets to be transmitted to the second medium and therefore, it has a critical rule on the transducer performance.

Since the impedance value of piezoelectric ceramics (e.g. approximately 34 MRayl for PZT) is much higher than that of the body (e.g. approximately 1.5 MRayl for tissue), a large portion of the ultrasound waves is reflected from the ceramic-body interface. For these reasons, efficient transfer of ultrasound waves to the body and rapid damping of the piezoelectric ceramic's vibration are crucial for high resolution in pulse-echo measurements, which are achieved by additional structural layers [Shung and Zippuro, 1996]. In addition to the piezoelectric material, which was introduced earlier, the bulk piezoelectric transducers commonly contain two more structural layers:

- **Matching Layer:** By introducing an acoustic impedance gradient, the matching layer creates an efficient transition between the high acoustic impedance of the transducer and the lower acoustic impedance of the load medium, typically biological tissue, causing less reflections at the boundaries and a higher transmission efficiency.

  Building on earlier approaches, where single matching layers were designed with an acoustic impedance (Z_m) equal to the geometric mean of the piezoelectric element's impedance (Z_p) and the load impedance (Z_w) (i.e., $Z_m = \sqrt{Z_p Z_w}$), it was later shown that the most efficient transducers require a matching layer with a different acoustic impedance, mathematically expressed as [Desilets et al., 1978]:

  $$Z_m = (Z_p Z_w^2)^{1/3} \tag{2.2}$$

Moreover, the thickness of the matching layer should correspond to the quarter of the wavelength ($\lambda/4$) at the center operating frequency. To achieve broader bandwidths, the ultrasound transducers can employ multiple matching layers, often two or three, each with different acoustic impedance characteristics. The selection of materials for these matching layers is based on the desired acoustic impedance and minimal attenuation. These materials are typically polymers (e.g. epoxies) loaded with powders such as alumina to precisely tune their acoustic properties.

- **Backing Layer:** In ultrasonic transducers used for pulse-echo measurements, a backing material is often attached to the rear face of the piezoelectric element. The role of this backing layer is to absorb the energy radiating from the back of the element and to damp its vibrations. When a piezoelectric element is excited, it tends to "ring" or vibrate for a period, which lengthens the pulse duration and degrades axial resolution.

  Ideally, the backing materials should have acoustic impedances similar to that of the piezoelectric materials to maximize energy absorption and minimize reflections back into the element. At the same time, they should have a high acoustic attenuation to dissipate the absorbed energy. Common materials for backing layers include epoxy mixed with heavy nanoparticles such as tungsten.

  While a backing layer improves axial resolution by shortening the pulse and increasing bandwidth, it also reduces the transducer's sensitivity and output power. This is because the energy is absorbed by the backing instead of being radiated forward, creating a trade-off between resolution and sensitivity. In some cases, air-backing is used to maximize energy delivered to the medium, as it eliminates energy absorption at the back of the transducer due to the greater acoustic impedance mismatch at the back of the transducer.

In addition to the properties of piezoelectric and passive materials, the geometry of the transducer is a major factor in the performance of a transducer through the resonance effect. When a piezoelectric material is electrically excited, it undergoes an oscillation around its natural vibration frequencies. The resonance is utilized during operation for efficient electromechanical conversion. In order to prevent energy loss, it is desired to isolate a desired vibration mode of interest around the targeted frequency range [de Jong et al., 1985]. Three most important vibration modes can be seen below:

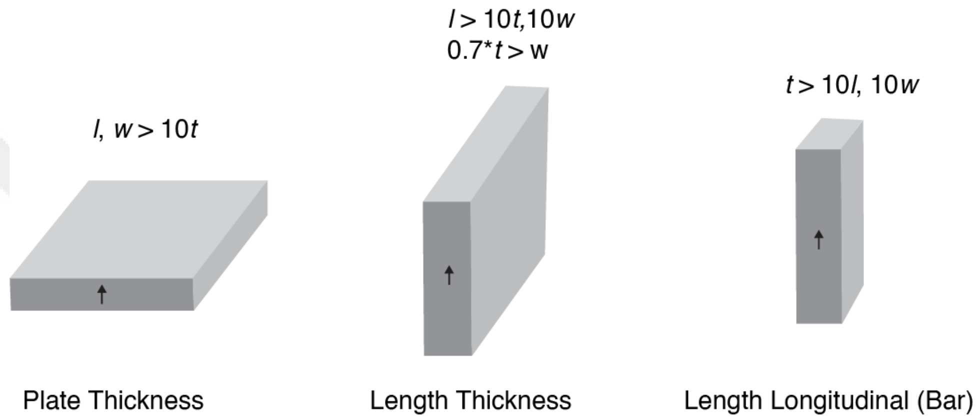

Figure 2.1: Three common vibration modes of bulk piezo transducers.

Most commonly, plates poled and vibrated in their thickness direction with thickness t are driven according to the fundamental (n=1) resonance frequency f_n of the structure:

$$t = n\frac{\lambda_n}{2}, \quad f_n = \frac{nv}{2t}, \quad n = 1, 3, 5, \ldots \tag{2.3}$$

where λ_n is the wavelength corresponding to the n-th resonant frequency $f_n = v/\lambda_n$, and v is the speed of sound in the piezoelectric material. The coupling coefficient for this thickness-mode k_t can be calculated as:

$$k_t = h_{33}\sqrt{\frac{\epsilon_{33}^S}{c_{33}^D}} \tag{2.4}$$

where superscripts S and D stand for constant strain and constant electric displacement boundary conditions, respectively [Cochran, 2012].

Given the complex nature of electromechanical coupling in piezoelectric materials, and additional key components of a transducer such as the matching and backing layers, it is very important to understand and properly model and simulate these structures. A fundamental tool in modeling of ultrasonic transducers is the use of equivalent circuit models which allow for one-dimensional analysis. These models enable the application of standard circuit and network theory using lumped elements and transmission lines with electrical and acoustic ports to describe the transduction.

Mason model is a commonly used equivalent circuit model which accounts for the electromechanical coupling by an ideal transformer and the piezoelectric element as a distributed transmission line as shown in Figure 2.2(a) [Mason, 1964]. With the help of a transmission line equivalent T-network (Figure 2.2(b)), the widely used lumped model is achieved as illustrated in Figure 2.2(c).

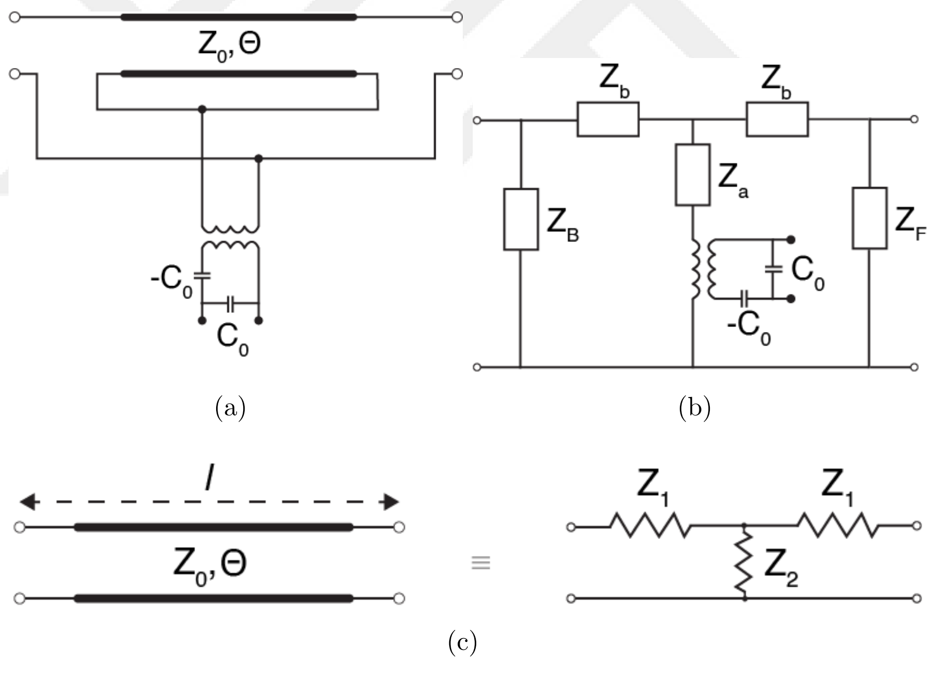

Figure 2.2: Mason's ECM of a thickness-mode ultrasonic transducer.

Mason's ECM model includes a static capacitance (C_0) in parallel with the electrical input terminals to represent the purely electrical capacitance of the piezoelectric crystal. Moreover, to meet the three-port transducer matrix equations, a non-physical negative capacitance ($-C_0$) is used in series with the transformer [Mason, 1964].

To remove the negative capacitance and the transformer and to improve the SPICE (Simulation Program with Integrated Circuit Emphasis)-compatibility of the model, Leach's ECM model utilizes controlled voltage and current sources to represent the complex electromechanical relations. This approach provides an easier implementation in SPICE software [Leach, 1994].

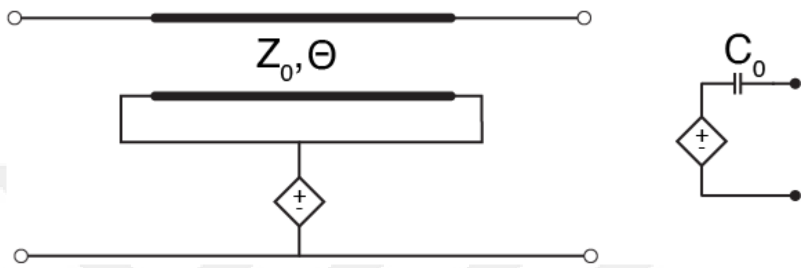

Figure 2.3: Leach ECM with two analogous circuits for electrical and mechanical parts. Coupling is obtained by the two controlled sources.

Beyond Mason and Leach, other important 1D equivalent circuit models do exist, including the Redwood model [Redwood, 1961] and the widely used KLM (Krimholtz, Leedom, Matthaei) model [Krimholtz et al., 1970]. There have also been many works further optimizing these developed models. Nevertheless, it was shown that the 1D equivalent circuit models are fundamentally equivalent, and can be used interchangably for simple thickness mode analysis. [Sherrit et al., 1999].

Building on these fundamental principles, a single-element ultrasonic transducer was designed to develop a fabrication flow, conduct preliminary characterizations and validate against the Leach ECM. In order to simplify the fabrication and accelerate the validation procedure, use of matching and backing layers were avoided. Accordingly, an air-backed PZT plate immersed in water was modeled. A commercially available PZT-5A from American Piezo with a thickness of around 1 mm was utilized. To isolate the thickness mode, a side length of 10 mm was chosen (l>10t).

Utilizing the material properties and dimensions from Table 2.1, parameters required for the implementation of Leach ECM were calculated. For transducer

Table 2.1: Material properties and dimensions used for Leach ECM.

Parameter	Unit	Value
Side length	m	10×10^{-3}
Thickness (t)	m	1×10^{-3}
Density (ρ_{pzt})	kg/m^3	7600
Speed of sound (v_{pzt})	m/s	4080
Relative dielectric constant (e^S)	-	1900
Piezo coefficient h	V/m	9.0×10^8
Quality factor (Q_{pzt})	-	75
Density (ρ_{water})	kg/m^3	1000
Speed of sound (v_{water})	m/s	1480
Density (ρ_{air})	kg/m^3	1.3
Speed of sound (v_{air})	m/s	340

surface area of A, the electrical capacitance C_0 is:

$$C_0 = \frac{e^S \cdot \mathrm{A}}{\mathrm{t}} \tag{2.5}$$

which is followed by the dependent current source multiplier N:

$$N = h \cdot C_0 \tag{2.6}$$

Moreover, following parameters were used for the lossy transmission line representing the thickness-mode transducer:

$$L_{pzt} = \rho_{pzt} \cdot \mathrm{A} \tag{2.7}$$

$$C_{pzt} = \frac{1}{v_{pzt}^2 \cdot L_{pzt}} \tag{2.8}$$

$$R_{pzt} = \frac{2\pi f_0 L_{pzt}}{Q_{pzt}} \tag{2.9}$$

Finally, the air-backing and water load at the front are calculated according to:

$$Z_{air} = \rho_{\text{air}} v_{\text{air}} \cdot \mathrm{A} \tag{2.10}$$

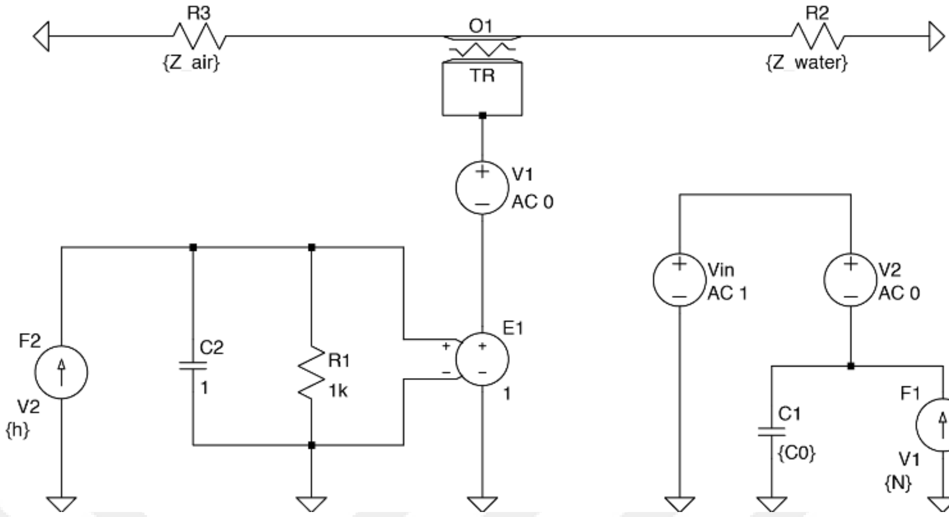

Figure 2.4: Leach ECM implementation of an air-backed PZT plate immersed in water in LTSpice.

According to the calculated parameters, Leach model was built and implemented in LTspice. The circuit schematic is shown in Figure 2.4.

The fabrication process is shown in Figure 2.5(a). The process flow begins with a standard single-sided copper clad FR4 circuit board. The board is laser-patterned for connections and pocketed to enable air-backing of the ultrasonic transducer. Finally, the PZT is soldered above the pocket using a low temperature solder paste (TS391LT, Chip Quik) in a reflow oven (LPKF). Finally, a thin wire is cold-soldered on top of the PZT for connection to the top electrode. The device is then coated with a thin layer of Parylene-C for encapsulation. Cross-sectional optical image of the device after the dicing in the middle following the characterizations demonstrate the succesfull fabrication as shown in Figure 2.5(b).

Following fabrication, an impedance analyzer (MFIA, Zurich Instruments) was used for impedance measurements of the fabricated transducer in the frequency range of 1-3 MHz. As shown in Figure 2.6, there is a good agreement between the calculations from the Leach ECM and the actual measurements, despite the fabrication errors and the variability of the material properties.

The transducer was further evaluated for its pulse-echo response. For the model,

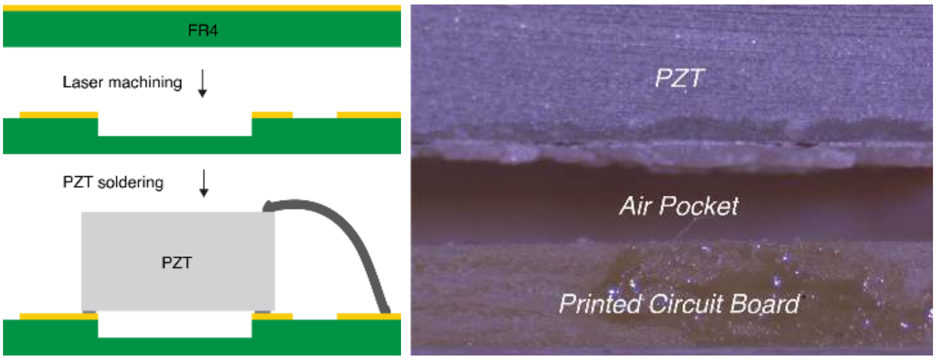

(a) (b)

Figure 2.5: Single element bulk piezoelectric transducer preparation: (a) Fabrication flow, (b) Cross-sectional photo of the fabricated device.

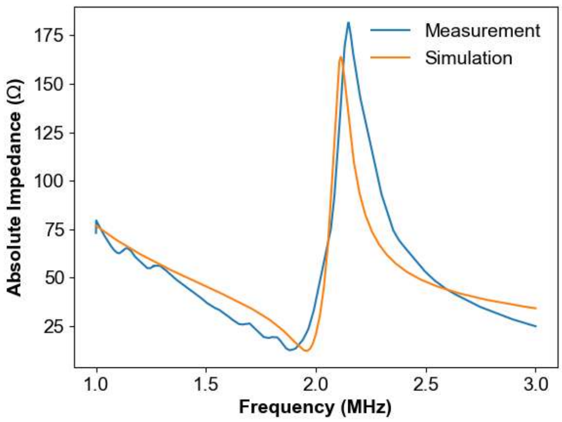

Figure 2.6: Comparison of computed and measured impedance values.

water was added as a lossy transmission line, and a steel reflector was utilized as the load, instead of the water illustrated in Figure 2.4. Similarly, the fabricated transducer was submerged in deionized water and placed against a steel reflector with a high impedance as depicted in Figure 2.7(a). The transducer was excited with a 100 ns long pulse and received echo was displayed and recorded on an oscilloscope. As shown in Figure 2.7(b,c) the measured echoes were in agreement with the simulated waveforms, both revealing a center frequency of around 2 MHz with bandwidths of 12% (measured) and 16% (calculated).

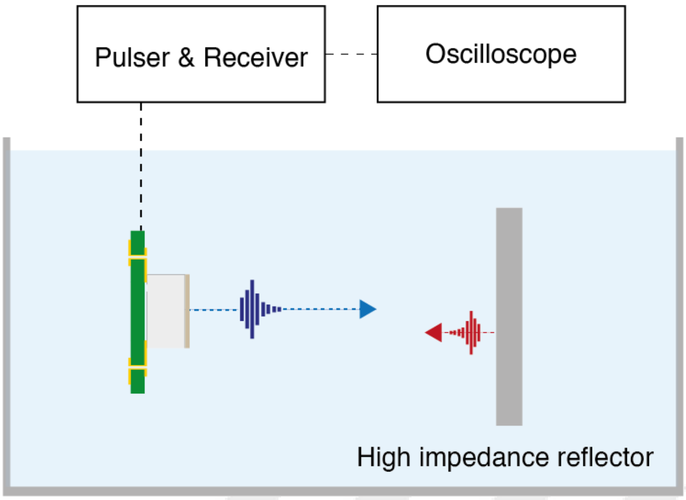

(a)

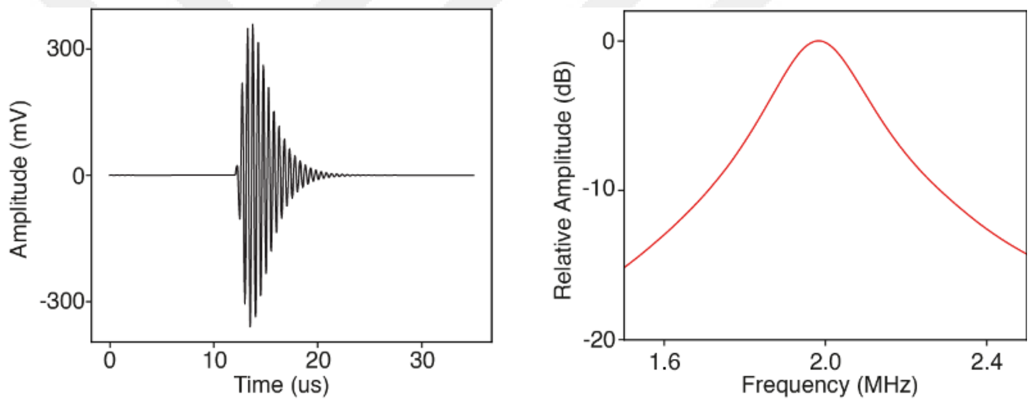

(b)

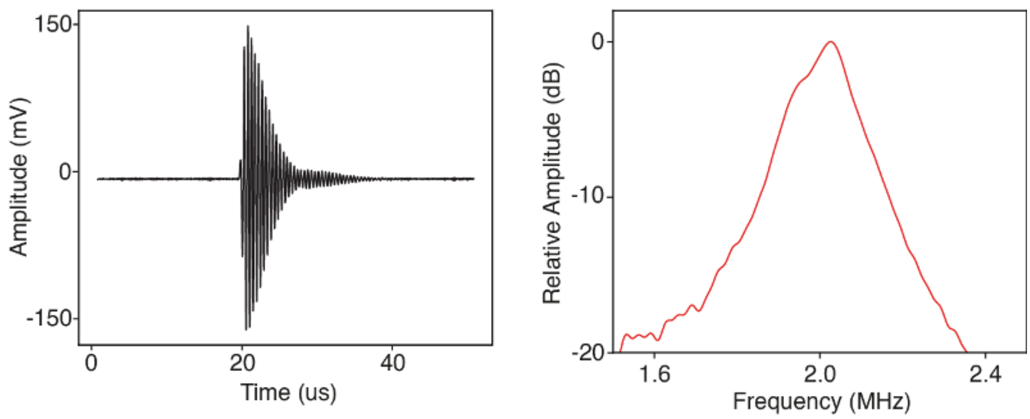

(c)

Figure 2.7: Pulse-echo response of the transducer: (a) Schematic of the pulse-echo setup, (b) ECM results, (c) Actual measurement.

2.3 Piezoelectric Micromachined Ultrasound Transducer

The ultrasonic transducer technology is experiencing a push towards MEMS fueled by the recent advances in microfabrication and growing interest in high-density high-number of element transducer arrays. The ability to fabricate MUTs using microfabrication processes, similar to those used for integrated circuits and other MEMS devices, is a key advantage. Conventional microfabrication techniques are employed to create thousands or even millions of identical, miniaturized transducer elements on a single wafer. This enables the cost-effective manufacturing of dense 1D and 2D arrays with precise element spacing and uniformity, which is essential for advanced beamforming and imaging techniques. More specifically, the interest in PMUTs is driven by a key advantage: compared to CMUTs, which often require high DC bias voltages for optimal performance, PMUTs typically operate at lower voltages, making them more compatible with standard low-voltage CMOS electronics and potentially reducing power consumption [Sadeghpour et al., 2022].

Unlike bulk piezoelectric transducers, which commonly utilize the fundamental vibration mode of the bulk piezoelectric element, MUTs are based on the flexural vibrations of micromachined membranes, which depend on either electrostatic (CMUTs) or piezoelectric transduction mechanisms (PMUTs).

A simple PMUT is a circular membrane with a multi-layer structure consisting of a piezoelectric thin film sandwiched between two electrodes on both sides, placed on a structural layer over a cavity. When an AC voltage is applied across the electrodes, the generated electric field along the thickness of piezoelectric layer results in an in-plane stress in the membrane due to piezoelectricity. The clamped structure of the membrane translates this stress into bending and vibration, which generate acoustic waves into the surrounding medium. In a similar fashion, impinging acoustic waves on the membranes can be detected. A typical PMUT element consists of:

- **Substrate:** PMUTs are most commonly fabricated on a silicon wafer. In addition to its function as a handling layer, the cavity of the membrane could be micromachined into the substrate by wet or dry etching of the silicon.

Moreover, despite not being a part of the vibrating membrane, the thickness of the substrate is critical, since the induced substrate vibrations would absorb the ultrasound energy at the corresponding thickness mode frequency [Giusti et al., 2023].

- **Structural Layer:** Also referred to as the elastic or the device layer, it is commonly the thickest layer of the oscillating membrane and contains the neutral axis of the multi-layered structure, which is crucial for the piezoelectric moment arm. Typically, the device layer Si of a Silicon-on-insulator (SOI) wafer is used. When the process is built on a conventional Si wafer instead of SOI, silicon dioxide (SiO_2), silicon nitride (Si_3N_4) or polyimide is commonly deposited. In addition to the determination of the neutral axis, the properties (density, Young's modulus, Poisson's ratio) of the structural layer is critical in the resonance frequency of the PMUT.

- **Electrodes:** In addition to providing electrical connectivity, bottom electrodes commonly serve as the seed layer for the subsequent piezoelectric thin film deposition. Platinum (Pt) and molybdenum (Mo) are the mostly used films due to their high conductivity, high melting points and chemical stability. Since the piezoelectric films generally require high-temperature processing steps, the electrodes could be further supported by adhesion layers such as titanium. For top electrode, gold (Au), aluminum (Al), or platinum (Pt) are typically used. More importantly, the ratio of top electrode to the membrane size is a major determinant in the coupling performance. 67-70 % coverage is typically used, and actual ratio can be calculated analytically ([Smyth and Kim, 2015], ([Pala and Lin, 2022]) or by FEM ([Mansoori et al., 2023]).

- **Piezoelectric Layer:** Piezoelectric layer is the active layer which is responsible for the operation of the device. When combined with a clamped structure, the piezoelectric operation in 31 direction causes the flexural motion of the membranes. PZT and aluminium nitride (AlN) are the most widely used piezoelectric thin films. Although PZT offer higher piezoelectric coefficients, it requires high temperatures for processing and contains lead. On the other hand, AlN is CMOS-compatible and less-demanding.

In addition to the material properties of the materials used in this multi-layered structure, the thicknesses of these layers and the dimensions of the membranes are the other determining factors in the performance of PMUTs. The design variables based on the material properties and the geometrical dimensions are briefly introduced below [Muralt et al., 2005]:

The *neutral axis* of the multilayered membrane is the stress-free reference plane. For a stack of n layers, with the i-th layer having Young's modulus E_i, Poisson's ratio ν_i, and occupying the region from z_{i-1} to z_i, the neutral axis z_{np} is given by:

$$z_{np} = \frac{1}{2} \cdot \frac{\sum_{i=1}^{n} \frac{E_i(z_i^2 - z_{i-1}^2)}{1-\nu_i^2}}{\sum_{i=1}^{n} \frac{E_i(z_i - z_{i-1})}{1-\nu_i^2}} \tag{2.11}$$

Based on the calculation of the neutral axis z_{np}, the *flexural (bending) rigidity* D of the multilayer diaphragm can be computed as:

$$D = \sum_{i=1}^{n} \frac{E_i}{3(1-\nu_i^2)} \left[(z_i - z_{np})^3 - (z_{i-1} - z_{np})^3 \right] \tag{2.12}$$

The surface mass density μ of the diaphragm is the summation of the mass contributions of each layer, which depend on the density ρ_i and the thickness t_i of the i-th layer:

$$\mu = \sum_{i=1}^{n} \rho_i t_i \tag{2.13}$$

Based on these computed parameters, the resonance frequencies of the plate is given by:

$$f_0 = \frac{\alpha^2}{2\pi a^2} \cdot \sqrt{\frac{D}{\mu}} \tag{2.14}$$

where $\alpha \approx 3.196$ is the eigenvalue constant for the first mode of a clamped circular plate.

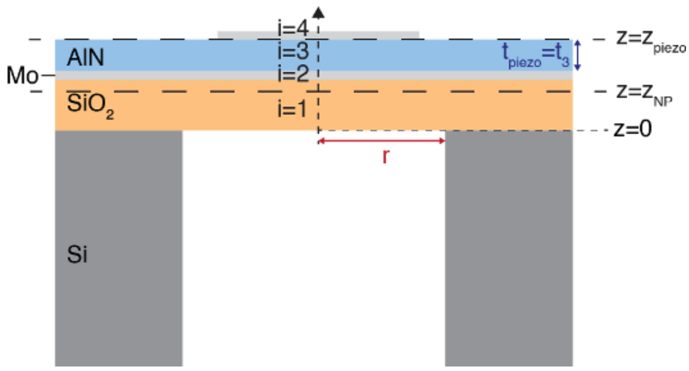

Figure 2.8: Schematic of an representative PMUT with geometrical design parameters.

As mentioned earlier, PMUTs operate based on the transverse mode (31-type) of the piezoelectric layers, where the piezoelectric strain constant is expressed as:

$$d_{31} = \frac{(1-\nu_p)\, e_{31,f}}{E_p} \tag{2.15}$$

where $e_{31,f}$ is the transverse piezoelectric stress constant, ν_p and E_p are the Poisson's ratio and Young's modulus of the piezoelectric layer, respectively. This leads to the following effective piezoelectric coupling coefficient for 31 operation:

$$k_{31}^2 = \frac{2\, d_{31}^2\, e_{31,f}}{\varepsilon_{33}} \tag{2.16}$$

Here, ε_{33} is the permittivity of the piezoelectric material in the polarization direction. The moment arm Z_p, representing the distance between the centroid of the piezo layer and the neutral axis can be computed as:

$$Z_p = z_{\text{piezo}} - \frac{t_{piezo}}{2} - z_{np} \tag{2.17}$$

where z_{piezo} is the top coordinate of the piezo layer, and h_p is its thickness. Based on these computed parameters and 67 % top electrode coverage, Mason ECM sketched in Figure 2.9 can be built for a single PMUT element with the help of Table 2.2 ([Pala and Lin, 2022]). The first transformer represents the electromechanical coupling, whereas the second tranformer represent the mechanoacoustic coupling with an effective acoustic radius $r_{acoustic}$ and corresponding effective surface area of $0.313A_{tot}$.

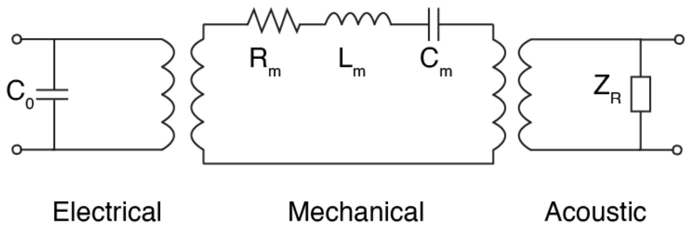

Figure 2.9: Mason ECM of a PMUT membrane.

Table 2.2: Equivalent circuit parameters for the PMUT ECM based on [Pala and Lin, 2022].

Parameter	Value
C_O	$\frac{0.449\epsilon_{33}^T \pi r^2 (1-k_{31}^2)}{h_p}$
$n_{elec-mech}$	$2\pi(0.947)e_{31,f}Z_p$
R_m	≈ 0 (neglected)
L_m	$0.184\pi r^2 \mu$
C_m	$\frac{r^2}{19.226\pi D}$
$r_{acoustic}$	$0.559r$
$n_{mech-acou}$	$\pi r_{acoustic}^2$
R_a	$\approx \frac{(k_{wave} r_{acoustic})^2}{2}$
X_a	$\approx k_{wave} r_{acoustic}$
Z_R	$\frac{\rho_m c_m (R_a + jX_a)}{A_{eff}}$

In order to quantify the feasibility of PMUTs and compare against bulk piezoelectric transducers, a single-element PMUT was designed, fabricated, and preliminarily characterized.

Compared to bulk piezoelectric transducers, where commercial bulk PZT ceramics are widely available with electrodes and already poled, PMUTs commonly require in-house processing or high-cost foundry relations with long delivery dates. Since the piezoelectric materials require custom deposition steps and are not readily available in a cleanroom environment, the first step was to evaluate the piezoelectric materials to choose the most suitable one.

Table 2.3: Thin film piezoelectric materials for PMUTs.

Material	e_{31} (C/m^2)	ε_r	E (GPa)	Fab. Complexity
PVDF	~ -0.01	~ 10	~ 3	Low
PZT	~ -13	~ 900	~ 75	High
AlN	~ -0.9	~ 9	~ 300	Moderate

As shown in Table 2.3, PZT has the highest piezoelectric coefficient within the commonly utilized thin film piezoelectric materials. Even though PZT thin films can be deposited by sol-gel spin coating and sputtering techniques, high temperature annealing steps are required for high quality crystalline films. In addition, Pt electrodes are required as the substrate due their lattice constant, stability and chemical inertness ([Muralt et al., 2005]). On the other hand, despite the popularity of AlN in radiofrequency filter field, the deposition commonly requires custom reactive sputtering systems, which might not be readily available. In contrast, piezoelectric PVDF films do not require high temperature processing steps, and can be simply spin coated. Due to these reasons, PVDF was chosen as the thin film piezoelectric material for rapid prototyping, despite their low piezoelectric coefficients.

Based on the PMUT ECM introduced in Chapter 2, the ECM of the polymer piezo based PMUT was built using Python with the parameters in Table 2.4 ([Shikata et al., 2023]).

Table 2.4: Material properties used for PMUT ECM.

Material	e_{31} (C/m^2)	ε_r	E (GPa)	ν	ρ (g/cm^3)
PVDF	0.05	8	3.6	0.4	1.8
SiO_2	–	–	70	0.17	2.2

A commonly used metric k_{eff} quantifying the degree of electromechanical coupling is used to determine the piezolayer thickness in the multilayered PMUT stack ([Smyth et al., 2017]), whereby the thickness of SiO_2 was kept constant at 1 um considering the in-house deposition capabilities.

$$k_{eff}^2 = \frac{N^2 C_m}{N^2 C_m + C_0} \tag{2.18}$$

The results are displayed in Figure 2.10(a), indicating the use of a 3 um thick PVDF layer. The computed varying resonance frequencies based on varying membrane radii of the stack are displayed in Figure 2.10(b).

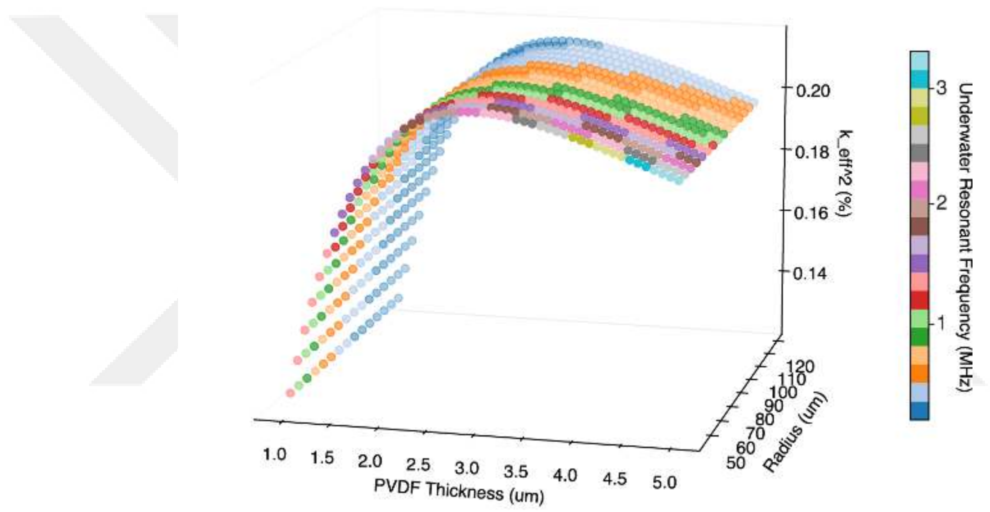

(a)

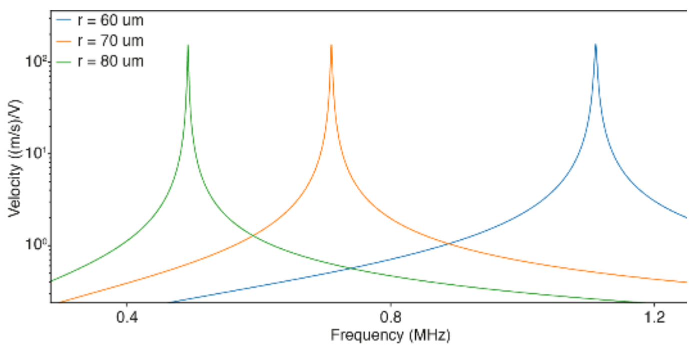

(b)

Figure 2.10: ECM of P(VDF-TrFE) based PMUT: (a) Piezolayer thickness sweep according to k_{eff}, (b) Computed surface velocities vs. frequency.

Despite having low piezoelectric coefficients, the simple processing of PVDF films is of interest across various fields, which is why much work has focused on improving these coefficients. These efforts also led to the development of the P(VDF-TrFE) copolymer that offers enhanced piezoelectric coefficients and improved thermal stability. P(VDF-TrFE) powders from Arkema Piezotech with 20 and 25 mol % TrFE content were already available (Piezotech FC20, Piezotech FC25). Amount of TrFE affects the properties of the copolymer such as the Curie temperature and the piezoelectric coefficient and can be tuned depending on the application requirements. In order to have a homogeneous solution of the the P(VDF-TrFE) powders suitable for spin coating, the followed procedure was follows:

Initially, the desired amount of the solvent N,N-Dimethylformamide (DMF) was transferred to a vial using a glass pipette under a fume hood. According to the determined weight ratio of the solution, desired amount of the powder was poured into the vial with DMF using a spatula and intermediate mixing (e.g. ultrasonication). After placing a magnetic stirring bar inside the vial, the solution was put on a hot-plate for heat-assisted mixing for 3 hours at 80°C with a stirring speed of 450 rpm (Figure 2.11). Lastly, the prepared solution was filtered with a 0.45 μm PTFE filter attached to a syringe to remove any insoluble particles present in the solution and achieve a better uniformity of the final film.

(a) (b)

Figure 2.11: P(VDF-TrFE) solution preparation: (a) P(VDF-TrFE) powders from Arkema, (b) Prepared solution in DMF.

Prior to the fabrication of PMUTs, the performance of the prepared thin films was evaluated by Laser Doppler Vibrometer measurements of a simple cantilever structure (Figure 2.13(a)). Initially, the cantilever structure was fabricated on a Si die with a stack of a Chromium (Cr)/Aluminium (Al)/ Cr bottom electrode, a few µm thick P(VDF-TrFE) piezoelectric film and a Cr/Al top electrode. Following the fabrication, the P(VDF-TrFE) was annealed around its Curie temperature (140°C) to improve the crystallinity and the piezoelectric response.

(a) (b)

Figure 2.12: Poling of P(VDF-TrFE): (a) Photo of the high-voltage setup, (b) Top-view showing the connections.

Lastly, before the characterization step, since as-deposited films do not exhibit piezoelectricity, poling process is required. A high electric field must be applied to align the dipoles of the polymer structure for net polarization and to observe a macroscopic piezoelectric effect. To achieve this, a high-voltage DC power supply (Stanford Research System) was used for contact poling. Electrical connections were established with the help of a probe station. Probe tips were placed onto the pads, and DC supply was connected to the probe station. Although AC poling is the preferred method, DC poling (75 V$\cdot\mu$m^{-1}) was utilized due to its availability.

As illustrated in Figure 2.13(b), the in-plane stress produced by V_{can} due to e_{31} coefficient of the piezoelectric film bends the cantilever, assuming one-end to

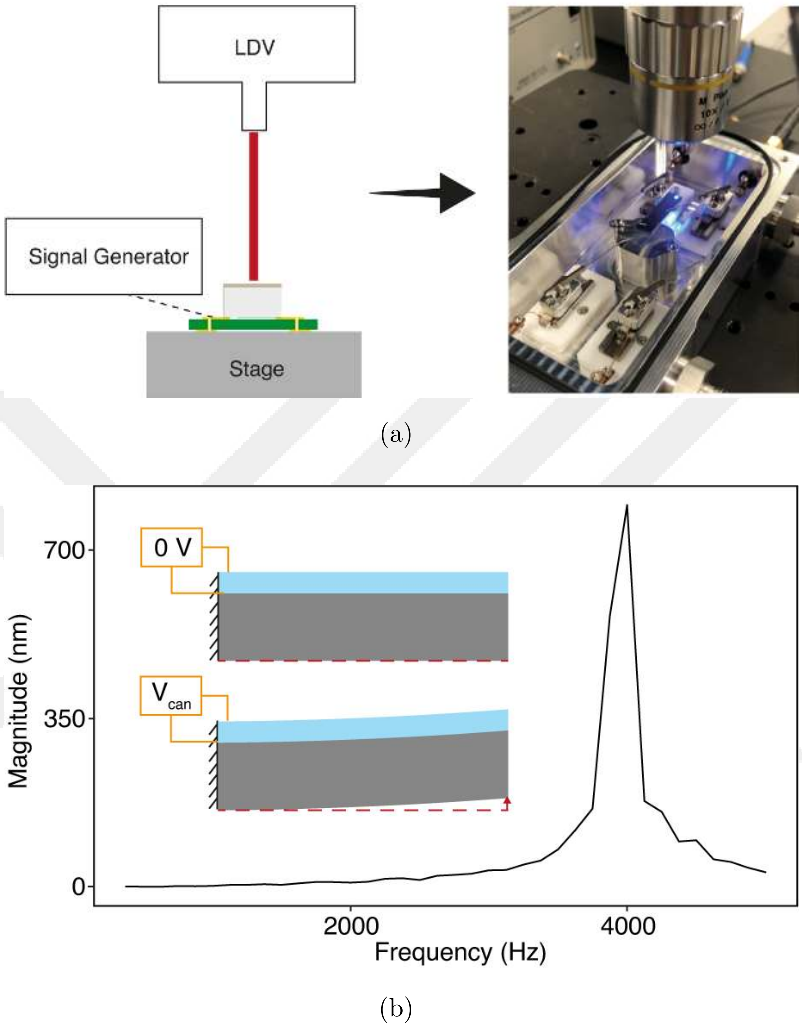

Figure 2.13: Cantilever measurement: (a) LDV measurement schematic and photo, (b) Measurement principle and tip vs. displacement results.

be fixed. The dynamic response of the cantilever can then be analyzed by LDV measurements taken at its tip [Kanno et al., 2003]. When the prepared sample was fixed at one-end and excited by a 2V periodic chirp signal with a frequency range of 0-5 kHz, the resonance of the cantilever was observed, confirming the actuation via the 31-mode of the piezoelectric film.

Following these studies on the piezoelectric film, PMUT fabrication methods were investigated. As summarized in Figure 2.14, a literature review focusing on

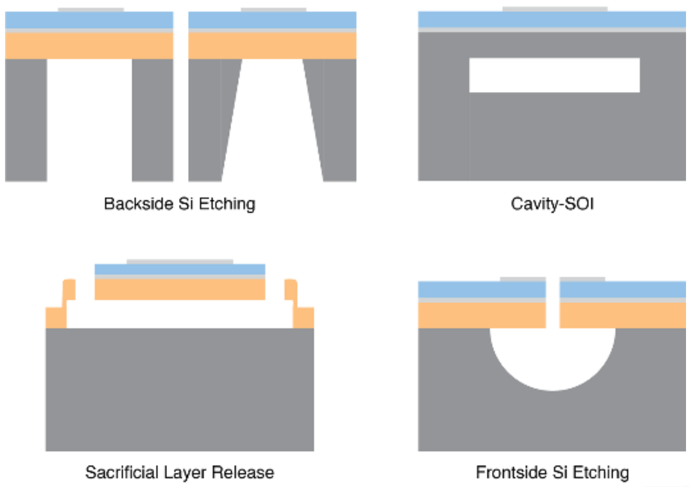

Figure 2.14: Common PMUT fabrication methods.

various microfabrication flows for PMUTs was completed. The methods were further evaluated with respect to the facilities at n^{2}STAR:

- **Backside Si Etching:** PMUTs are most commonly fabricated using backside silicon etching. This method is widely used, but initial trials highlighted key challenges such as grass formation, high costs for deep reactive ion etching (DRIE), design constraints and very low fill-factor for potassium hydroxide (KOH) etching, and the necessity of backside alignment for both.

- **Cavity-SOI:** Also referred to as built-in cavities, this method simplifies the fabrication process drastically. However, it comes with high costs and limited design flexibility, and was not considered within the scope of this dissertation.

- **Sacrificial Layer Release:** In addition to providing a simple process and eliminating backside alignment, this method can result in delicate surface-micromachined membranes and may have issues with sidewall coverage.

- **Frontside Si Etching:** PMUTs fabricated with frontside etching benefit from a simple process and elimination of backside alignment. However, this method presents challenges with deep etching and critical etch hole/area dimensions.

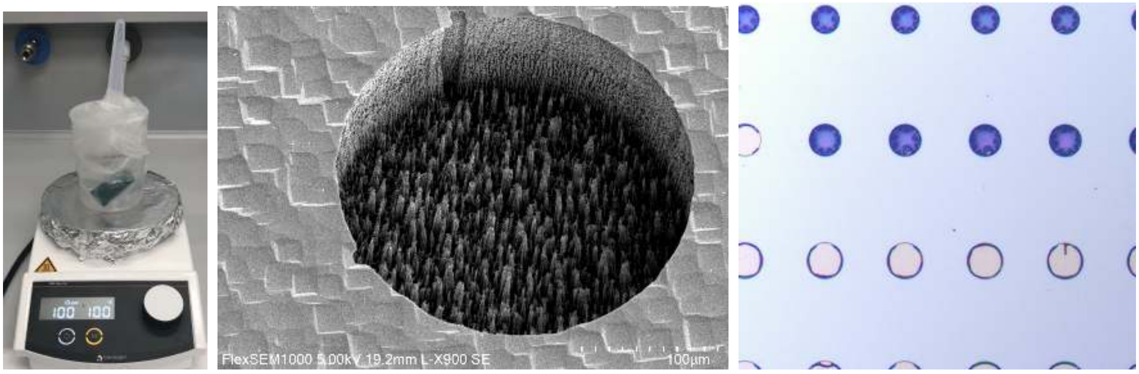

(a) (b) (c)

Figure 2.15: Exploratory membrane fabrication trials: (a) Photo of KOH etching setup, (b) SEM image of the grass formation due to micromasks caused by Cr hard mask used during DRIE, (c) Optical image of the succesfully released and collapsed SiO_2 membrane after germanium sacrifical layer etching by XeF_2.

Among the available fabrication methods, frontside Si etching with XeF_2 attracts interest due to its simplicity and capability of fabricating smaller membranes compared to backside Si etching based methods. Based on these findings, XeF_2 etching was chosen for the fabrication [Toymus et al., 2022]. Cleanroom facilities of N^2STAR was utilized to fabricate the PMUT prototypes. Prior to actual processes, chambers were cleaned and pre-conditioned by running the recipe without the die. For lithography steps, uMLA instrument from Heidelberg Instruments was utilized, along with AZ5214E photoresist and AZ MiF 726 developer.

1. The fabrication flow started with the deposition of a SiO_2 layer as the structural layer with ICP-PECVD at 90 °C. As the bottom electrode, a tri-layer Cr/Al/Cr was deposited by electron beam evaporation.

2. To create the etch hole for subsequent membrane release, the SiO_2 and bottom electrode layer were patterned with ICP-RIE. For SiO_2 etching, 50 W RF, 100 W ICP, 20 sccm CHF_3 and 10 sccm Ar were used at 25 °C and 0.5 Pa. For metal etching, 100 W RF, 600 W ICP, 20 sccm BCl_3, 5 sccm Cl_2 and 10 sccm Ar were used at 80 °C and 0.4 Pa. To have a transparent area for optical

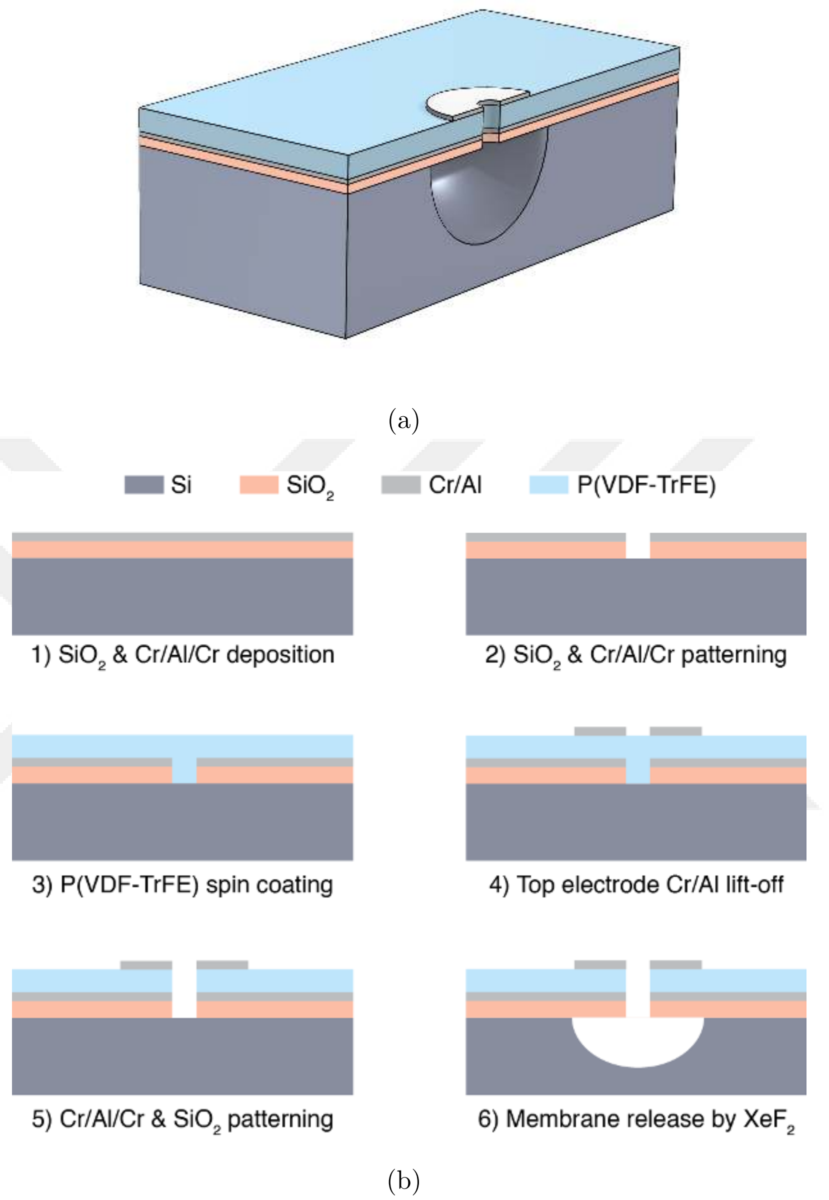

Figure 2.16: Proposed PMUT: (a) 3D illustration, (b) Fabrication flow.

characterization of XeF_2 etch size, an additional metal area was etched. Prior to metal etching, 100 sccm O_2 descum at 4 Pa was used.

3. Next, prepared P(VDF-TrFE) solution was spin coated at 2000 rpm for 60 seconds and baked at 140 °C for 10 minutes. This process was repeated twice to achieve ≈ 3 μm film thickness. Following this step, acetone was replaced

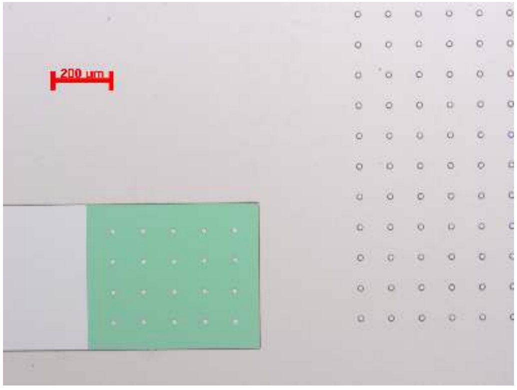

Figure 2.17: Optical image prior to spin coating.

with methanol to protect the deposited film.

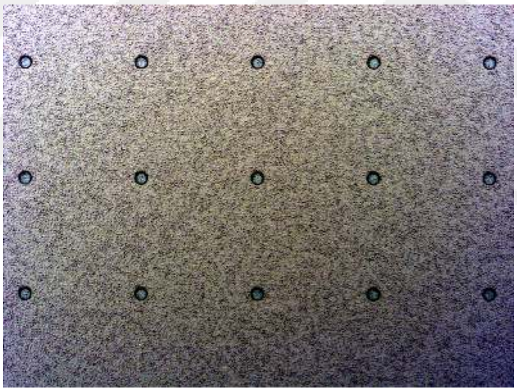

Figure 2.18: Optical image after spin coating.

4. For the top electrode, Cr/Al was again sputtered and patterned with lift-off or ICP-RIE.

5. For bottom pad opening and to fully open the neck of the structure and clear the etch holes, P(VDF-TrFE) was etched with ICP-RIE. For etching, 50 W RF, 250 W ICP, 50 sccm O_2 and 10 sccm Ar were used at 25 °C and 0.3 Pa.

6. As the last step, membranes were released by XeF_2 etching at 9 Torr and 50 sccm N_2 using the memsstar Orbis Alpha XeF_2 vapor phase etching tool.

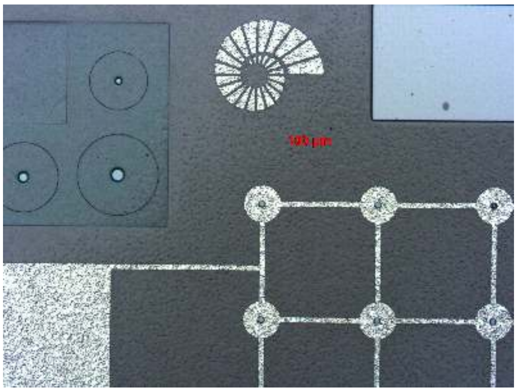

Figure 2.19: Optical image before membrane release.

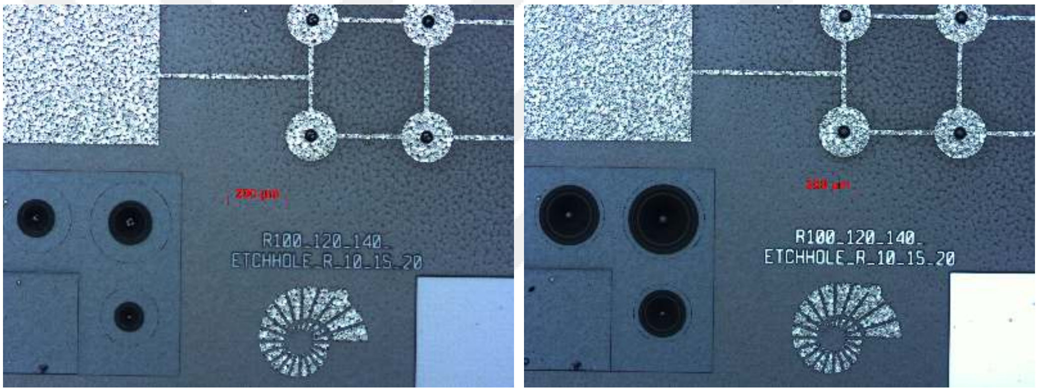

(a) (b)

Figure 2.20: Optical image after membrane release: (a) Midway through the etch, (b) After full etching.

Following fabrication, the membranes were further characterized by scanning electron (Hitachi FlexSEM) and LEXT laser scanning microscopy (Figure 2.22), which confirmed the released membrane structure.

Similar to the previously introduced cantilever samples, fabricated P(VDF-TrFE) based PMUTs were poled with DC-contact poling for 30 minutes. Poling was followed by the LDV characterization of the dynamic profiles of the PMUTs using Polytec MSA-600 LDV. With the help of a probe station and the intrinsic signal generator of the system, membranes were excited by a 2V periodic chirp signal with a frequency range upto 1.5 MHz as shown in Figure 2.23(a).

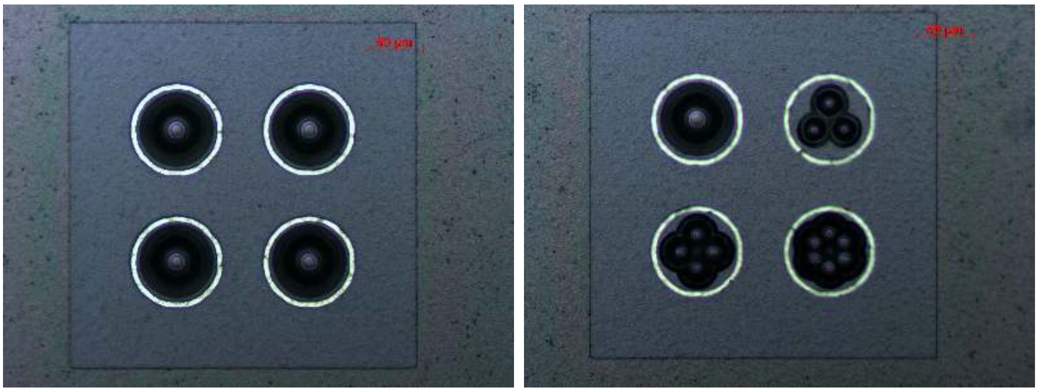

(a) (b)

Figure 2.21: Various etch hole strategies: (a) Single etch hole in the middle, (b) Distributed etch holes on the membrane.

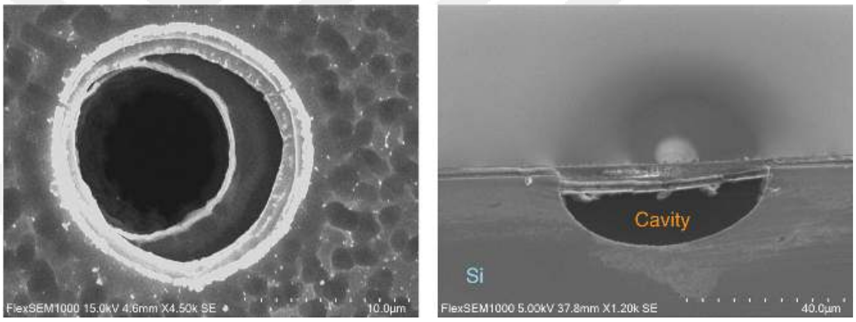

(a)

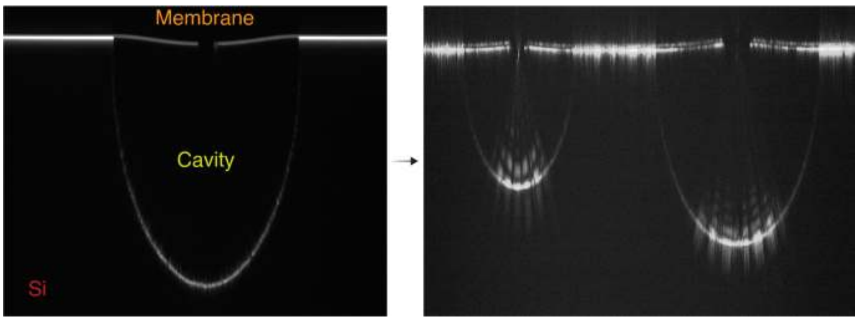

(b)

Figure 2.22: Microscopy images after membrane release: (a) SEM of top (left) and cross-sectional view (right), (b) LSM images of the transparent membranes. A dummy die with a SiO_2 membrane is also shown (left) for comparison with the PMUT die (right).

As illustrated in Figure 2.23(b), all three membranes displayed distinct resonance frequencies, which decrease with the increasing membrane radius as expected. On the other hand, increased member sizes also lead to increased displacements, albeit the lower frequencies. The inset shows a scan over a full grid of points on the membranes, highlighting the fundamental mode shape, whereas the plotted values were measured at positions with peak displacement values. Moreover, since the membranes required further insulation and sealing steps for underwater characterization, airborne pulse-echo measurements were conducted under LDV with values from the largest membrane plotted in Figure 2.23(c).

(a)

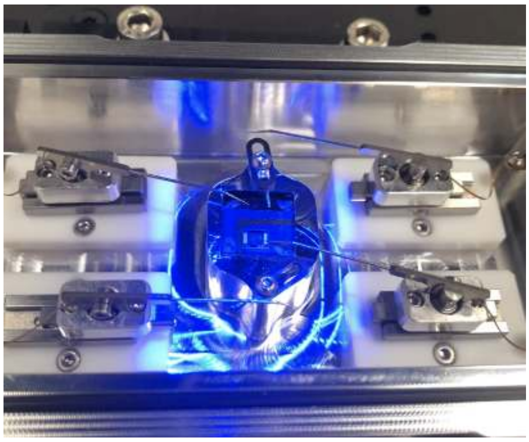

(b)

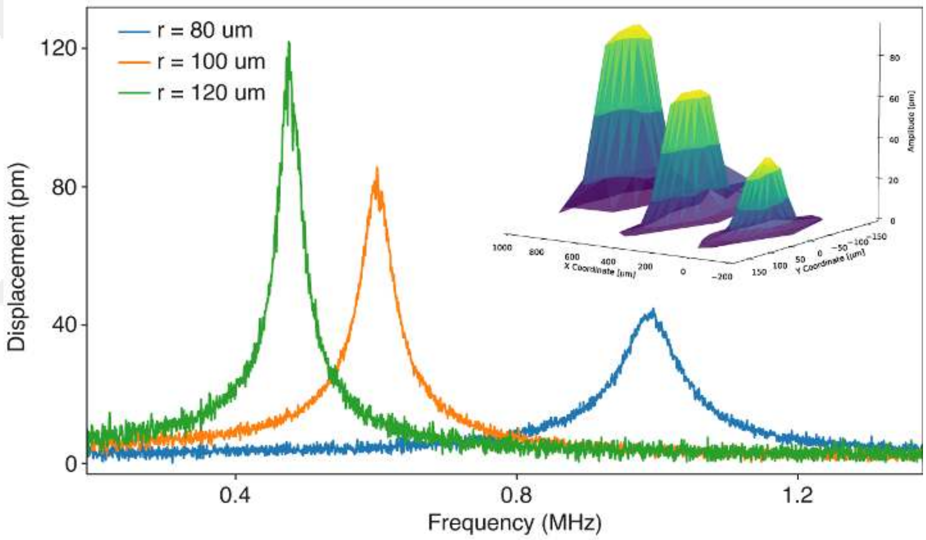

(c)

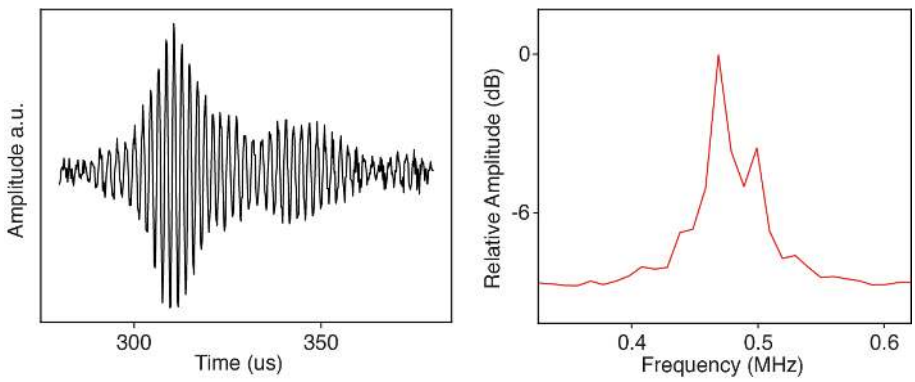

(d)

Figure 2.23: LDV measurements of the PMUTs: (a) Photo of probe station placed under LDV, (b) Photo of a die in probe station under LDV head, (c) Displacement vs. frequency plot, (d) Pulse-echo measurements in transient mode.

2.4 Discussion

While both transducer types utilize piezoelectricity for the generation and detection of ultrasound waves, their fabrication, performance characteristics, and maturity differ significantly. To better understand their design strategies, fabrication challenges, and characterization methods, this chapter aimed to develop single-element prototypes from both technologies. Due to their widespread use and commercial availability, bulk PZT plates were purchased and processed using conventional PCB techniques. Polymer-PMUTs, on the other hand, were developed in-house. Based on these prototypes, the following features were evaluated for integration into wearable devices:

- **Design:** The established analytical approaches and numerical tools for both technologies simplify the design process for both. The vibrational mode dependency of bulk piezoelectric transducers may limit their geometrical design flexibility. When integrating the bulk transducers with wearable electronics, packaging aspects and connections must be discussed during the design phase due to additional layers around the piezoelectric element. On the other hand, despite the small size of an individual PMUT element, array design can compensate for the size of an individual element and can be tailored for the application.

- **Fabrication:** Bulk PZT transducers are commercially available and can be simply diced or machined into desired geometries. Due to the acoustic impedance mismatch, the use of additional layers is generally required, which complicates fabrication. Moreover, the complexity of processing bulk transducers increases dramatically with an increasing number of elements. This is due to challenges in integrating a high number of electrical interconnects and variability in element performance (e.g., due to matching layer thickness homogeneity) – challenges where PMUTs shine. On the other hand, despite the established microfabrication processes and ease of array fabrication, deposition of high-quality piezoelectric layers is a major challenge and may not be worth the effort for smaller arrays. Therefore, for simpler designs with a small number of elements, bulk piezoelectric transducers should be the choice, given the maturity of the technology and the ease of rapid prototyping.

- **Acoustic performance:** Due to the sub-mm size of PMUT elements, the performance by itself is not comparable to that of a bulk transducer element by its own. Owing to the monolithic array design capabitlity, performance metrics such as the bandwidth, transmit and receive sensitivity and acoustic pressure output could be tailored and can reach to the levels of the mature bulk technology. Nevertheless, piezoelectric coefficients play a key role in the performance, as can be quantified by the electromechanical coupling coefficient, k_{eff}. While thin-film PMUTs based on more conventional piezomaterials show promising results in terms of key performance metrics, PMUTs based on piezopolymers such as those in this chapter, fall short with transmit sensitivities (less than 200 pm/V) an order of magnitude smaller than reported values as shown in Table 2.5.

Table 2.5: Transmit sensitivities of selected PMUT works.

Piezolayer	Trans. Sens. (nm/V)	Oper. Freq. (MHz)
PZT [Liu et al., 2022]	175	5.4
KNN [Huang et al., 2022]	245	0.1
ScAlN [Karuthedath et al., 2023]	150	7.1

Given these comparisons and considering the ease of signal processing and electronics development for a small number of elements in a wearable device, the focus of the following chapters will be on bulk piezoelectric transducers. However, PMUT technology remains a strong candidate, especially for the ultrasonic implant introduced in Chapter 5, due to its potential for extreme miniaturization. As PMUT transmit and receive sensitivities continue to improve, wearable applications introduced in the thesis may also benefit from this technology. Ultimately, bulk piezoelectric transducers were chosen for this study due to their technological maturity, broad applicability, and alignment with the proof-of-concept wearable device development and demonstration focus of this dissertation.

Chapter 3

WEARABLE ULTRASOUND FOR CONTINUOUS BLADDER VOLUME MONITORING

3.1 Introduction

Lower urinary tract dysfunction (LUTD) is an umbrella term that includes conditions and diseases related to the bladder and the urethra [D'Ancona et al., 2019]. LUTD affected 2.3 billion people worldwide in 2018, which is expected to increase in future due to the aging population [Irwin et al., 2011]. Common conditions that cause LUTD include benign prostate hyperplasia (BPH) [Awedew et al., 2022] and neurological disorders like multiple sclerosis [Phe et al., 2016] and spinal cord injury [Panicker et al., 2015]. For BPH-LUTD alone, the global economic burden was estimated to be more than 73 billion USD in 2019 [Launer et al., 2021].

Since LUTD revolve around the abnormalities during the filling and emptying of the bladder, bladder volume monitoring is an essential tool to evaluate bladder function [Nieuwhof-Leppink et al., 2019]. At present, the gold standard measurement method is the bladder catheterization [Gammie et al., 2020]. Despite its accuracy, it is not recommended for routine examinations due to the high adverse outcomes associated the invasive procedure [Smith et al., 2013]. Hence, clinicians rely on ultrasound imaging of the bladder to estimate the bladder volume, which is a quick and non-invasive method to obtain information such as post-void residual volume of the bladder. However, this method cannot provide continuous monitoring and necessitates trained personnel with expensive benchtop equipment. Moreover, both of these methods are applicable to patients while they are admitted to the hospital only. Outside the hospital, monitoring relies on the patients themselves to fill urinary diaries and questionnaires to provide information regarding the volume and frequency of micturition [Bright et al., 2014]. Although continuous monitoring via implantable sensors does exist at the research level [Hannah et al., 2019], only patients with complicated or severe symptoms would be suitable for such invasive devices [Thuroff et al., 2011]. Given the importance of bladder volume monitoring and the current status; precise and non-invasive technologies to monitor bladder volume outside the hospital settings are needed [Abelson et al., 2019].

To this end, decades of research have led to several commercial wearable devices in which signals from the anterior and posterior walls of the bladder are used to quantify the degree of bladder filling [van Leuteren, 2020]. Although such devices might be useful to alert the users when the bladder is full, they are not intended for accurate and continuous bladder volume measurement which is critical for diagnostic and treatment applications [van Leuteren et al., 2019]. In addition, these rigid and non-conformal devices suffer from reliability issues and require ultrasound gel for proper signal transmission which limits their usage during daily activities [Semproni et al., 2022]. Furthermore, although recent scientific studies reported improved accuracies for continuous monitoring by utilizing phased arrays or multiple elements, these studies either incorporate bulky electronics subsystems [Jo et al., 2021]. or lack such systems totally and require wired connections to benchtop laboratory equipment to conduct the measurements [Fournelle et al., 2021]. Other reported methods include electrical impedance analysis [Schlebusch et al., 2014] and near-infrared spectroscopy [Molavi et al., 2013]. However, these methods could only provide preventative insights, and such indirect measurements would only be suitable for coarse estimations of the bladder volume due to their low specificity, proneness to motion artifacts, and urine dependent properties [Koven and Herschorn, 2022]. Therefore, none of these devices are suitable for accurate and continuous bladder volume monitoring.

3.2 Measurement Strategy

Due to the invasiveness of the catheterization, bladder volume is determined by ultrasonographic measurements. Given the operator dependency of the ultrasound images and the various shapes of the bladder, numerous algorithms and formulae are developed to estimate the bladder volume from the ultrasound images of the bladder. Among these methods, spherical bladder assumption utilizes the maximum longitudinal (l), transverse (w) and anterior-posterior diameters (h) with a correction factor of 0.52 for bladder volume calculation [Bih et al., 1998]. The volume calculation formula is derived as follows:

$$\text{Volume of a sphere} = \frac{4}{3} \cdot \pi \cdot R^3 = \frac{4}{3} \cdot \pi \cdot \left(\frac{D}{2}\right)^3 \tag{3.1}$$

$$\text{Bladder Volume} = \frac{4}{3} \cdot \pi \cdot \left(\frac{l}{2}\right) \cdot \left(\frac{w}{2}\right) \cdot \left(\frac{h}{2}\right) = 0.52 \cdot l \cdot w \cdot h \tag{3.2}$$

Based on these findings, the decision was made to develop a wearable device for operator-free and continuous bladder volume monitoring. Due to the complexity of autonomous ultrasound imaging of the bladder continuously, alternative strategies utilizing amplitude mode (A-mode) ultrasound were investigated.

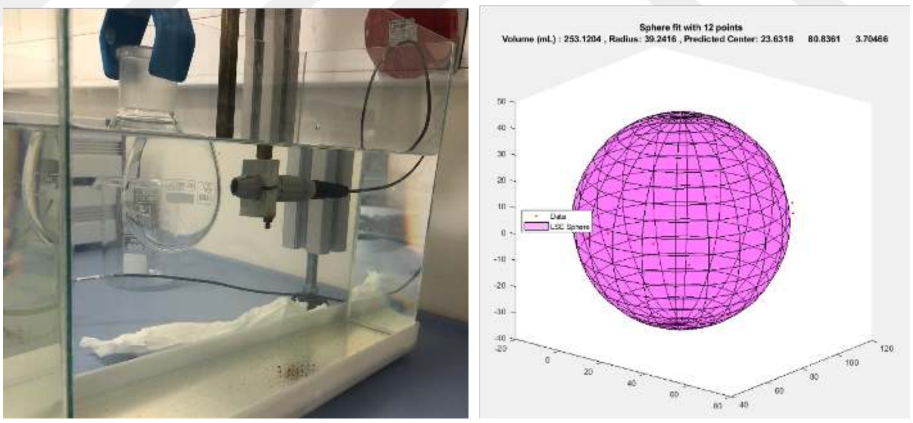

(a) (b)

Figure 3.1: Evaluation of the measurement strategy: (a) Measurement setup with a commercial immersion transducer and round-bottom flask, (b) Volume estimation of the flask based on measurement points.

In existing literature, many studies have employed various algorithms and formulae to approximate the shape of the bladder [Dicuio et al., 2005]. More specifically, some studies [Bih et al., 1998] analyzed the impact of bladder shape on the ultrasound image-based volume measurement accuracy [Kuzmić et al., 2003]. In the former [Bih et al., 1998], bladder shapes of 146 subjects were analyzed and classified into a geometrical shape. The reported values are 23 % for spherical, 25 % for cuboid, 21 % for ellipsoid, 25 % for triangular prism and 6 % for undefined shape. Although the use of specific calculations for specific bladder shapes improved the accuracy and decreased the error to less than 10 %, the use of a generalized formula, regardless of the bladder shape, still resulted in an acceptable error of less than 20 %. In the latter [Kuzmić et al., 2003], a similar study concluded that when bladder shape is considered in the selection of volume calculation method, mean error decreased from 16.9 % to 12.7 %. Based on these results, the simplest method of spherical volume fitting based on multiple anterior-posterior distance measurements was chosen for further investigation. To evaluate the spherical volume fitting strategy, a custom in-vitro measurement setup was built as shown in Figure 3.1(a).

After the acquisition of the signals from multiple points on the surface of the flasks, the information was used in a spherical fitting algorithm based on the following relation and a minimization optimization function:

$$(x - x_0)^2 + (y - y_0)^2 + (z - z_0)^2 = R^2 \tag{3.3}$$

where (x_0, y_0, z_0) is the center of the sphere and R is its radius. A representative result of the fitting procedure is shown in Figure 3.1(b). The algorithm calculated the volume of a 250 mL beaker as 253 mL. To determine the required number of measurement points for an accurate estimation, 16 measurements were taken on two flasks using a 4x4 scan array Figure 3.2. A varying number of measurement points were then used in the volume estimation algorithm. As shown in Figure 3.2(b), measurements with 4 piezoelectric elements provided accuracy comparable to those taken with 10 piezoelectric elements. Therefore, four elements were selected as a simple yet effective transducer module.

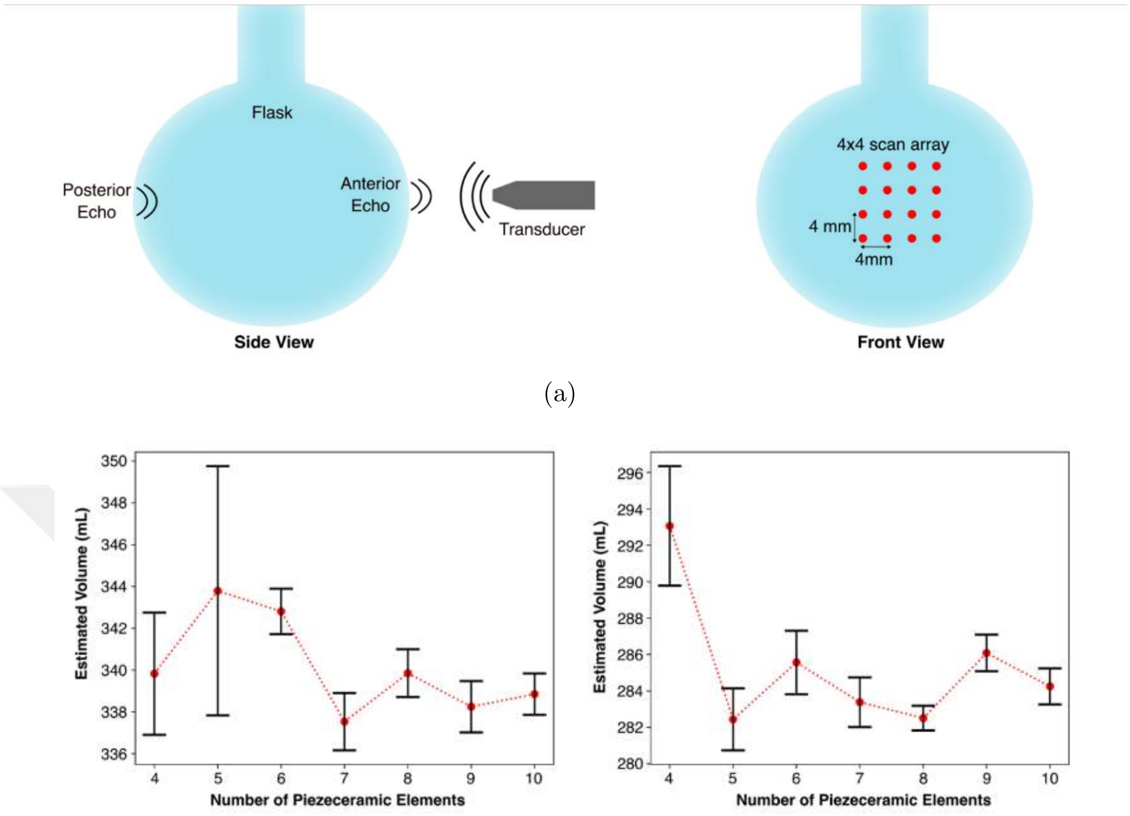

(a)

(b)

Figure 3.2: Effect of number of measurement points: (a) Measurement setup with a commercial immersion transducer and round-bottom flask, (b) Volume estimation of the flask based on number of measurement points used by the algorithm.

3.3 System Architecture

The concept and the operating principle of the proposed device are illustrated in Figure 3.3. Once placed in the lower abdomen, the device performs continuous and wireless monitoring of the bladder volume. This is achieved by continuously recording the distance between the anterior and the posterior wall of the bladder from multiple sites using multiple transducers. These measurements are then transferred to a nearby mobile device and utilized in a volume estimation algorithm. The measurement process involves sequentially exciting the transducers, which emit ultrasound waves toward the bladder.

In our specific application, these ultrasound waves are reflected from the anterior

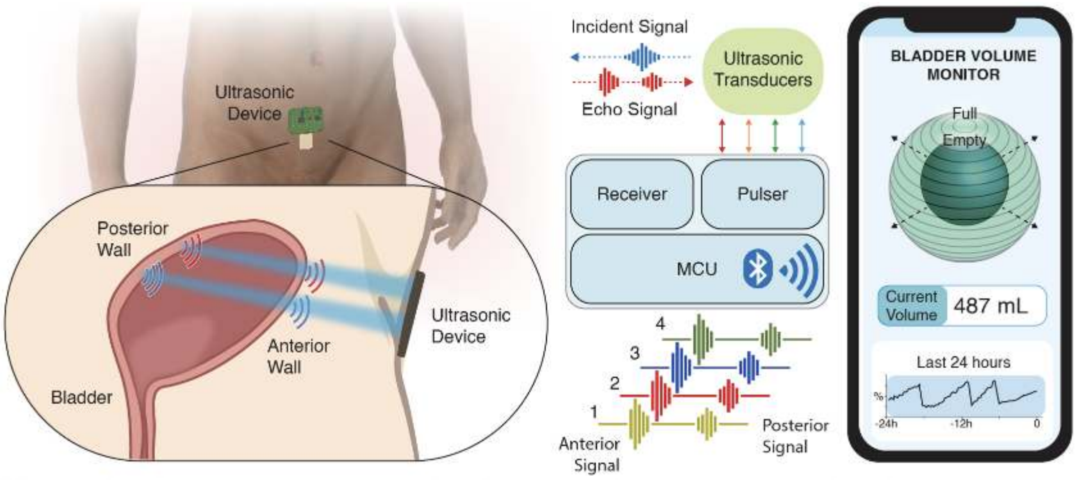

Figure 3.3: Operating principle of the system.

and the posterior walls of the bladder. Upon returning to the transducers, the waves are converted back into electrical signals, carrying location information of the reflection points from the bladder wall. This information is then transferred to a mobile device via Bluetooth technology. With sequential repetition of such a measurement from multiple transducers at multiple sites, an algorithm estimates a sphere with its surface points corresponding to the reflection points on the bladder surface.

The three main subsystems of the whole device are (1) a millimeter-scale conformal ultrasonic transducer module, (2) miniaturized electronics with integrated Bluetooth Low Energy capability, and (3) a custom mobile app that wirelessly communicates with the hardware and displays the bladder volume measurements (Figure 3.3). In addition to piezoceramics and their matching layers, the transducer module consists of a flexible substrate and soft silicone-based encapsulation layer to conform to the human skin (Figure 3.4).

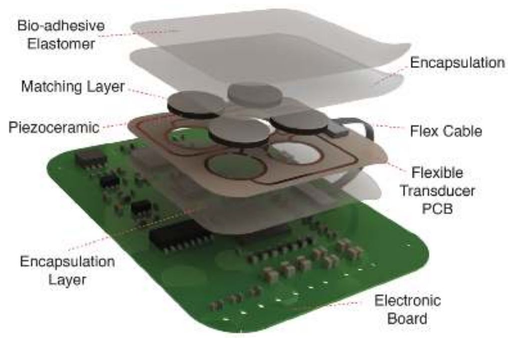

(a)

(b)

Figure 3.4: System architecture: (a) Exploded view of the whole device with transducers and control electronics, (b) Photograph of the transducers.

3.4 Transducer Design, Fabrication and Integration with Electronics

3.4.1 Piezoelectric Layer

In addition to the frequency bandwidth of the transducer, which is key influence in the axial resolution, the center (operating) frequency and the sound field of the transducer are critical factors. The center frequency plays a crucial role in the resolution and penetration depth due to frequency-dependent attenuation in tissue, which is approximately 0.5 dB/cm/MHz [Goss et al., 1979]. Due to this attenutation, higher frequencies are attenuated more rapidly, resulting in a trade-off with the axial resolution. Moreover, the sound pressure field, which is related to the aperture and the beam diameter influences the lateral resolution.

Based on these, a parametric study on operating frequency and aperture size was conducted in Field II [Jensen, 1997], [Jensen and Svendsen, 1992], and the results are shown in Figure 3.5. Based on these findings, a centre frequency of 2 MHz is decided based on the penetration depth, transducer thickness, and axial resolution requirements of the application. PZT discs with a diameter of 10 mm were chosen to isolate the thickness mode of the piezoceramic from other modes of vibrations, and to increase the pressure generated at deep sites so that posterior wall of the

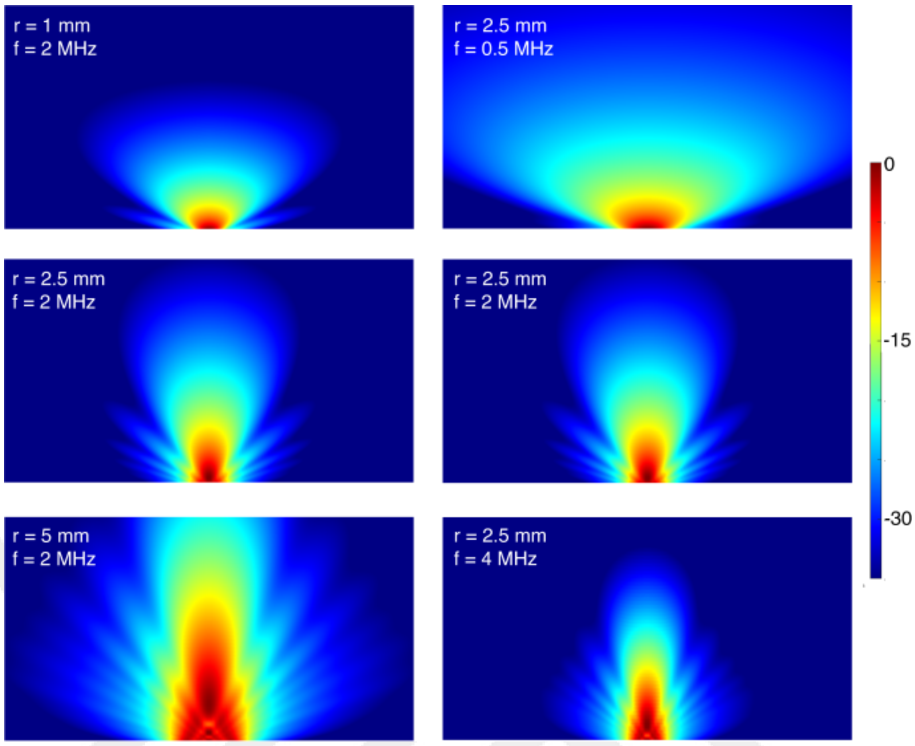

Figure 3.5: Acoustic pressure field (dB) simulations for a disc source in Field ii software.

bladder can be detected even at low excitation voltages.

To achieve a thickness-mode resonance frequency of approximately 2 MHz in the PZT disc, given a theoretical longitudinal speed of sound of 4600 m/s, the $\lambda/2$ criterion indicates a desired thickness of around 1.15 mm. Since this exact thickness wasn't readily available, the closest commercially available PZT discs with a thickness of 1 mm were used.

3.4.2 Backing and Matching Layers

Backing layers are typically used to improve the bandwidth of the transducer by introducing heavy damping and decreasing the ringdown of the piezoceramic which improves the axial resolution. Backing layer materials are typically made of filled epoxies with acoustic impedances close to that of the PZT. This causes the transmission of the most of the energy into the backing layer and get dissipated. This poses a significant problem for a wearable ultrasonic device that uses voltage levels lower than the levels used in the benchtop equipment. In addition, the use of a

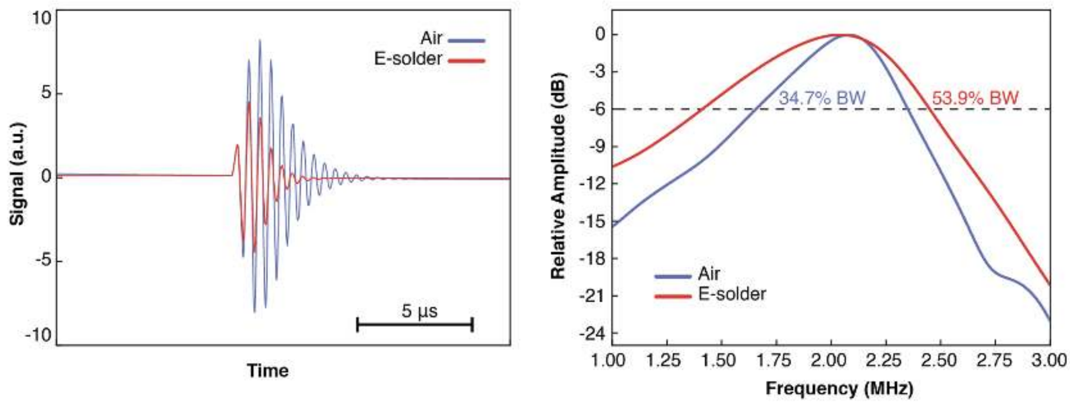

Figure 3.6: Simulated pulse-echo responses of a PZT disc with air-backing (left) vs E-solder (moderate backing, right).

backing layer introduces an unwanted increase in the thickness and overall footprint of the device, which harms the wearability and user-comfort of the device.

Due to these concerns, air-backing was utilized in the design. The fact that it creates a greater acoustic impedance mismatch at the back of the transducer causes less power to travel into the backing and more into the tissue. This can be further seen in the pulse-echo responses of a transducer ECM by comparing the air-backing with a commonly used backing layer material E-solder 3022 (a moderate impedance value of 5.92 MRayl) [Zhou et al., 2014]. Figure 3.6 highlights the higher SNR of the air-backed configuration.

Furthermore, air-backing decreases the overall footprint and weight of the transducer by avoiding the thick backing layer which is an essential requirement in a wearable device. The longer ringdown times and hence worse axial resolution caused by the air-backing does not affect the application since the ultrasonic signals reflected from the anterior and posterior walls of the bladder are very apart from each other. For instance, the time-of-flight for anterior wall signal is between 25 and 50 microseconds whereas the range for posterior wall signal is between 90 and 250 microseconds, depending on the state of the bladder. Therefore, the ringdown effect caused by the anterior wall signal dissipate long before the posterior wall signal is recorded.

To further improve the performance of the transducers device, matching layers were prepared by mixing epoxy (EPOTEK 301-2FL) with alumina nanoparticles. The weight percentage of the mixture is decided by the optimum matching layer acoustic impedance calculation as introduced earlier [Desilets et al., 1978]. Using the acoustic impedances of tissue and PZT piezoceramic, the target acoustic impedance for the matching layer can be calculated as below:

$$Z_1 = 31.5^{\frac{1}{3}} \cdot 1.63^{\frac{2}{3}} = 4.32\,\mathrm{MRayl} \tag{3.4}$$

To use as the matching layer material, several Al_2O_3-Epoxy mixtures with varying weight percentages are assessed. The specific acoustic impedance of the matching layer material is calculated by multiplying its density and the speed of sound c_s, which was calculated according to (4.5), where d is the sample thickness and c_w is the speed of sound in water.

$$c_s = \frac{c_w d}{d + c_w(t_{with\_sample} - t_{without\_sample})} \tag{3.5}$$

The speed of sound measurements were done underwater in an ultrasonic measurement system setup using commercial immersion transducers and hydrophones, both from Precision Acoustics, as shown in Figure 3.7.

The density of the Al_2O_3-epoxy mixture is calculated by dividing the sample's mass to its volume. As a result of several iterations, 40-wt% mixture of Al_2O_3-epoxy was observed to give the targeted acoustic impedance.

3.4.3 Fabrication

For fabrication of the ultrasonic transducers, bulk PZT disks were purchased from American Piezo (APC-850). To enable access to top and bottom electrodes from the same plane, disks were modified to a custom wrap-around electrode configuration. A commercial picosecond-pulsed laser ablation system; 500 kHz pulse repetition frequency and 1.5 W power, LPKF) was utilized to isolate a small portion of the silver electrode on one face of the PZT disc. Then, the isolated portion of the silver

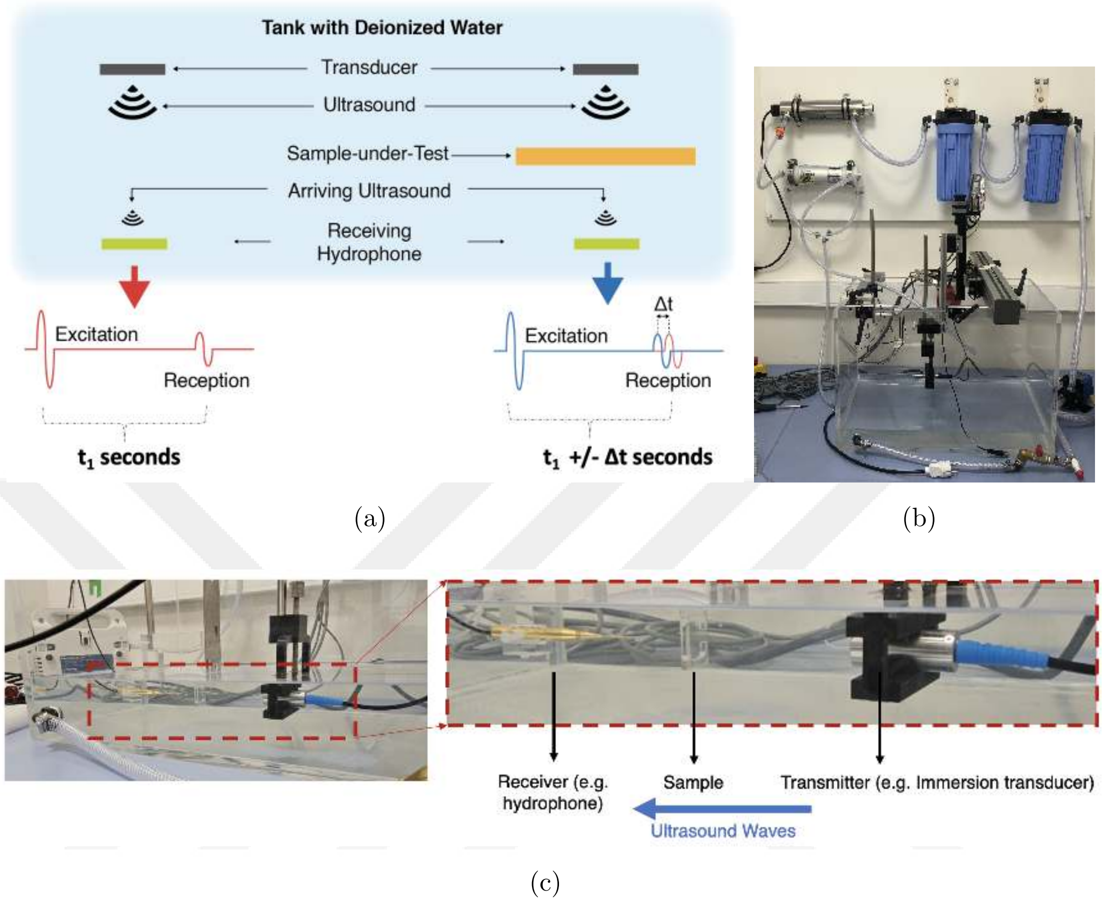

Figure 3.7: Speed of sound measurements: (a) Schematic of through-transmission, (b) Photo of the tank setup, (c) Photo of the measurement.

electrode on that face was electrically connected to the electrode on the opposite face of the disc using a low-temperature silver paste (PE827, DuPont).

Following the preparation of individual PZT transducers in wrap-around electrode configuration, a 25 µm-thick flexible laminate with 9 µm copper layer (AC0925, DuPont) was patterned with LPKF U4 to create the circuit pattern of the transducers and cut the laminate for air-backing. Two-component epoxy resin (EPOTEK 301-2FL, 1:0.35) was mixed at 3500 rpm for 20 min using a speed mixer (Hauschild mixer, DAC 150). Alumina nanoparticles (290 nm, Nanografi) were added to the mixture for desired acoustic impedance and mixed at 3500 rpm for another 10 min using the same speed mixer. The epoxy-nanoparticle mixture was poured inside a disc-shaped PDMS (Dow Corning, 10:1) mold. Cured matching layer was manually

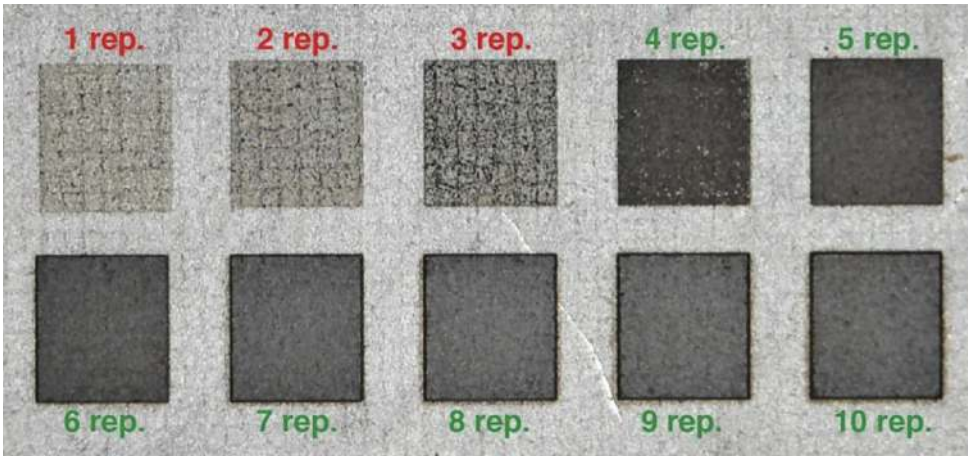

(a)

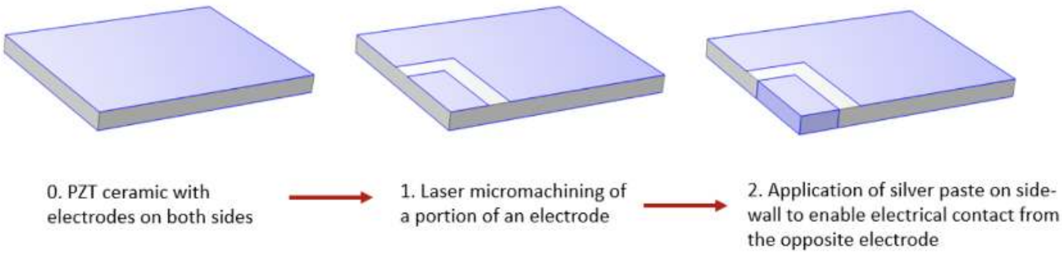

(b)

Figure 3.8: Preparation of PZTs with wrap-around electrode configuration: (a) Microscope images of the laser etched electrode surface, (b) Fabrication flow.

bonded to PZT disks using a fast-curing two-component epoxy (Loctite EA3 422, 1:1). PZT disks with matching layers were manually placed and reflowed with low-temperature solder paste (TS391LT, Chip Quik). To preserve the air-backed design of the transducers, laminate under the disc-shaped PZTs was cut. In analogous fashion, a doublesided tape (Tesa 64621) was machined. PZT-soldered laminate adhered to the bottom encapsulation layer (40 µm-thick PET sheet) using double-sided tape. For the front side encapsulation, a mold was 3D printed (BMF microArch S230) and parylene-c-coated (Plasma Parylene Systems). The laminate with transducers was placed inside the mold. Silicone encapsulant (PDMS, 10:1) was poured and cured at 60 °C for 9 h. The fabrication flow is shown in Figure 3.9.

Figure 3.10 illustrates the comparison of various acoustic coupling agents used in

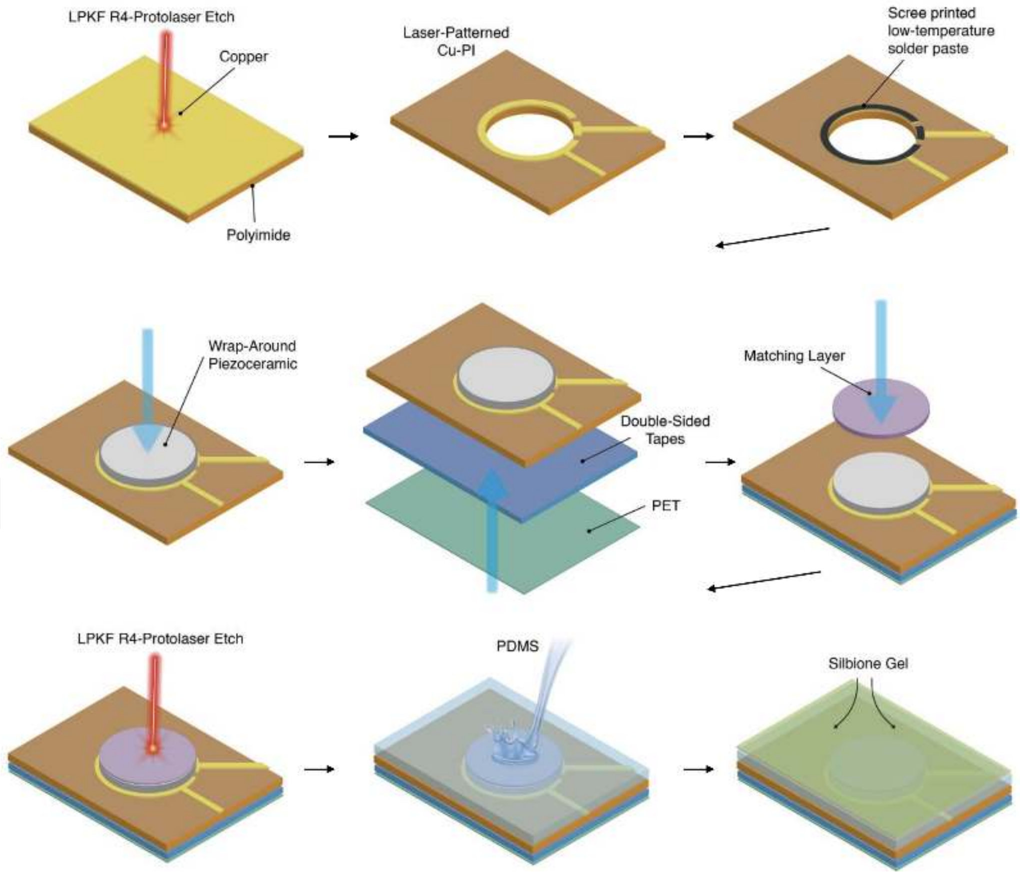

Figure 3.9: Fabrication flow of the transducer module.

the pulse-echo test setup. In the experimental setup, a commercial immersion transducer (V323-SU, Olympus) was employed to record ultrasound waves reflected from the air boundary of a thick PMMA block. Different acoustic coupling agents were applied between the transducer and the PMMA block to ensure efficient transmission of the ultrasound waves. The setup allows for the evaluation of how well each coupling agent facilitates the transmission of sound waves and the corresponding signal quality, measured as the amplitude of the reflected echo.

Furthermore, the peak ultrasound echo amplitudes obtained for each of the coupling agents tested, with a total of 10 repetitions per condition (n=10) are also displayed in Figure 3.10. The data reveals variability in the effectiveness of the coupling agents, providing insight into their relative efficiency in transmitting sound waves through the medium. These results are crucial for selecting optimal coupling

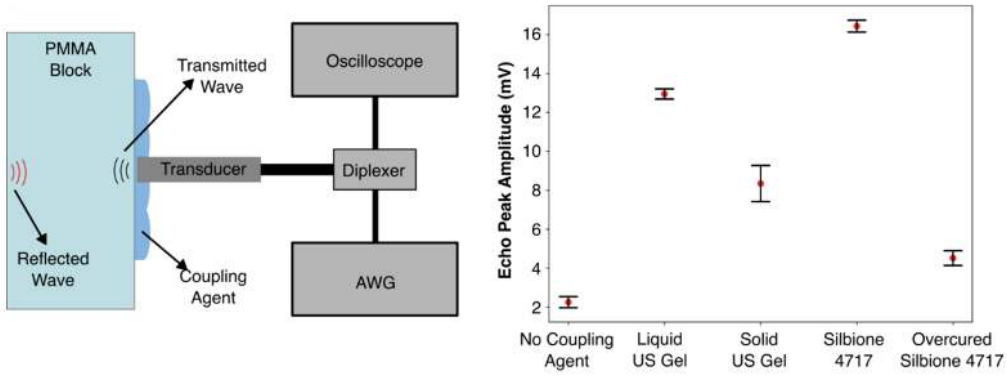

Figure 3.10: Acoustic couplent agent comparison with schematic of the pulse-echo test setup (left), Peak ultrasound echo amplitudes for various acoustic coupling agents ($n = 10$) (right).

agents for specific applications in acoustic testing, where maximizing echo amplitude is essential for accurate measurements and diagnostics. As a result, to enable gel-free measurements, Silbione 4717 gel (1:1) was screen-printed on the front side of the transducers. Silbione gel offers robust adhesion and very little acoustic attenuation, making it a good choice for wearable ultrasonic applications.

3.4.4 Characterization

All electrical and acoustics characterizations were conducted in deionized water. An impedance analyzer (MFIA, Zurich Instruments) was employed to obtain frequency-dependent electrical parameters (electrical impedance, phase, conductance) of the transducer. For the pulse-echo response, an arbitrary waveform generator (33521B Waveform Generator, Keysight) was used to excite the transducer-under-test. The echo signal from a stainless steel reflector was received by an oscilloscope (Picoscope 6000 series) through the use of a diplexer (RDX-6, RITEC Inc.).

Underwater characterizations were conducted inside a UMS Research system covered with acoustic absorbers (AptFlex F28, Precision Acoustics). The pressure field, sound pressure output, and bandwidth were evaluated with a 0.5 mm needle hydrophone (Precision Acoustics) connected to an oscilloscope (DSOX3024G, Keysight Technologies).

Figure 3.11 illustrates the cross-sectional view of the fabricated transducer and the electrical impedance and phase measurements underwater. The impedance curve demonstrates the resonance behaviour around the frequency of interest as discussed earlier.

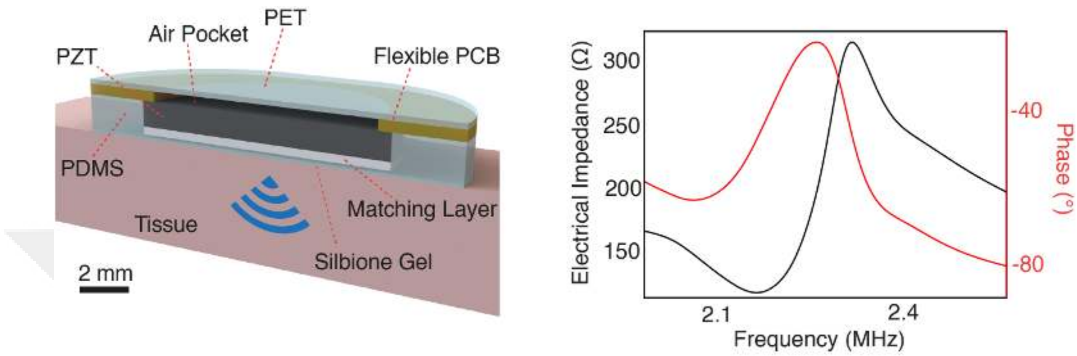

Figure 3.11: Cross-sectional view and electrical characteristics of a transducer.

Pulse-echo response of the transducer and its derived frequency spectrum are shown in Figure 3.12. Due to the air-backing, the transducer demonstrated a relatively high quality factor with a -6 dB bandwidth of 37.9%.

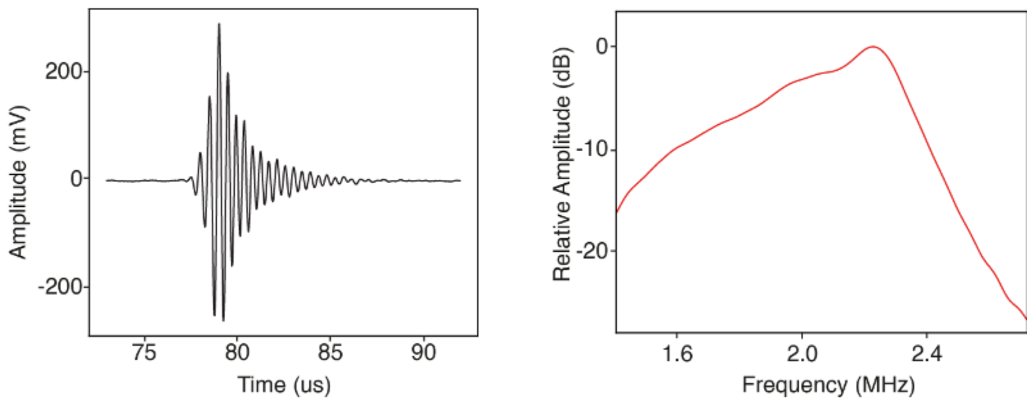

Figure 3.12: Raw echo signal waveform and corresponding FFT of a single transducer.

Underwater pressure field scans of the trandsucer is shown in Figure 3.13. Figure 3.13(a) shows the 1D scans, highlighting the near-field distance of the transducer and intensity area at its focal point. 2D pressure field of the transducer in the longitudinal direction is shown in Figure 3.13(b), showing the directivity of the transducer as a result of the chosen aspect ratio of the PZT disc. This is further supported by the transverse pressure field scan of the transducer, where the -6 dB contour lines are smaller than the radius of the PZT disc.

To assess the mechanical durability and robustness of the transducers, a comprehensive test was performed using a custom-built bending stage. This experiment was designed to simulate real-world conditions where the transducer might be subject to repeated bending and flexing during its application. The transducers underwent 500 bending cycles, each involving the application of mechanical stress to the device in a controlled manner. This was done to evaluate if repeated bending would lead to any degradation in the performance or functionality of the transducers.

Before and after the bending procedure, the transducers were subjected to a pulse-echo experiment to measure their performance. In this experiment, an ultrasonic pulse was transmitted through the transducer, and the echoes received from the reflective surface were analyzed. The primary focus was to observe any variations in the signal strength, resolution, or any other measurable parameters that could indicate wear or damage to the transducer's internal structure. The results showed that, despite the 500 bending cycles, the transducer performance remained consistent and unchanged. No significant degradation was observed in terms of signal quality or sensitivity (Figure 3.14).

To evaluate the skin wearability of the device, a flexible piezoresistive force sensor (FlexiForce A201, Tekscan) was placed between the skin and the device. The piezoresistive nature of the sensor allows it to detect changes in resistance in response to applied pressure, providing an accurate measurement of contact force. The impedance of the sensor was recorded using an impedance analyzer, which allowed for precise monitoring of force variations during the experiment (Figure 3.15).

The results showed that the average contact force exerted by the device on the skin was approximately 0.17 N. This moderate contact force suggests that the device applies a well-distributed pressure that is unlikely to cause discomfort or skin irritation during prolonged use.

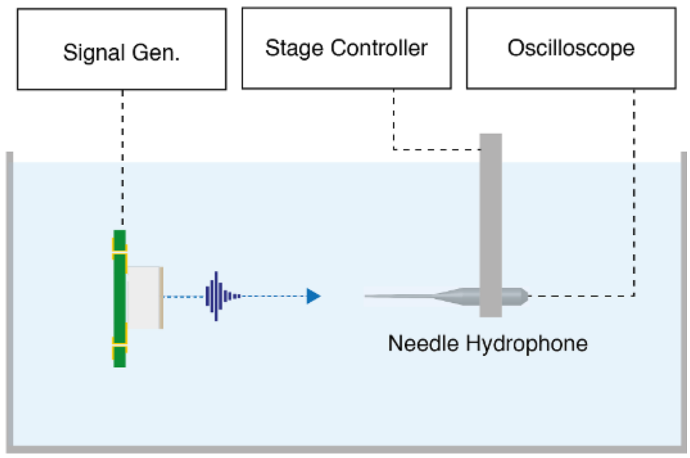

(a)

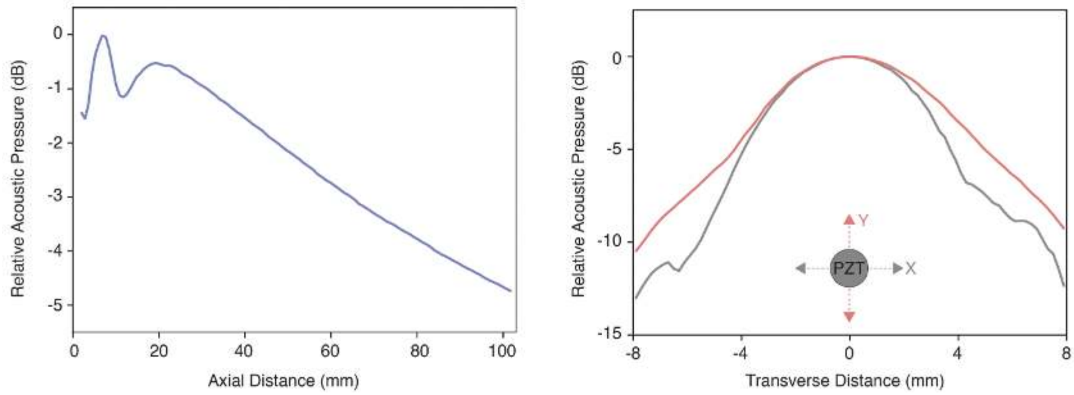

(b)

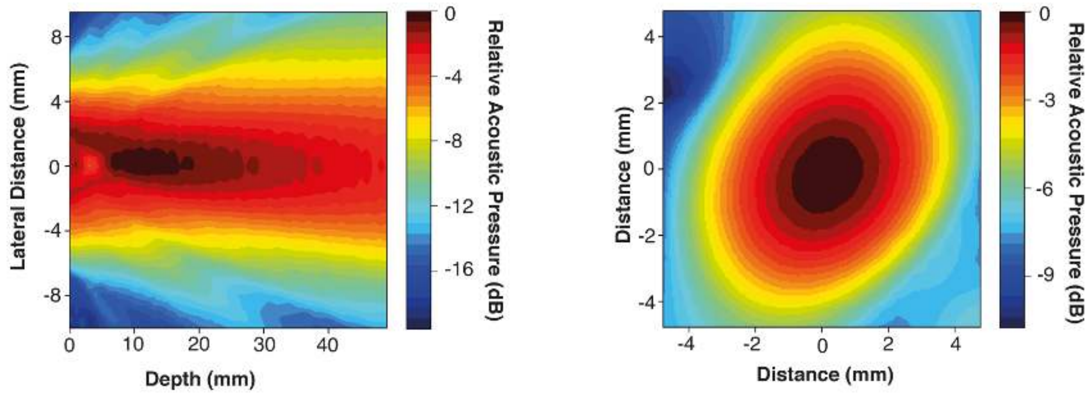

(c)

Figure 3.13: Underwater pressure field maps of a transducer: (a) Schematic of measurement setup, (b) 1D scan of pressure field in longitudinal (left) and transverse (left) orientations, (c) 2D scan fields.

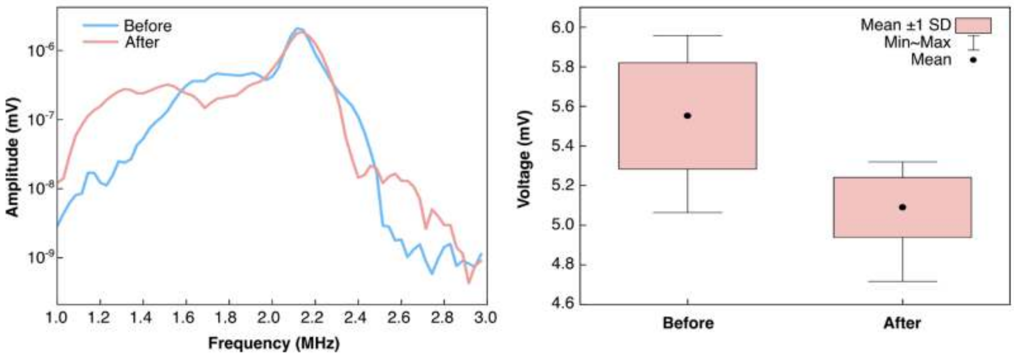

Figure 3.14: Repetitive bending test results with FFT spectra of echo signals (left) and (right) peak-to-peak echo amplitude comparison before and after repetitive bending $n = 25$.

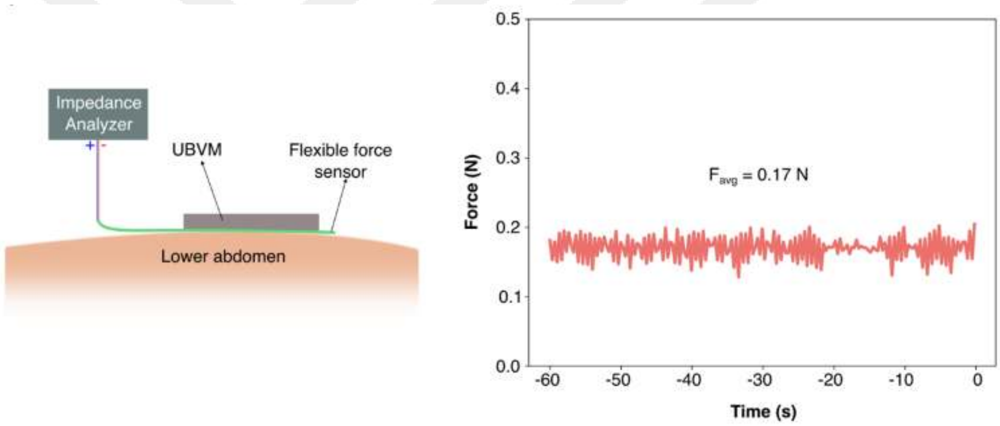

Figure 3.15: Applied force on the skin measurements with setup (left) and force readings from the sensor (right).

3.5 *In-vitro and In-vivo Demonstration*

After characterizing the ultrasonic transducer module, the full device was tested in vitro to simulate bladder volume measurements in a controlled environment. The device was placed in a water tank where various-shaped flasks—spherical round-bottom, oval-shaped round-bottom, and Erlenmeyer—represented different bladder volumes and shapes. To better replicate in vivo conditions, the flasks were submerged into the UMS Research system, with transducers connected via a flexible cable to the PCB outside the water tank as shown in Figure 3.16.

(a)

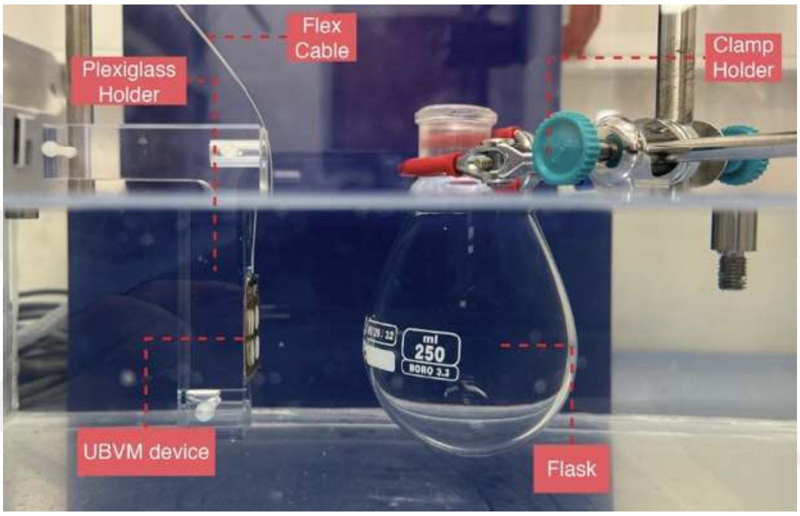

(b)

Figure 3.16: In-vitro setup for bladder volume measurements: (a) Spherical-shaped round-bottom flasks used in the experiment, (b) A photo of the setup with the transducers and the flask placed inside the water tank.

The measurements were conducted in deionized water, chosen for its acoustic impedance properties similar to human tissue. The transducer signals were captured, and timestamps were transferred to a mobile app, which processed the signals, converted them into coordinate points, and fitted them to a spherical shape for volume calculation. The device estimated the flask volumes with a mean relative error of 14.85 %, demonstrating its ability to detect volume changes under varying conditions as shown in Figure 3.17.

Furthermore, in-vivo measurements were conducted to demonstrate the continuous bladder volume monitoring capability of device. Figure 3.18(a) shows a photo-

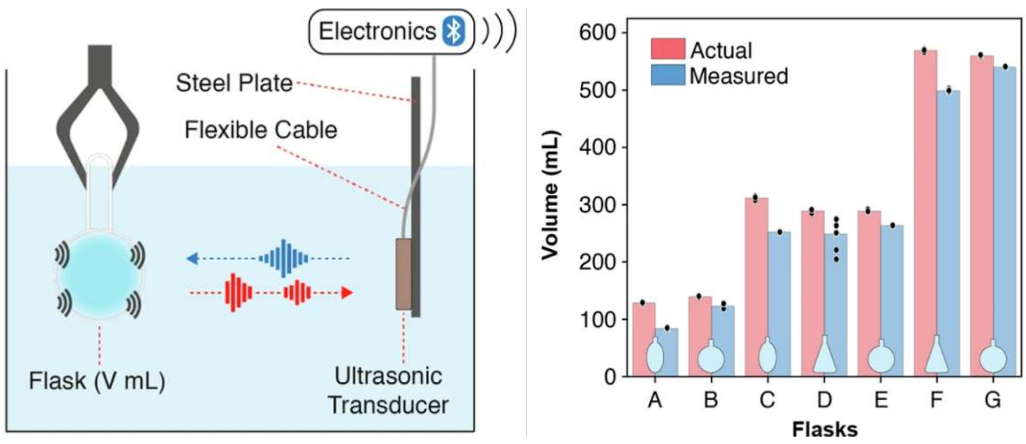

(a) (b)

Figure 3.17: In-vitro demonstration of the system: (a) Schematic drawing of the in-vitro setup of the whole system. The test set-up mimics the bladder with flasks in deionized water, where the transducers were connected to the electronics with a 1-m-long flex cable. (b) Comparison of the actual volume and the measured volume of flasks with various volumes and shapes ($n = 10$).

graph of the transducers on the lower abdomen of a volunteer. In an ideal measurement, the four transducers should receive eight echo signals in total, four from the anterior and another four from the posterior wall of the bladder. The mobile app analyzes the received signals and alerts the user if the number of echoes received is below five, which is the minimum required for accurate spherical fitting, prompting the user to reposition the transducers. In order to observe a full micturition cycle, measurements were initiated with an empty bladder and the transducers are placed with the guidance from the mobile app.

To validate the accuracy of the volume estimates, ultrasound images of the bladder were used to calculate the bladder volumes of five healthy (3 females and 2 males) volunteers. The ultrasound images were captured by an experienced urologist using a commercial ultrasound imaging system as shown in Figure 3.18(b). After the ultrasonographic bladder volume assessments of the participants, the values were compared to the estimates of the developed device. Volume estimations were recorded every 30 minutes by opening the custom app for automatic calculation of the bladder volume. Figure 3.19(a) shows a full micturition cycle of the volunteer

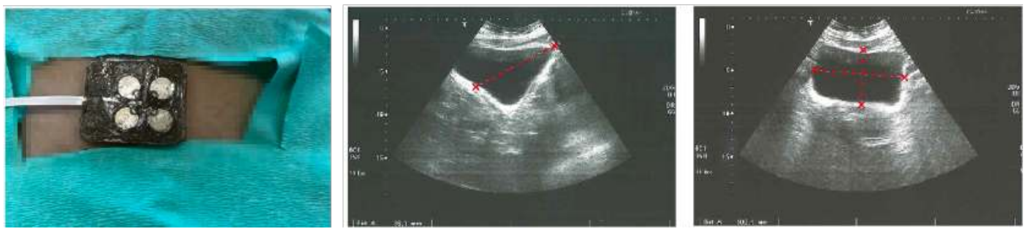

(a) (b)

Figure 3.18: In-vivo experiments: (a) Developed transducers placed on the lower abdomen of a volunteer. (b) Comparative ultrasound images of the bladder taken by a commercial scanner.

captured by the device and the A-P distance data from one of the transducers. The increasing bladder volume trend can easily be recognized. The transducers measure the A-P wall distances of the bladder, and multiple distance measurements are used to estimate the volume.

As shown in Figure 3.19(b), the device accurately estimated the bladder volumes of the participants with volumes ranging from as low as 84 mL to as high as 800 mL, demonstrating its performance in various bladder shapes and sizes. Raw echo signals and the associated comparator output are shown in Figure 3.20. Thanks to the air-backed design with the matching layer, echoes from the anterior and posterior walls of the bladder are clearly captured, even with an excitation voltage as low as 30 V.

3.6 Discussion

In this chapter, a wearable ultrasonic device for bladder volume monitoring was described. At the core of the device is flexible transducer module with a simple fabrication method and an air-backed design that enables low driving voltages.

The overall device has two key advantages compared to existing technologies, which either suffer from accuracy issues or require wired connections to benchtop equipment for measurements [Zhang et al., 2024], [van Leuteren et al., 2019]. Firstly, the device eliminates the wires current ultrasonic patches require and is fully inte-

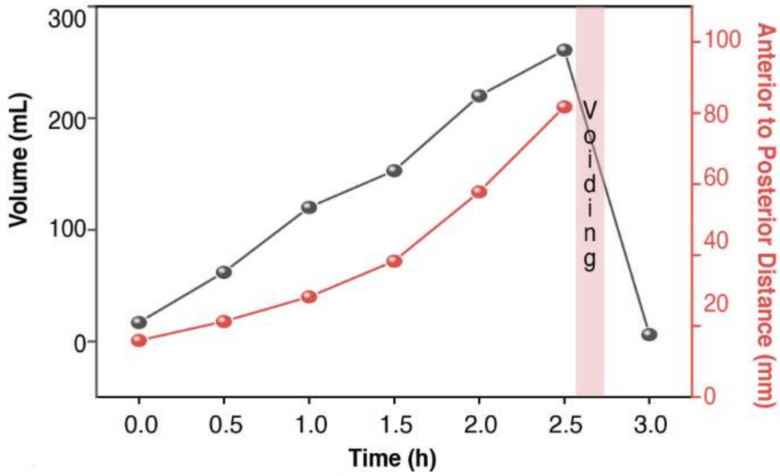

(a)

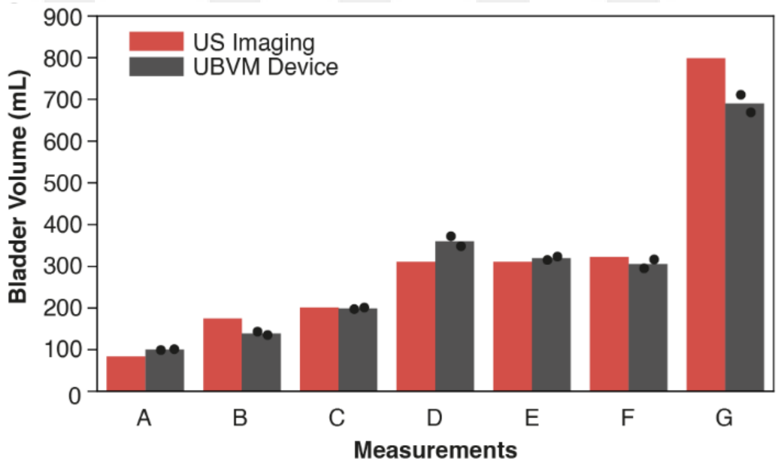

(b)

Figure 3.19: In-vivo results: (a) Monitoring during a micturition cycle (red) and the A–P distance measurements (black). (b) Comparison of the device measurements with the volumes from conventional ultrasound imaging of the volunteers ($n = 2$).

grated and wearable. This is of utmost importance to enable unobtrusive measurements and continuous monitoring. Secondly, such full wearability does not carry the burden of unreliable and inaccurate results. By utilizing multiple transducers, the device offers non-invasive measurements with high accuracy. This superior performance was demonstrated by thorough wearability studies and in-vitro characterizations with a mean relative error of 14.85 % among various shaped flasks to mimic various shaped bladders in clinical scenarios. In addition, in-vivo measure-

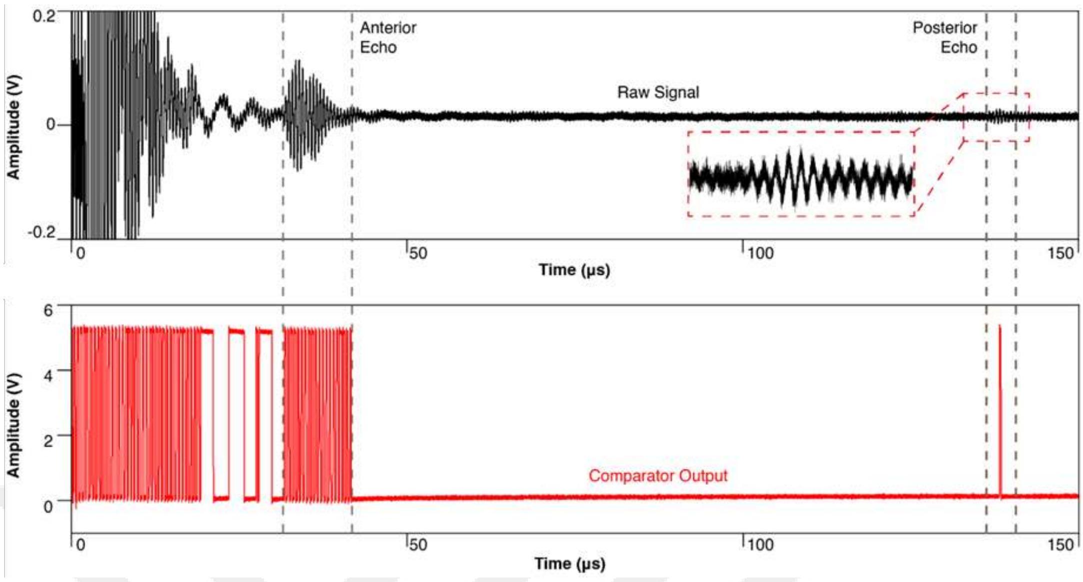

Figure 3.20: Raw and processed signals.

ments revealed a mean relative error of 11.17 % of the patch with various bladder shapes and volumes ranging from 100 to 800 mL.

Future work could focus on increasing the number of transducers while reducing the overall footprint. Although the accuracies of the in-vivo measurements are well within the acceptable range, further improvements in the accuracy are possible with the increased number of coordinates to conduct the volume fitting. In addition, by acquiring at least nine coordinate points, the device would be able to conduct ellipsoid fitting, which might result in improved estimates and an overall increase in the accuracy. This increase in the number of transducers could be achieved by increasing the frequency of the transducers, shrinking their size in all three dimensions, and expanding the number of channels of the multiplexers used in the current version of the electronics. Furthermore, a more comprehensive in-vivo validation could be completed to evaluate the performance of the device for patients with lower urinary tract dysfunctions and overweight and obese patients. Once these points are addressed, it is expected that the device will become an invaluable tool in addressing various use cases, such as lower urinary tract symptoms and post-operative urinary retention. In addition, while the focus has been on bladder volume monitoring, extended versions of the transducer module with minor hardware and firmware modifications can open up new dimensions in wearable ultrasound imaging.

Chapter 4

ELECTRONICS-FREE ULTRASONIC TAGS FOR WEARABLE ULTRASOUND

4.1 Introduction

Ultrasound examination has become an essential tool in clinical medicine for a broad spectrum of applications [Fitzgerald et al., 2022]. Compared to other medical imaging technologies such as CT scan, magnetic resonance imaging, and X-rays, ultrasound stands out for its portability, relatively low cost and greater accessability [Morris and Perkins, 2012]. Modern electronics and advances in fabrication and signal processing have reduced the cost and size of ultrasonic devices, leading to the development of hand-held ultrasonic probes and the rise of point-of-care ultrasound [Bledsoe and Zimmerman, 2021]. Despite these advancements, ultrasound probes are still too bulky for continuous, skin-mounted monitoring as wearable devices outside of clinical settings, similar to glucose monitors. Moreover, the expertise required for manual operation of these devices by highly trained clinicians further complicates their use in continuous monitoring. Therefore, developing wireless and wearable ultrasonic tools to enable operator-free ultrasound is a major step forward in diagnostic healthcare [Lin et al., 2022].

To address these issues, wearable ultrasound is a rapidly emerging field that attracted researchers [Huang et al., 2024]. Despite being in the early stages of development, wearable ultrasonic transducers have been reported to be used for various applications such as blood pressure monitoring [Wang et al., 2018], deep-tissue hemodynamics monitoring [Wang et al., 2021a], cardiac imaging [Hu et al., 2023a], elastography [Hu et al., 2023b], long-term organ imaging [Wang et al., 2022], continuous doppler [Kenny et al., 2021] and bladder volume monitoring [Zhang et al., 2024]. Majority of these reports focused on development of small footprint and conformal ultrasonic transducers, utilizing benchtop equipment for transducer excitation and data processing as sketched in Figure 4.1. In the previous chapter, I introduced a fully integrated battery-powered wearable ultrasound patch with wireless electronics for bladder volume monitoring [Toymus et al., 2024]. These reports highlight two main challenges for fully wearable ultrasonic patches. Firstly, the

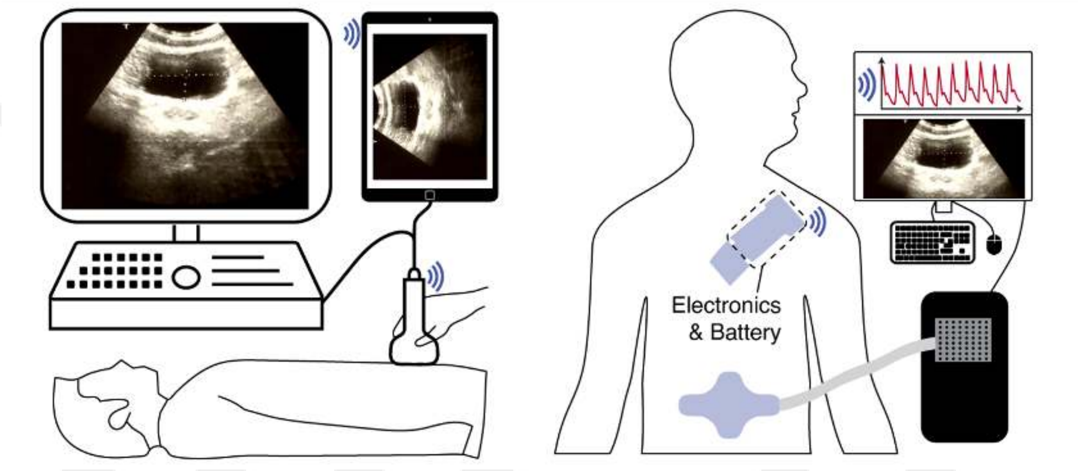

Figure 4.1: Ultrasonic device landscape: conventional (left) vs. emerging (right).

electronic circuitry required for wireless operation can occupy several tens of square centimeters [Toymus et al., 2024],[Lin et al., 2023]. Secondly, the batteries often need frequent replacement and rely on external recharging [Vostrikov et al., 2025]. The battery issue is also a significant concern for wearable ultrasonic devices since the technology requires high sample rates and processing speeds. For instance, a battery with power consumption of hundreds of milliwatts would require several square centimeters to sustain a few hours of operation. Looking ahead, resolving the size and battery barriers would enable the development of miniaturized wearable ultrasound for monitoring various health metrics including the blood pressure or the bladder volume, and could also pave the way for new applications such as an ultrasonic lens for ophthalmologic ultrasonography. Therefore, similar to bioelectronic implants [Nair et al., 2023], fully wearable ultrasonic devices with potential for further miniaturization rely on battery-less technologies, which have yet to be demonstrated.

4.2 System Design and Equivalent Circuit Modeling

From a conceptual point of view, the US tags are distributed sensory nodes at various measurement sites that enable ultrasonic measurements on-demand at multiple sites (Figure 4.2). By separating the transducers from the control electronics and the battery, the ultra-compact US tags can perform wireless ultrasonic measurements at various body locations.

Through strategic choices of the placement sites and wireless inductive coupling to the external T/R coil, the US tags enable numerous applications, including the monitoring of axial eye length, bladder volume and blood pressure. Unlike conventional ultrasonic devices, which would require dedicated electronic circuitry for each application, such a wireless measurement scheme enables the use of a single external device to conduct measurements with all the on-body US tags.

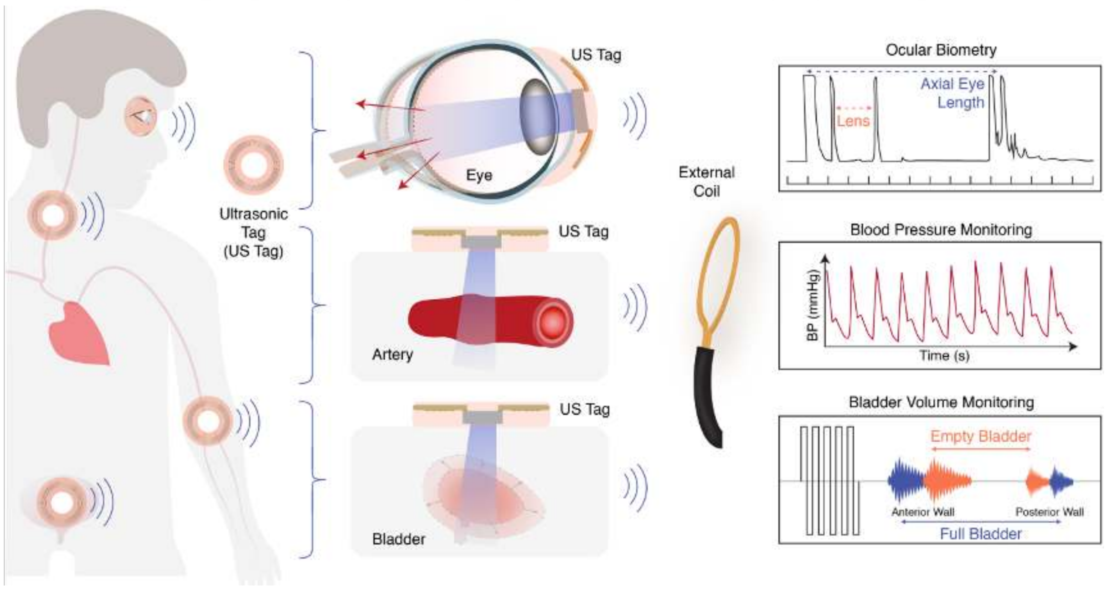

Figure 4.2: Sketch of US tags placed on various sites for multi-site physiological monitoring. The miniaturized tags can be tailored for ocular and epidermal applications. When wirelessly coupled to an external reader, the tags enable battery-less and electronics-free monitoring of e.g. axial eye length, blood pressure and bladder volume.

At their core, the US tags contain an ultrasonic transducer -with or without matching and backing layers- connected to a coil on a single layer printed circuit board (PCB) (Figure 4.3). The overall footprint of a tag can be further miniaturized by using multi-layer PCBs to implement the transducer coil, and by using piezocomposites to eliminate the need for matching and backing layers in demanding applications. The structure is encapsulated with a biocompatible soft silicone elastomer to conform the human skin. To meet the specific requirements of the individual applications, the US tags can cover the full diagnostic ultrasound frequency range and operate at 2, 5 and 10 MHz. In addition, to demonstrate different use-cases, transducers with and without matching and backing layers were developed. With these operating frequencies, thicknesses of the US tags range from 0.3 mm to 1 mm whereas the diameter of the tags are between 1 and 2 cm (Figure 4.4).

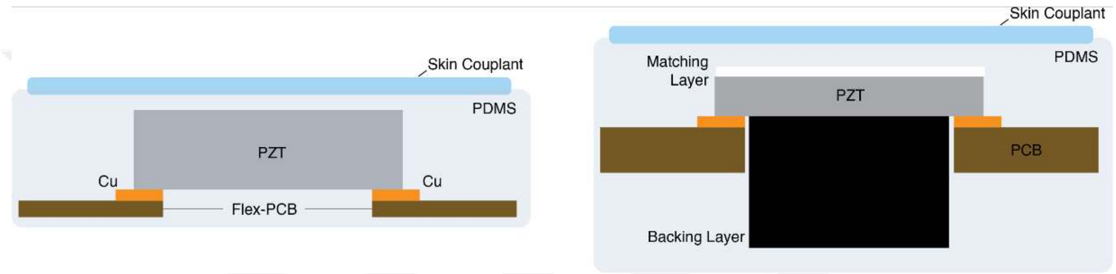

Figure 4.3: US Tag designs with and without matching and backing layers.

(a)

(b)

Figure 4.4: Concept of the US tags: (a) Exploded view of the epidermal US patch and US contact lens. (b) Photograph of a US tag next to a 1 Turkish Lira coin for scale.

The wireless excitation of the US tags and subsequent wireless reception of the echo signals requires an external T/R coil in close proximity of the US tags (Fig. 4.5(a)). By matching the operating frequency of the T/R coil with the US tag, maximum power transfer is achieved, which enables wireless ultrasonic measurements. Received echo signals are then processed specifically for each application.

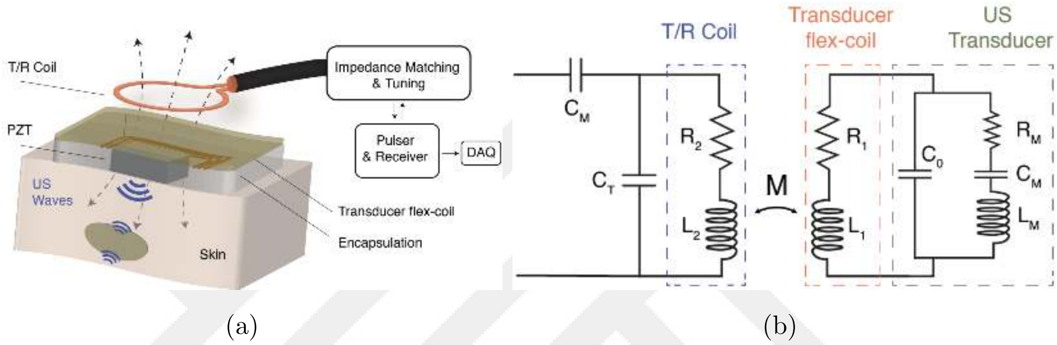

Figure 4.5: Wireless operation of the US tags: (a) Operating principle and cross-sectional view of the US tags. (b) Simplified equivalent circuit model of the US tags and external T/R coil.

Fig. 4.5(b) displays the simplified equivalent circuit model (ECM) of the wireless US tag system. We constitute the US tag ECM by using the Butterworth-Van Dyke (BVD) model to describe the electrical parameters of the PZT based ultrasonic transducer and combine it with the transducer coil inductance L_1 and resistance R_1. When the external T/R coil with inductance L_2 and resistance R_2, which is tuned and matched for the desired frequency using capacitors C_T and C_M, is in close proximity of the US tag, wireless inductive coupling of the ultrasonic signals is achieved.

4.3 Fabrication and Characterization

The fabrication of the US tags employed a combination of various materials and micro manufacturing techniques. The main active elements of the devices were wrap-around electroded PZT discs and bulk PZT plates with silver electrodes, sourced from American Piezo (APC - 850) and CTS Ferroperm (Pz27), respectively. These bulk PZT plates were diced into the required dimensions using a DAD3350 dicing saw (DISCO Corporation). To facilitate access to both electrodes of the diced PZTs from the same plane, one face of the PZT discs underwent laser ablation (LPKF Laser & Electronics, R4) using a 500 kHz pulse repetition frequency, similar to the procedure described in the previous chapter. The laser process, set at 1.5 W power and 1500 mm/s cutting speed, removed a portion of the electrode, exposing the underlying ceramic for electrical connection. This exposed portion was then connected to the electrode on the opposite side using low-temperature silver paste (DuPont PE827). The result was a functional PZT element capable of supporting ultrasound transmission and reception.

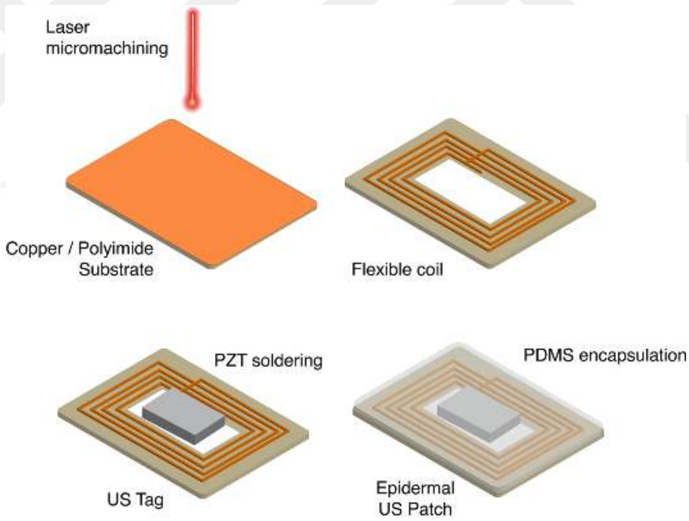

Figure 4.6: Fabrication flow of US tag in epidermal US patch format.

The flexible laminate used for the ultrasound tags was 0.2 mm thick with an 18 µm copper layer, purchased from LPKF (119818), and patterned using the LPKF U4 laser system to create the flexible coils. These coils were designed such that their operational frequency matched the resonance frequency of the PZT transducers. The PZT elements were manually aligned with the pads of the flexible coils and then soldered using low-temperature solder (TS391LT, Chip Quik). Once the assembly was complete, the PZT coils were encapsulated in a degassed silicone elastomer

(PDMS) mixture (Sylgard 184, mixed in a 10:1 ratio) for protection and durability (Figure 4.6).

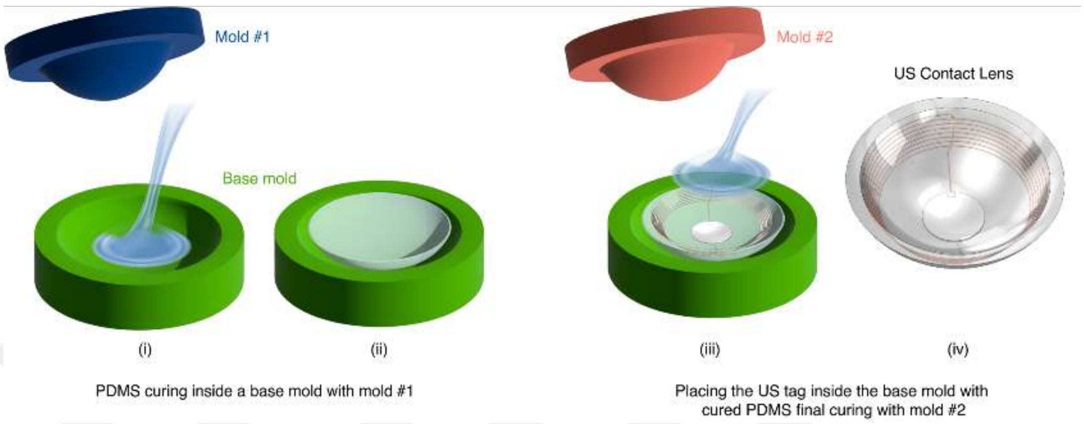

Figure 4.7: Fabrication flow of US tag in US contact lens.

Custom molds were used to fabricate the encapsulation for two formats: an epidermal patch and a contact lens, which were then cured in an oven at 40°C overnight (Figure 4.7). Additionally, a standard 1.5 mm thick FR4 board (LPKF) with an 18 µm copper layer was patterned with the LPKF U4 laser to create the T/R coils of the tags, which are critical components in enabling the bidirectional operation of the US tag.

For the blood pressure monitoring application, the device's performance was enhanced through the use of matching and backing layers (Figure 4.8).

Lead wires were first soldered to the wrap-around PZTs using low-temperature solder wire (SMDIN52SN48, Chip Quik). The soldered PZTs were then placed inside a silicone mold with a cavity, ensuring that the ceramic transducer fit perfectly. A few layers of PTFE double-sided tape were laser-patterned and applied to the PZT as a spacer for the matching layer screen-printing process. Epoxy resins loaded with various inorganic particles were then prepared for the matching and backing layers. The matching layer was made using 60% alumina nanoparticles (290 nm, Nanografi) mixed into epoxy resin (EPOTEK 301-2 FL), which was then screen-printed onto the ceramic surface and cured at 80°C for 8 hours. The backing layer, designed to improve acoustic attenuation, was composed of tungsten microparticles

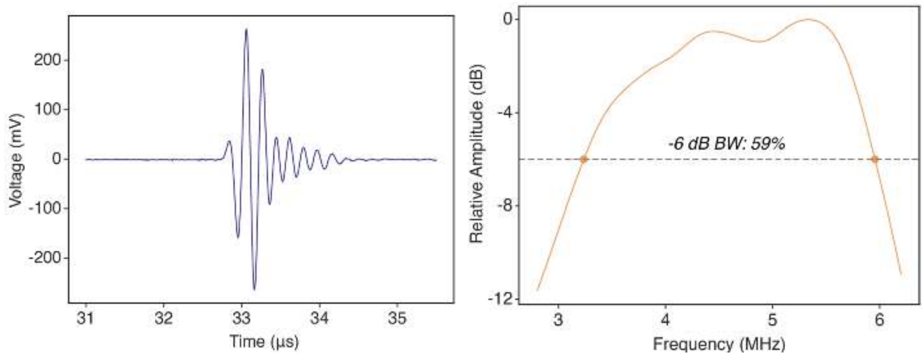

(a) (b)

Figure 4.8: Transducer used in the blood pressure monitoring US Tag: (a) Raw echo signal. (b) Frequency spectrum.

(1-10 µm, Nanografi) mixed into a highly attenuative epoxy. The backing layer was also screen-printed and cured similarly. The matching layer was then lapped to the desired thickness using conductance measurements to ensure optimal acoustic impedance matching.

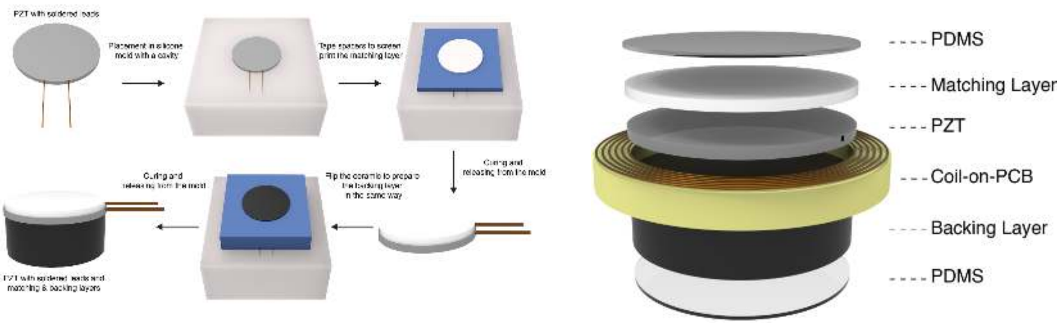

(a) (b)

Figure 4.9: US tag in epidermal format with matching and backing layers: (a) Fabrication flow, (b) US tag with coil.

After ECM based calculations of the required dimensions, the coil of the US tag is fabricated by nano-second laser micromachining to achieve 100 µm line gaps and line widths in transducer coil fabrication (Figure 4.10).

Although the parameters vary between the US tags for each application, we de-

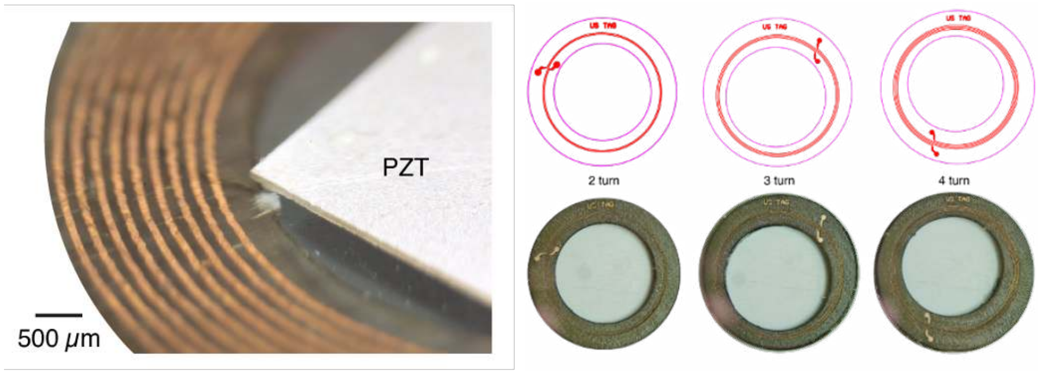

(a) (b)

Figure 4.10: US tag coil: (a) Optical image of an US tag, showing the PZT transducer and flexible coil, (b) Representative transducer coil designs with varying turn numbers.

velop a generalized design and characterization workflow for the realization of the US tags in three different frequencies. Initially, we extract the electrical parameters (R_m, C_m, L_m and C_0) of the ultrasonic transducer by BVM model fitting (Figure 4.11(a)). An impedance analyzer (MFIA, Zurich Instruments) was used to determine the electrical characteristics of the transducer. Measured impedance values were fitted to BVD model for subsequent coil design. These fitted parameters are then used within the previously described ECM and the required L_1 and R_1 values of the transducer coil to match the operating frequency of the US tag with that of the PZT were calculated. For the bladder volume monitoring patch, operating frequency was around 2 MHz.

Table 4.1: Representative coil design parameters.

Application	Coil	Turns	Trace Width	Gap Width	Inner Diam.	Outer Diam.
Bladder	Tag	13	200 um	100 um	13.2 mm	20.8 mm
Bladder	T/R	45	100 um	100 um	7.2 mm	25 mm
BP	Tag	15	100 um	100 um	5.3 mm	11.3 mm
BP	T/R	45	100 um	100 um	3.7 mm	21.5 mm

The procedure was validated by the return loss measurements of the US tag with a single turn PCB coil, highlighting the expected frequency of the US tag based on the model and the measured S_{11} value (Figure 4.11(b)). S11 parameters of the US tag was wirelessly measured using a single turn planar spiral coil connected to a vector network analyzer (VNA) (SVA1000X, Siglent). Furthermore, for T/R coil, impedance matching and tuning capacitors were used to maximize the power transfer and tune the frequency to the frequency of the tags. During matching and tuning, the coil was connected to the VNA to determine the S11 parameter.

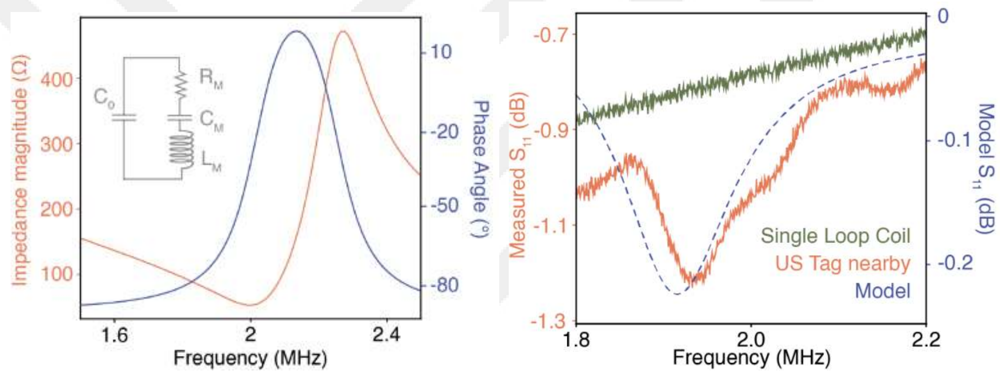

(a) (b)

Figure 4.11: Electrical Characterizations: (a) Fitted Butterworth-van-Dyke equivalent model of US tag to its measured impedance. (b) Calculated vs measured S11 of a single turn coil with and without US tag nearby.

Figure 4.12(a) shows the Laser Doppler Vibrometer (LDV) measurements of the US tag, wirelessly driven by an external T/R coil. Coils were coaxially aligned and affixed with an inter-coil distance of 5 mm. T/R coil was excited with a 2 V periodic chirp signal generated by the LDV, and surface displacements were recorded for the frequency range of interest. Measured surface displacements with respect to excitation frequencies highlight that the maximum displacement of the transducer occurs around 2 MHz.

Similarly, the US tags were characterized underwater. To evaluate the wireless pulse-echo response, US tags were placed in an acrylic water tank and affixed on the wall with a double-sided tape. The tank was filled with deionized water, and T/R coil was aligned from outside the water tank. An arbitrary waveform generator (AWG 33521B, Keysight) was used to excite T/R coil. The echo signal from a stainless-steel reflector was received by an oscilloscope (Picoscope 6000 series) through the use of a diplexer (RDX-6, RITEC Inc.). The pulse-echo response of the wirelessly excited US were in agreement with previous results, with an operating frequency around 2 MHz as shown in Figure 4.12(b).

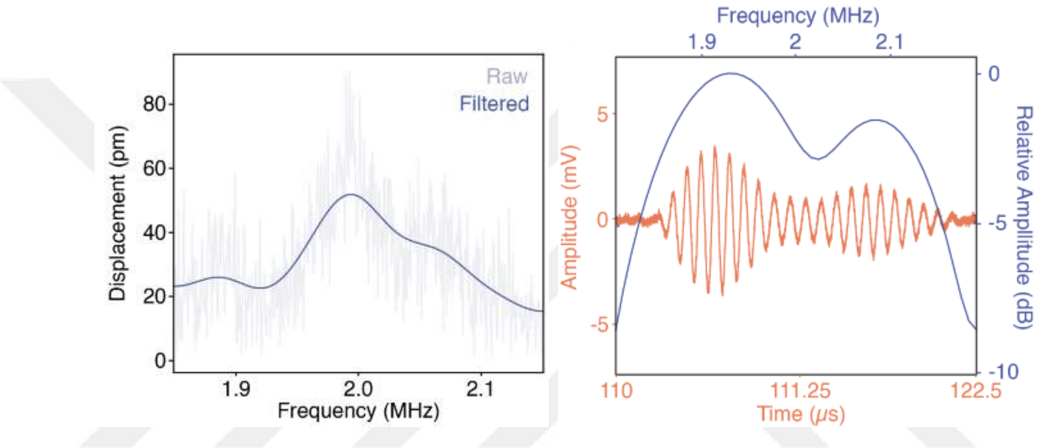

(a) (b)

Figure 4.12: Transducer Characterizations: (a) LDV measurements of the wirelessly excited US tag. (b) Pulse-echo response and derived frequency spectra of the wirelessly excited US tag.

To evaluate the underwater pressure field generated by the US tags, we conducted hydrophone measurements in longitudinal and transverse orientations, and observed no discrepancies as compared to conventional wired US transducers (Figure 4.13). These acoustic characterizations were conducted underwater inside an UMS Research system covered with acoustic absorbers (AptFlex F28, Precision Acoustics). Similar to pulse-echo response, the US tags were affixed inside the water tanks and T/R coils were aligned from outside. The longitudinal and transverse pressure field, and the bandwidth were evaluated with a 0.5 mm needle hydrophone (Precision Acoustics) connected to an oscilloscope (DSOX3024G, Keysight Technologies).

Coil misalignment in inductively coupled systems is a critical factor that affects both signal integrity and overall system performance. As expected, experiments with

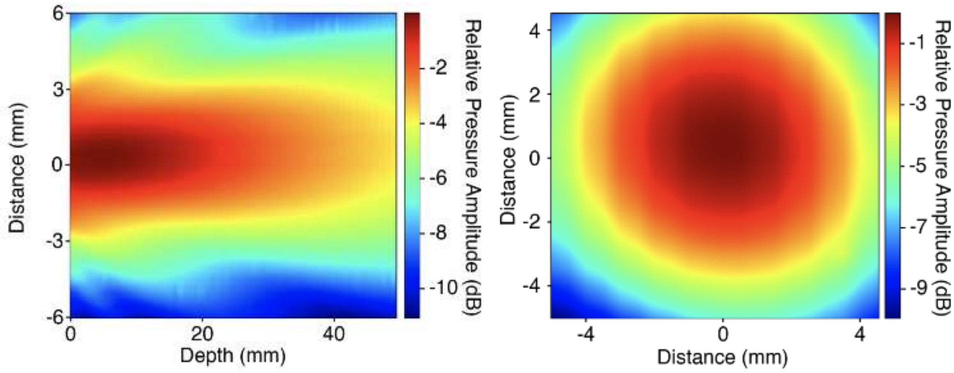

(a) (b)

Figure 4.13: Underwater pressure field scans in (a) longitudinal and transverse (b).

US tags showed a significant impact on the SNR due to coil misalignment. However, as shown in Figure 4.14, the primary measurement of the experiment—time-of-flight (TOF)—remained largely unaffected .

The misalignment experiments, which included angular misalignments up to 40°, lateral offsets up to 9 mm, and vertical gaps up to 9 mm, revealed that the SNR decreases as the misalignment increases. Specifically, a 9 mm lateral or vertical offset results in a reduction of up to 20 dB, while a 40° angular misalignment causes a drop of up to 13 dB (Figure 4.14). Despite these changes, TOF measurements remained consistent, with deviations of less than 1%. This indicates that, within typical usage scenarios, moderate misalignments do not compromise measurement accuracy.

The resilience of TOF measurements to misalignment is crucial for applications that US tags target, where TOF is the primary diagnostic metric. In these cases, signal degradation does not interfere with the ability to detect echo arrival times accurately, even under conditions of significant misalignment.

Nonetheless, extreme misalignments can significantly reduce signal quality, potentially causing weaker echoes to go undetected. In such cases, more precise coil alignment will be necessary to maintain high-quality signal reception. Ultimately, these findings indicate that while misalignment and motion can degrade signal quality, they do not significantly affect the core measurement accuracy of TOF.

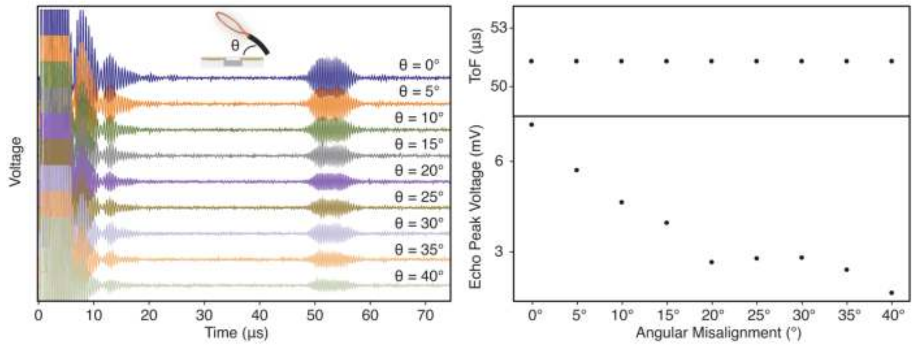

(a)

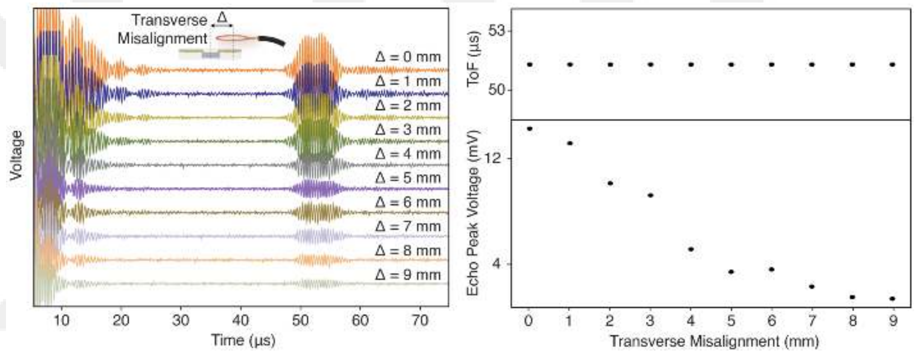

(b)

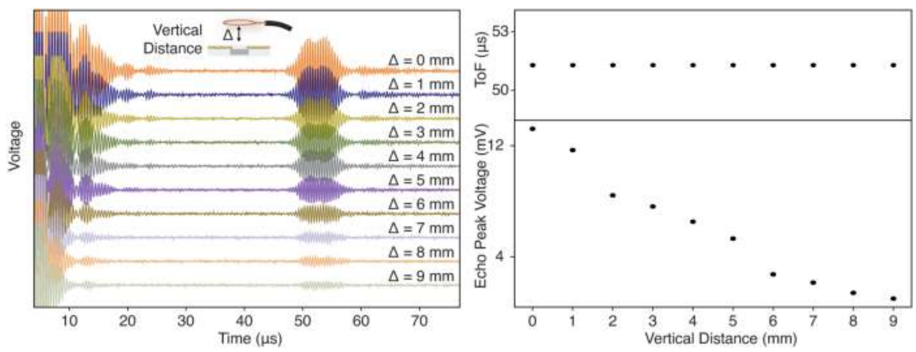

(c)

Figure 4.14: Effect of coil misalignment on the measured signal: (a) Angular misalignment, (b) Transverse misalignment, (c) Vertical distance.

4.4 In-vitro Evaluations

Following fabrication and characterization, US tags were integrated into two formats: a soft contact lens to enable out-of-clinic ocular ultrasound and an epidermal patch format for bladder volume monitoring using A-P distance measurements and blood pressure monitoring via vessel wall motion tracking. Considering the shapes of the eye and bladder, both axial eye length monitoring and bladder volume applications were simplified to diameter measurements of spherical or ellipsoid objects. To simulate these conditions, spherical-shaped round-bottom flasks were mounted on a motorized stage and submerged in DI water, with US tags attached inside the water tank. The patch was characterized using the in-vitro setup shown in Figure 4.15.

For eye and bladder monitoring, 25- and 50-mL flasks were used for the US contact lens, while 100, 250, and 500-mL flasks were employed for bladder monitoring. With the motorized stage, the flasks were aligned to maximize the time between echoes reflected from the anterior and posterior walls. AWG was used to excite the T/R coil, and echoes were recorded on the oscilloscope via a diplexer. The US tags emitted ultrasound waves, reflecting off the front and back walls of the flasks. By aligning the US tags to the flasks to maximize echo signal strength, the diameter of the flasks was determined using time-of-flight measurements.

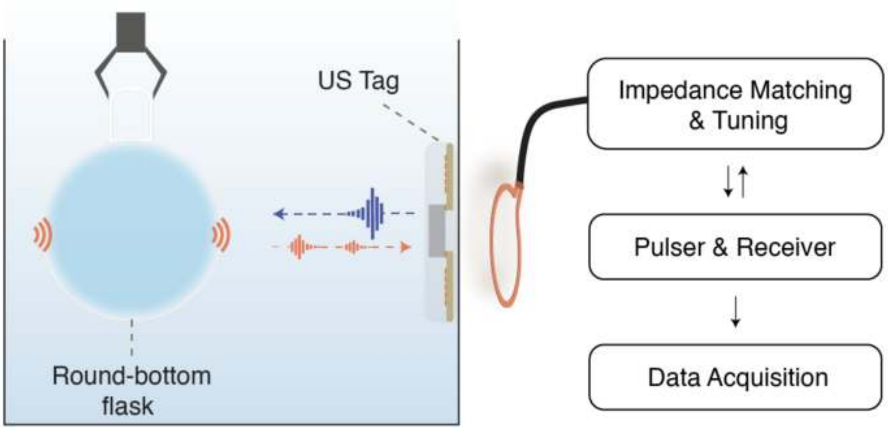

Figure 4.15: Schematic drawing of the in-vitro experimental setup with round-bottom flasks acting as the bladder and/or the eye.

As shown in Figure 4.16(a), the wireless US tags produced diameter measurements with a mean relative error of less than 17 % when used with the alignment platform. The in-vitro eye monitoring performance was also tested using the setup in Fig. 14, where two round-bottom flasks (25- and 50-mL) with diameters of 4 and 5 cm were used to simulate the eye. As shown in Figure 4.16(b), the wireless US tags recorded diameter measurements with a mean relative error of less than 2 % when used with an alignment platform.

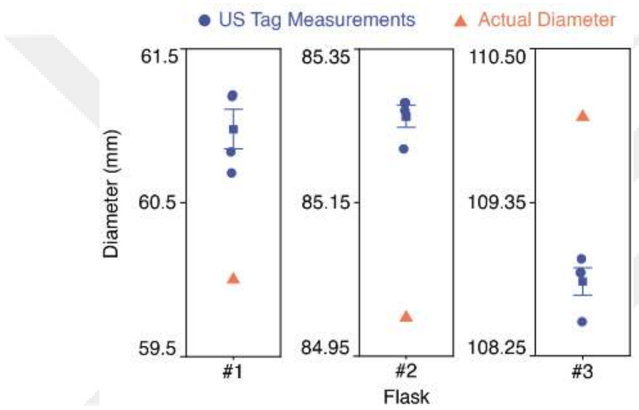

(a)

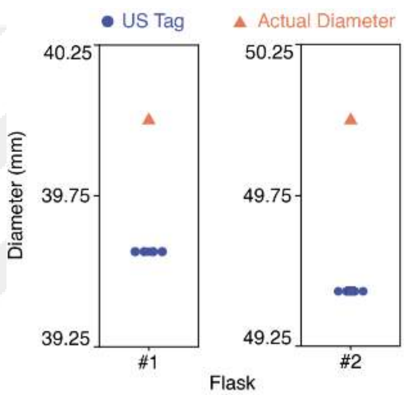

(b)

Figure 4.16: In-vitro demonstration of US tags for bladder and axial eye.

For further in-vitro characterization of the contact lens format (Figure 4.17(a)), the US tag was encapsulated in PDMS inside a 3D-printed mold with a curvature matching that of the eye phantom (VK-10222, Gampt mbH). The eye phantom, designed to mimic the eye's echogenic layers, was used in the demonstration of the US contact lens (Figure 4.17(b)). Upon wireless excitation, the US contact lens captured and transmitted echo signals from the eye phantom to the external T/R coil for post-processing. The US contact lens was further tested in an ex-vivo setup (Figure 4.18(a)), where artificial eye elongation was induced using a syringe pump to inject deionized water into enucleated eyes. The vitreous chambers of the eyes were cannulated to allow water injection, which caused elongation of the axial eye length due to increased pressure. After each 0.5 mL injection, pulse-echo measurements were performed using the in-vitro setup. Received echoes were

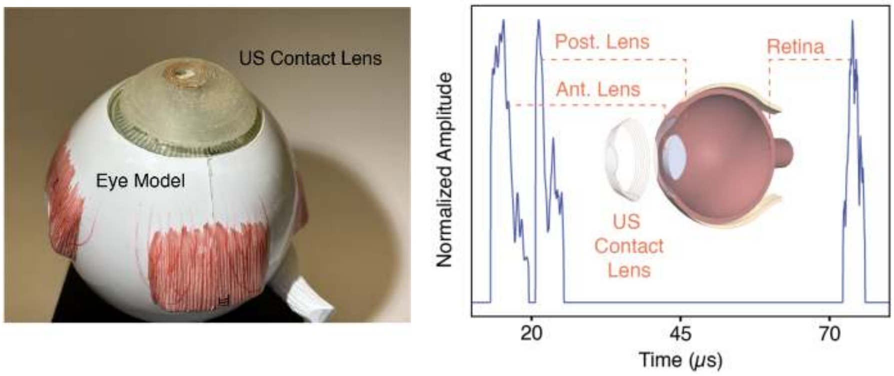

(a) (b)

Figure 4.17: In-vitro demonstration of US tags with eye phantom.

processed through band-pass filtering, time-gain compensation, and amplification. The increased pressure from the injected water led to eye elongation, and as shown in Figure 4.18(b), the US contact lens detected this elongation through shifting echo signals. As the injected water increased pressure, the structures causing the echoes moved further away from the US contact lens, resulting in delayed echo peaks, which provided information on the amount of elongation.

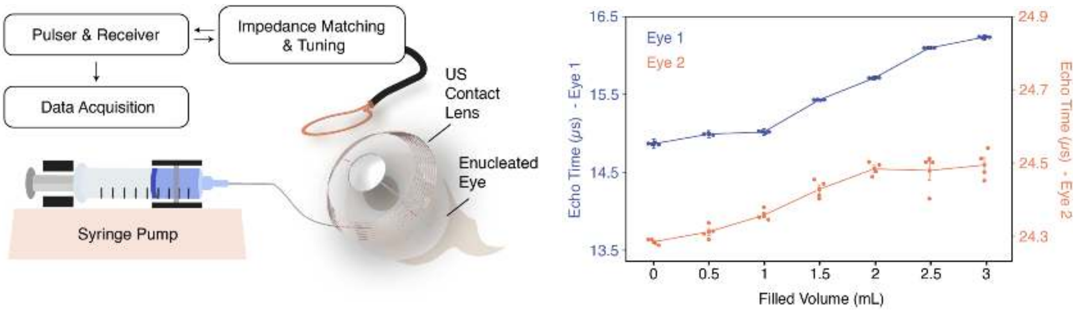

(a) (b)

Figure 4.18: Ex vivo demonstration of US tags.

For the in-vitro characterization of the blood pressure and heart rate monitoring Us tag, a pulsatile pump (SuperPump, ViVitro Labs) with a silicone rubber vessel was used to simulate a physiological flow profile of 70 beats per minute. The experimental setup for in-vitro characterization is shown in Figure 4.19(a). This setup was integrated with a custom water tank containing the pulsating silicone vessel. As in previous underwater tests, the US tag was aligned with the pulsating vessel and secured to the water tank wall. The T/R coil, positioned with the US tag, was excited by the AWG and amplifier (F30PV, Pendulum).

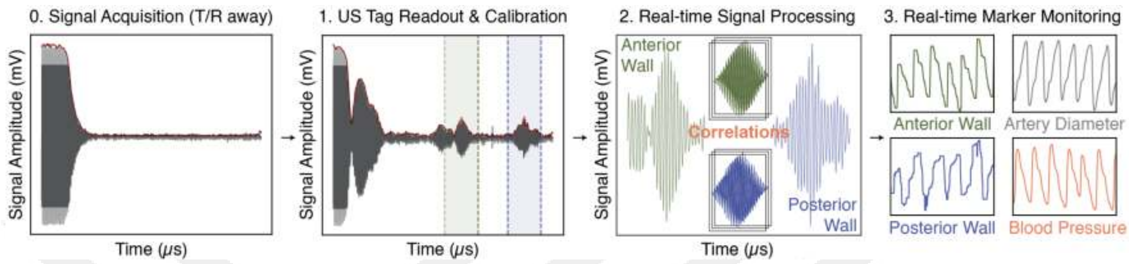

(a)

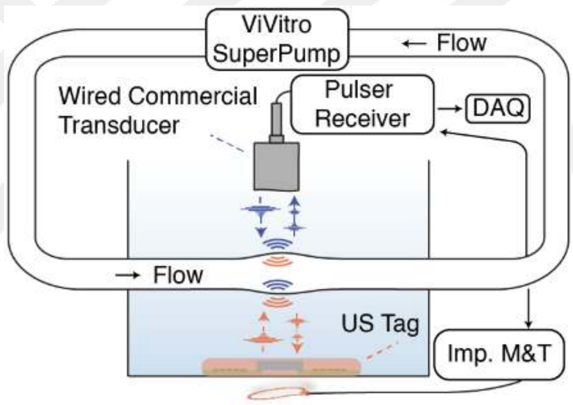

(b)

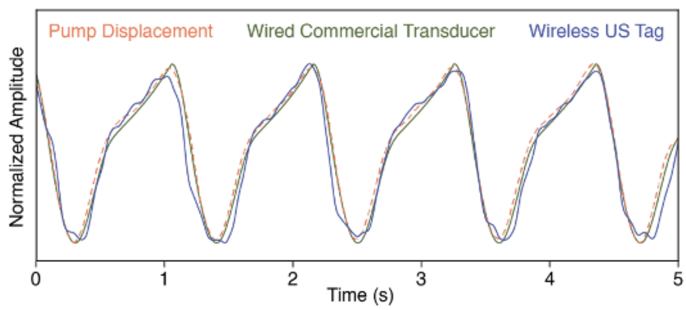

(c)

Figure 4.19: In-vitro blood-pressure monitoring demonstration of US tags.

The flow was monitored using both a commercial transducer connected to bench-top instruments and the US tag wirelessly coupled to the external T/R coil. Displacement data from the pulsatile movement of the silicone vessel walls was recorded for both systems and processed to derive pressure values. The results, presented in Figure 4.19(b), show excellent agreement between the two measurement methods over extended periods. All phases of the cycle with distinct points were visible. As briefly described in Figure 4.19(c), cross-correlation of the band-pass filtered echo signals from the dynamic walls of the vessel were used to quantify the artery wall movement.

4.5 In-vivo Demonstrations & Applications

The performance of the epidermal US patch was further demonstrated in-vivo on a healthy volunteer. Measurements were taken at 10 minute intervals while the US tag was placed on the lower abdomen. For ultrasound imaging, ultrasound probe was manually placed longitudinal and transverse orientation until the maximum dimensions of the bladder was observed on the scanner's screen and recorded. Length, width and height dimensions of the bladder were then manually determined by caliper placement on the recorded images. Finally, prolate ellipsoid volume method was used to estimate the bladder volume from the recorded US images. As previously mentioned, the echo signals from the anterior and posterior walls of the bladder can act as a surrogate measure for the actual bladder volume. Similar to the in-vitro characterization setup, the ultrasound waves emitted by the US tag reflect from various interfaces within the body. Since the bladder is filled with urine, the most distinct signals come from the anterior and posterior walls of the bladder. As urine accumulates, the bladder expands, and it contracts again when urine is voided.

The varying A-P distance is a result of this act of continuous expansion and shrinking of the bladder and can be monitored by the echo signals coming from the A-P walls as seen in Figure 4.20(a). The results of the wireless US tag-based A-P distance measurements in comparison to ultrasound imaging-based volume calculations are presented in Figure 4.20(b). A similar trend between the results of two modalities supports the findings of previous works on the use of A-P distance and highlights the capability of the US tag based epidermal patch to conduct wireless

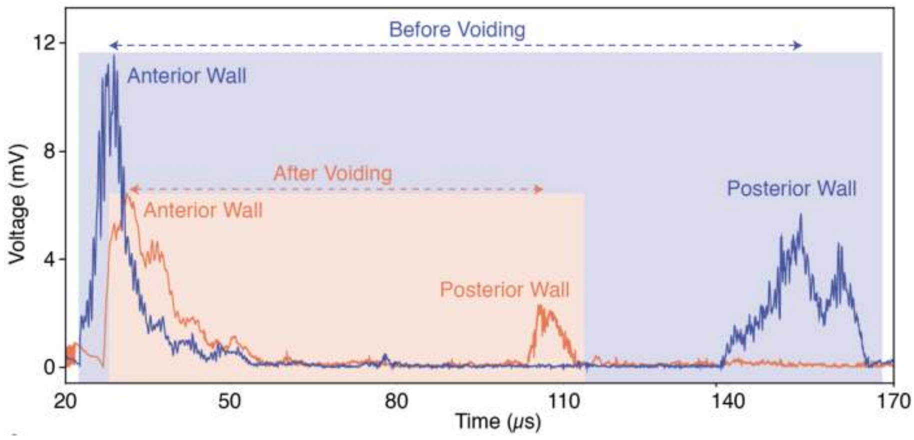

(a)

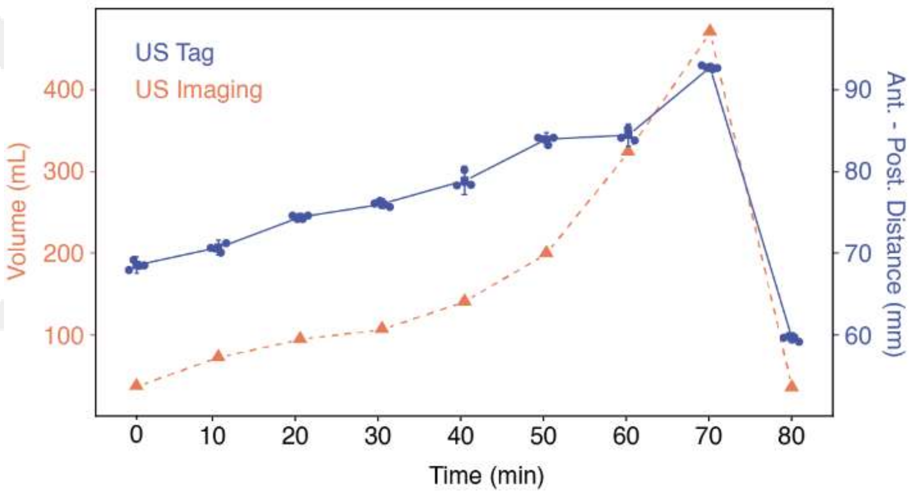

(b)

Figure 4.20: In vivo bladder volume measurements of the US tags: (a) Representative ultrasonic measurements of the full (blue) and empty (orange) bladder. (b) Extended monitoring during a full micturition cycle with conventional ultrasound imaging (orange) and the anterior-posterior distance measurement with the US tag (blue). All data points are displayed (n=4) and the measurements are presented as the mean $\pm$ 2 s.d.

and battery-less A-P distance measurements.

For proof-of-concept, in-vivo blood pressure monitoring capability of the device was demonstrated on a healthy volunteer. The US tag in epidermal US patch format was manually positioned by the volunteer according to the ultrasound images taken by a commercial probe. When the T/R coil is excited, only the transmit waveform is

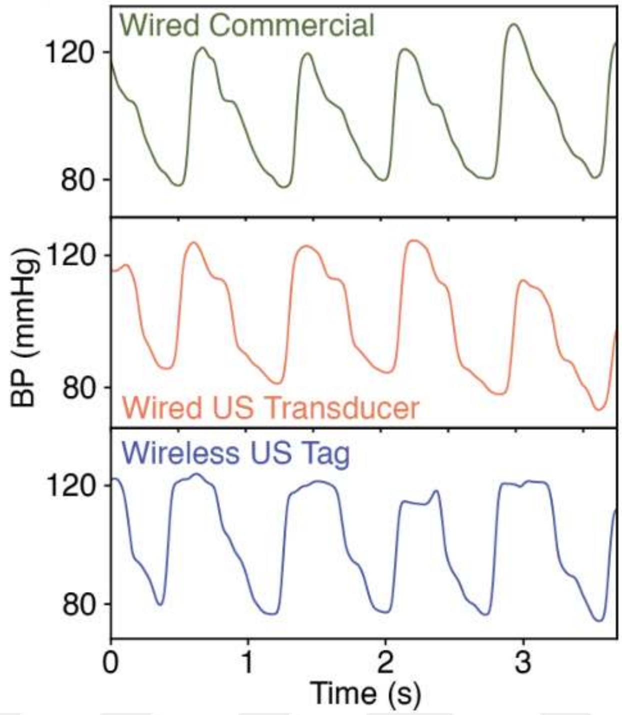

Figure 4.21: Comparison of the blood pressure measurements obtained by a commercial ultrasonic transducer, wired US tag ultrasonic transducer and wireless US tags.

observed on the oscilloscope screen without any echoes. As the T/R coil is brought in close proximity of the US tag, distinct echoes can be seen. The echo movements are then translated into artery diameter and blood pressure readings by a custom algorithm. Representative BP waveforms from a commercial ultrasonic transducer, the ultrasonic transducer of the US tag in wired form and wireless US tags are shown in Figure 4.21. The wirelessly coupled US tag successfully captured the major changes in the cardiac cycle. When the coils are decoupled, the echo signals from the artery walls disappear. In accordance with the reported methods, the pressure values from a commercial cuff measurement were used for the calibration, and systolic and diastolic pressure values from the US tags were taken as the mean values recorded during a 5-second interval. Based on these US tags accurately captured the heart rate and the blood pressure values when compared with the values obtained from the cuff measurements.

Lastly, to evaluate the long-tern wearability aspect of the US tags, an in vivo study targeting muscle activity monitoring was conducted. A US tag was adhered to the forearm of a subject for 24 hours to evaluate its reliability during periodic and on-demand muscle monitoring. Throughout this timeframe, the tag maintained stable adhesion and provided consistent signal fidelity as shown in Figure 4.22 and Figure 4.23. No significant degradation was observed, indicating reliable performance over extended wear. Importantly, no skin irritation or discomfort upon tag removal was observed, suggesting its suitability for routine, daily use.

4.6 Discussion

Clinical adaptation of wearable ultrasonic devices is still at its infancy due to several technological barriers, including size constraints, energy management, and integration challenges—areas directly addressed by the US tags. Firstly, albeit the sensor miniaturization efforts, the use of centimeter-scale rigid electronic components and batteries for physiological monitoring and wireless data transmission impedes the transition from large and bulky systems. In addition, the power demand of wearables increases as the sensors become more sophisticated and multiplexed.

Inspired by researchers from various fields who utilized wireless signal transmission between two coils to overcome these challenges, US tags were introduced to tackle major problems in wearable ultrasound technology. The footprint of the device is drastically reduced by removing both the electronics and the battery. This miniaturized form factor not only improves wearability for existing applications but also enables new applications, such as out-of-clinic ophthalmologic ultrasound, for the first time. Moreover, existing wired approaches require dedicated electronics and batteries for each application. With the separation of the control electronics and the ultrasonic transducers, a single device can be used to conduct measurements with all worn US tags.

Future work could focus on the optimization of the ultrasonic transducers of the US tags for specific applications. While the current implementation focuses on A-mode and M-mode ultrasound, which are well-established for localized clinical

Figure 4.22: Photos of the US tag taken during a 24-hour period.

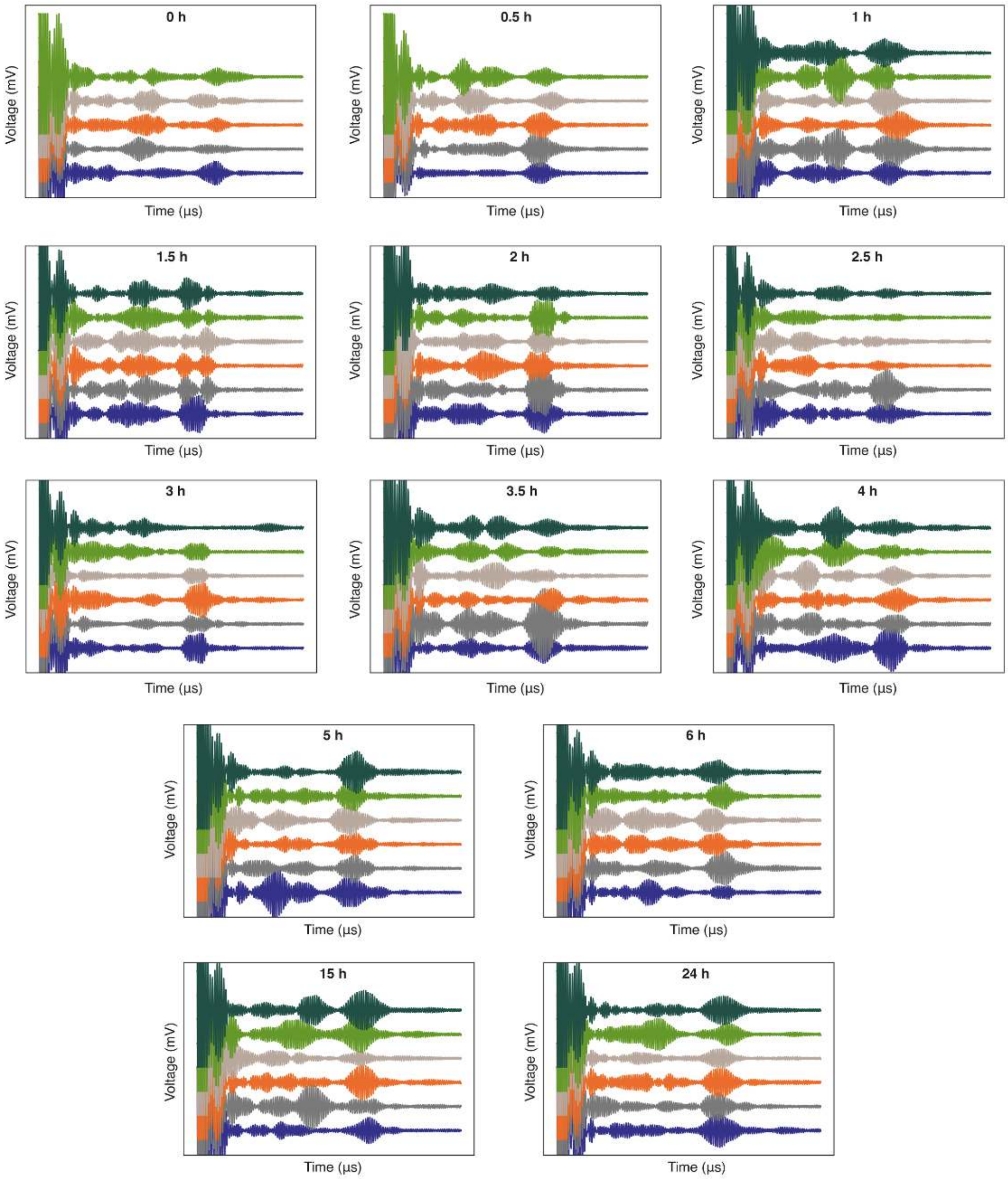

Figure 4.23: Long-term performance of the US tags.

assessments, the importance of expanding its capabilities to support more advanced imaging modalities will be critical. One inherent limitation of the current design is that each piezo–coil unit operates at a single frequency channel, restricting simultaneous array operation. A promising approach to achieving this involves transitioning to multi-layer PCB coils, which provide higher inductance while occupying a smaller footprint. This enhancement would allow multiple transducer–coil pairs to be incorporated within a compact configuration while maintaining adequate isolation between them. Future research could focus on overcoming associated challenges, including potential coil-to-coil crosstalk and refining multi-channel signal processing techniques for integrating B-mode imaging and multi-element beamforming, enabling anatomical imaging.

Another key consideration for translation is the proximity requirement of the US tag. The system relies on near-field inductive coupling, meaning that the external interrogator coil must be placed in close proximity to the tag for effective signal transmission. While this may initially seem restrictive, it aligns well with existing near-field communication (NFC) technologies, such as contactless payment systems, which also operate within a few centimeters. In practical use, a wrist-mounted or handheld interrogator coil can be positioned within millimeters to a few centimeters of the tag, ensuring a convenient and wire-free experience. This approach is particularly well-suited for on-demand measurements, where users or clinicians can briefly position the coil as needed for intermittent ultrasound scans rather than requiring continuous remote monitoring. Many applications, such as muscle activity assessment or bladder volume monitoring, naturally lend themselves to this operational paradigm, making short-range coupling both practical and effective. Nevertheless, the current readout scheme could be further miniaturized and integrated into truly portable devices, potentially interfacing with smartphones or tablets to enable rapid, real-time diagnostics and telemedicine applications.

Ultimately, the wireless US tag is envisioned as a foundational building block for a new generation of health monitoring technologies. By prioritizing user comfort, minimal maintenance, and seamless integration into daily life, the system represents a meaningful step toward practical, non-invasive ultrasound-based diagnostics. Continued advancements in miniaturized piezoelectric materials, multi-frequency transducer architectures, and intelligent signal processing are expected to further enhance its capabilities, enabling broader adoption in both clinical and consumer health applications.

Chapter 5

ELECTRONICS-FREE ULTRASONIC COMMUNICATION FOR MEDICAL IMPLANTS

5.1 Introduction

Monitoring vital signs deep within the body is a major challenge in healthcare. Since many diseases originate in deeper tissues, measurements on or close to the skin surface often fail to provide valuable clinical information. While medical imaging modalities like ultrasonography and magnetic resonance imaging allow non-invasive access, they are not suitable for continuous, in-situ monitoring. Although invasive methods, such as those involving catheters, can provide such continuous monitoring, they are typically limited to clinical settings and require specialized personnel. Furthermore, the discomfort and risk of infection associated with these procedures limit their frequent and long-term application. Therefore, the development of wireless implants for deep-tissue vital sign monitoring presents a compelling and attractive alternative [Sonmezoglu et al., 2021].

On the other hand, conventional active wireless implants, which often require application-specific integrated circuits for both power and data transmission, highlight the need for simpler communication approaches. Passive communication methods relying on electromagnetic waves face significant limitations due to signal attenuation in biological tissues [Sonmezoglu et al., 2021]. In contrast, passive ultrasound communication, which eliminates the need for complex active electronics within the implant and exhibits strong penetration capabilities in deep tissue, offers substantial potential for a new era of non-invasive and miniaturized implants for continuous deep-tissue health monitoring. In our research group, we have previously demonstrated a passive ultrasonic communication method that could be utilized with any implantable capacitive sensor [Akhtar et al., 2021], [Yener et al., 2025]. This chapter will explore the next-generation of the method, focusing on a simpler interrogation scheme for wearable device compatibility (e.g the devices developed in the previous chapters) and the achievement of faster rates for monitoring dynamic and pulsatile mechanisms within the body.

5.2 System Design and Equivalent Circuit Modeling

Previous work was built on a lock-in amplifier (LIA) based interrogation scheme. Instead, to remove the LIA dependency and propose a simpler method, this chapter focuses on the simple and fundamental pulse-echo measurements to extract the information from the implant piezo.

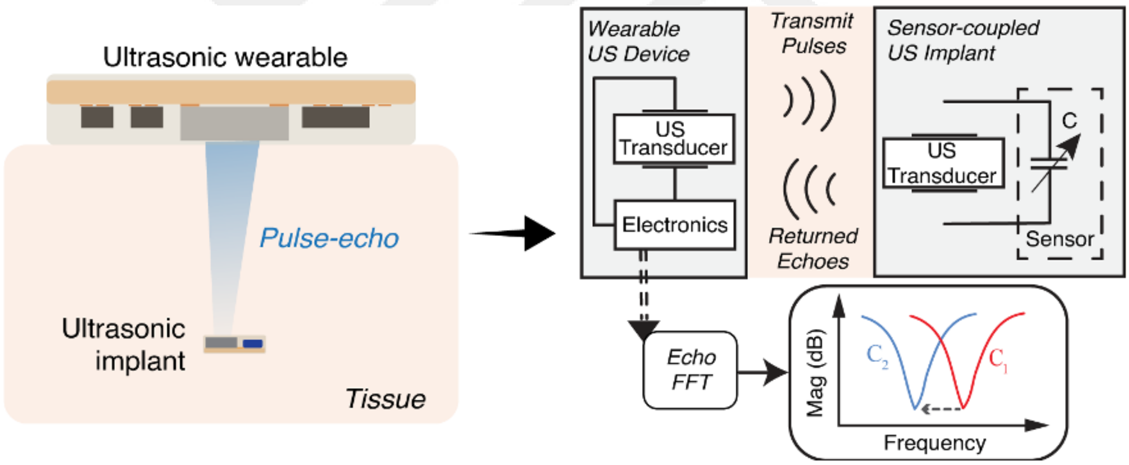

Figure 5.1: Conceptual schematic and building blocks of the proposed implant communication method.

The core concept is illustrated in Figure 5.1. Communication with sensor-coupled ultrasonic implants could be a core functionality of the wearable ultrasonic devices, such as the devices introduced in the earlier chapters. Since a wearable ultrasonic device is already capable of conducting pulse-echo measurements, the main idea is to understand and adapt these measurements such that they can be used to extract information from a sensor-coupled ultrasonic implant placed e.g. during an operation. The echo signal would then be analyzed by mainstream signal processing techniques, such as FFT, and sensory readings can be wirelessly obtained.

Building on the validated Leach ECM models from the previous chapters, a simulation of the communication link was built in LTSpice. The link consists of an external transducer (acting as an interrogator), the medium between the transducers (water or tissue), and an implant transducer designed to be coupled with a capacitive sensor. Similar to the previous implementations, the medium was modeled as a lossy transmission line connecting the interrogator transducer to the implant. Unlike air-backed transducers, the interrogator transducer was modeled with matching and backing layers, both represented as lossy transmission lines. To model a heavily backed, broad bandwidth interrogator transducer, arbitrary yet realistic material properties were used, including a backing layer speed of sound c_{BL} of 2400 m/s and a density ρ_{BL} of 6100 kg/m^3 along with a matching layer speed of sound c_{ML} of 3000 m/s and a density ρ_{ML} of 1200 kg/m^3.

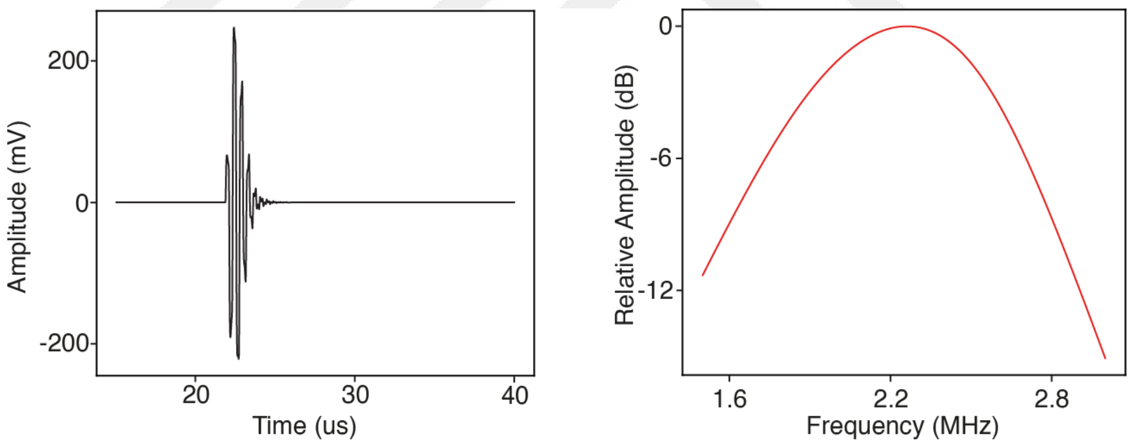

Figure 5.2: Pulse-echo response of the modelled interrogator transducer from a high impedance reflector with raw echo (left) and its FFT (right).

Initially, the pulse-echo response of the interrogator transducer with backing and matching layers was evaluated. As shown in Figure 5.2, the ringdown characteristics were improved and the fractional bandwidth was calculated to be approximately 45 %. The fractional bandwidth can be further improved by increasing the acoustic impedance of the backing layer material, which is 14.6 MRayl with the above-mentioned properties. Following the initial pulse-echo study, the link shown in Figure 5.3 was built.

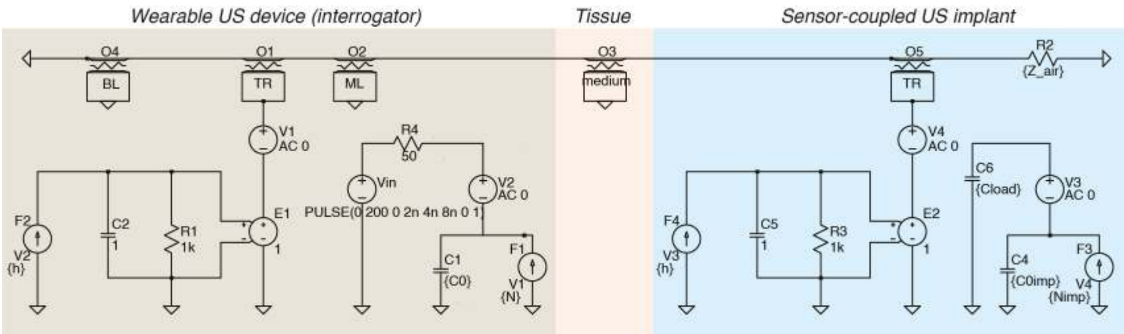

Figure 5.3: Leach ECM based communication link model implemented in LTSpice.

The ultrasonic implant from Chapter 3 was modeled with air-backing and without matching layer. Due to the absorption of the acoustic energy by the implant, the FFT of the echo signal displayed a sharp dip at the anti-resonance frequency of the implant as shown in Figure 5.4. This is also in agreement with the previous discussions on the acoustic reflection coefficient of a piezoelectric transducer [Allam et al., 2022], [Yener et al., 2025].

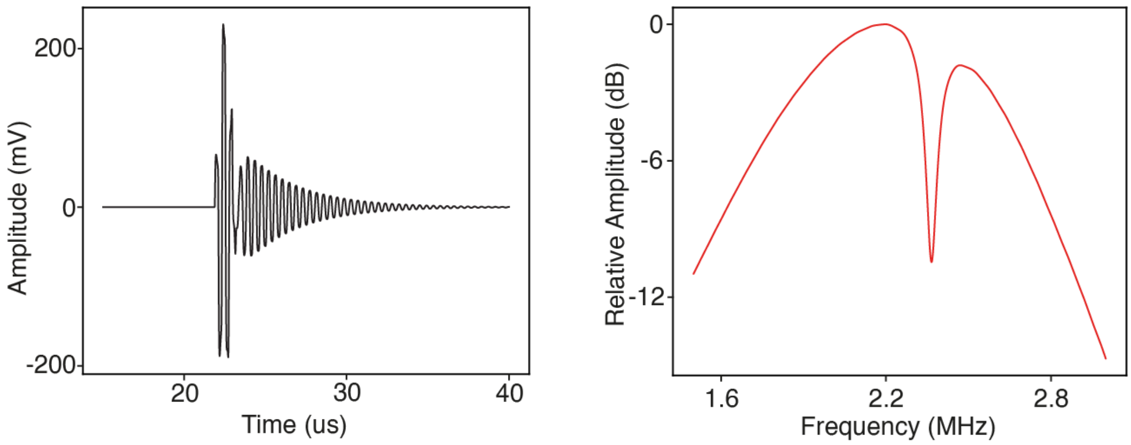

Figure 5.4: Pulse-echo response of the modelled interrogator transducer from an ultrasonic implant with raw echo (left) and its FFT (right).

With the addition of a parallel capacitor C_{load} to the ultrasonic implant, the anti-resonance frequency shifts as illustrated in Figure 5.5.

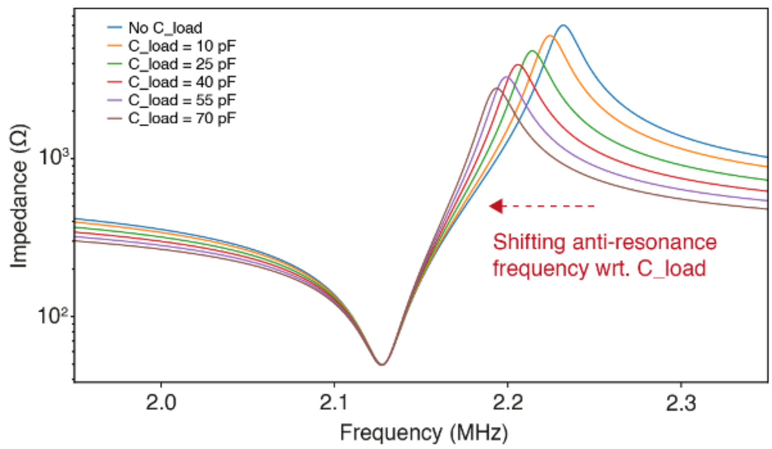

Figure 5.5: Effect of parallel capacitance on the anti-resonance frequency of a piezo-ceramic.

Furthermore, the acoustic reflection characteristic of the implant is also altered as depicted in Figure 5.6. The capacitance value of C_{load} was swept from 10 to 70 pF with step sizes of 15 pF. The FFT spectra of the received echo waveforms indicated a shift in the dip frequency as a result of a change in the electrical section of the implant.

This shifting behavior in the FFT is directly correlated with the load capacitance C_{load} of the ultrasonic implant, and allow the continuous and real-time measurements of the capacitance. These findings indicated that, when a capacitive sensor is coupled to the ultrasonic implant, changes in the sensor capacitance —resulting from a biomarker or physiological change of interest— can simply be monitored by pulse-echo measurements. Such a measurement scheme would enable rates of hundreds of Hz and remove the dependency on LIA.

5.3 In-vitro Demonstration

Based on the promising results, an in-vitro setup was built for validation. Firstly, a commercial immersion transducer (V323-SU, Olympus, USA) was characterized as the external interrogator transducer. As shown in Figure 5.7, the bandwidth of the transducer was calculated to be ≈ 65%, which justified its use as the interrogator.

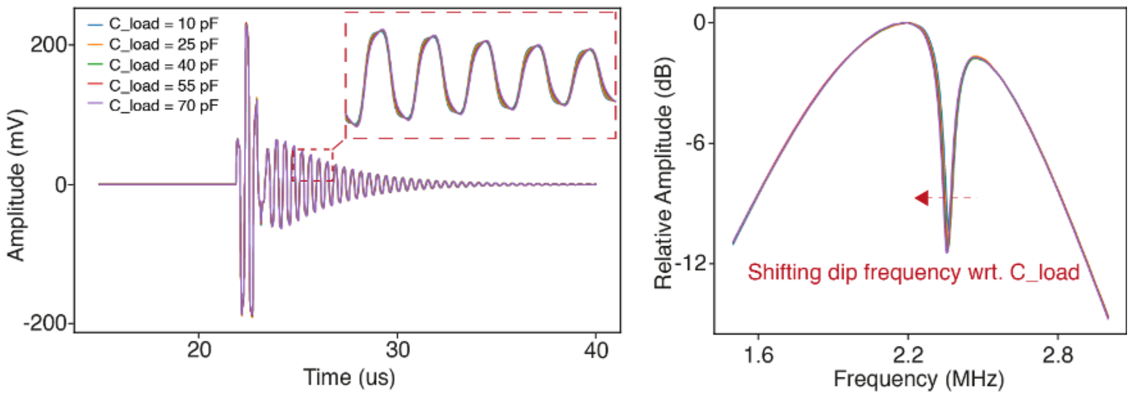

(a)

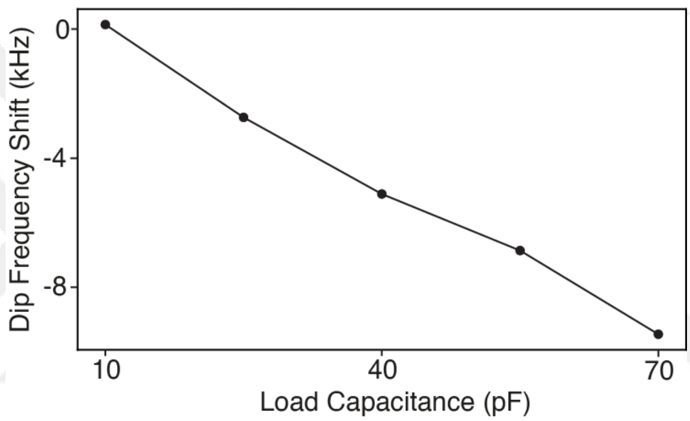

(b)

Figure 5.6: Communication link results from the ECM: (a) Pulse-echo response of the modelled interrogator transducer from a capacitor-coupled ultrasonic implant with raw echo (left) and its FFT (right). (b) Simulated requency shifts caused by varying load capacitance.

With this commercial transducer and the air-backed ultrasonic implant from Chapter 2, the experiment setup shown in Figure 5.8(a) was utilized for the measurements. Briefly, the commercial transducer was connected to a diplexer (RDX-6, RITEC, USA) which was connected to an AWG for transmit and an oscilloscope to receive. Prior to the pulse-echo measurements, transducers were coaxially aligned with the help of a manual stage, until maximum signal amplitude was observed. The ultrasonic implant was connected to a custom PCB with pins for capacitor (discrete and variable/trimmer) connections.

Despite the approximately ≈ 1 nF electrical capacitance of the ultrasonic im-

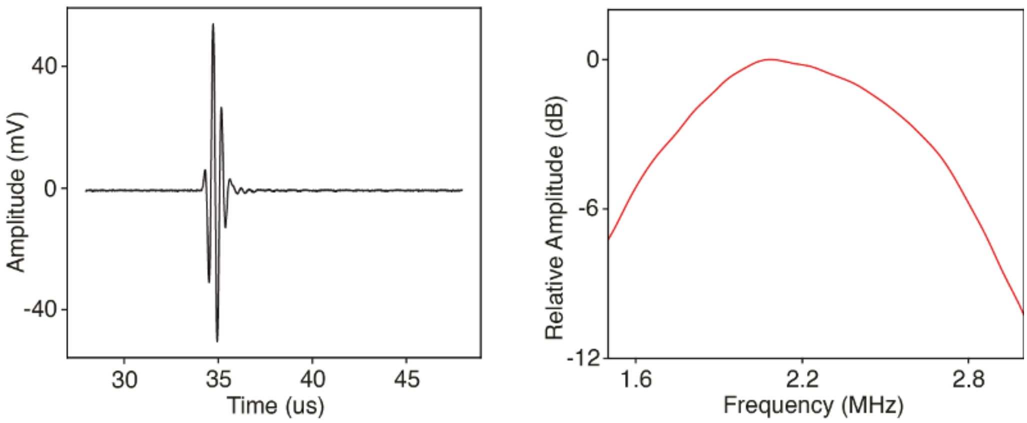

Figure 5.7: Echo and FFT of commercial broadband transducer as interrogator.

plant, the proposed method successfully captured clinically relevant tens of pF changes in the load capacitance. As illustrated in Figure 5.8(b), varying the sensor capacitance from 68 pF to 681 pF directly caused a major shift in the dip frequency, demonstrating the system's responsiveness to load changes. In addition, Figure 5.8(c) further confirms the sensitivity, showing distinct frequency shifts as capacitance increased across both a wider range (100-600 pF) and, more importantly, within the highly sensitive tens of pF range (5-25 pF). These results validate the method's ability to detect clinically relevant capacitive pressure sensor readings, even from an unoptimized implant.

To further evaluate the performance of the method and validate the temporal resolution, a transient-cyclic test was performed. During the experiment, the capacitance of the variable capacitor was periodically changed while the pulse-echo measurements were continuously conducted every 10 ms. The resulting plot in Figure 5.9 highlights the dynamic response and accurate capturing of the cyclic changes in capacitance over a 5-second period. This confirms the proposed method's high temporal resolution and real-time monitoring capabilities, which are essential for characterizing dynamic physiological events, including pulsatile activities.

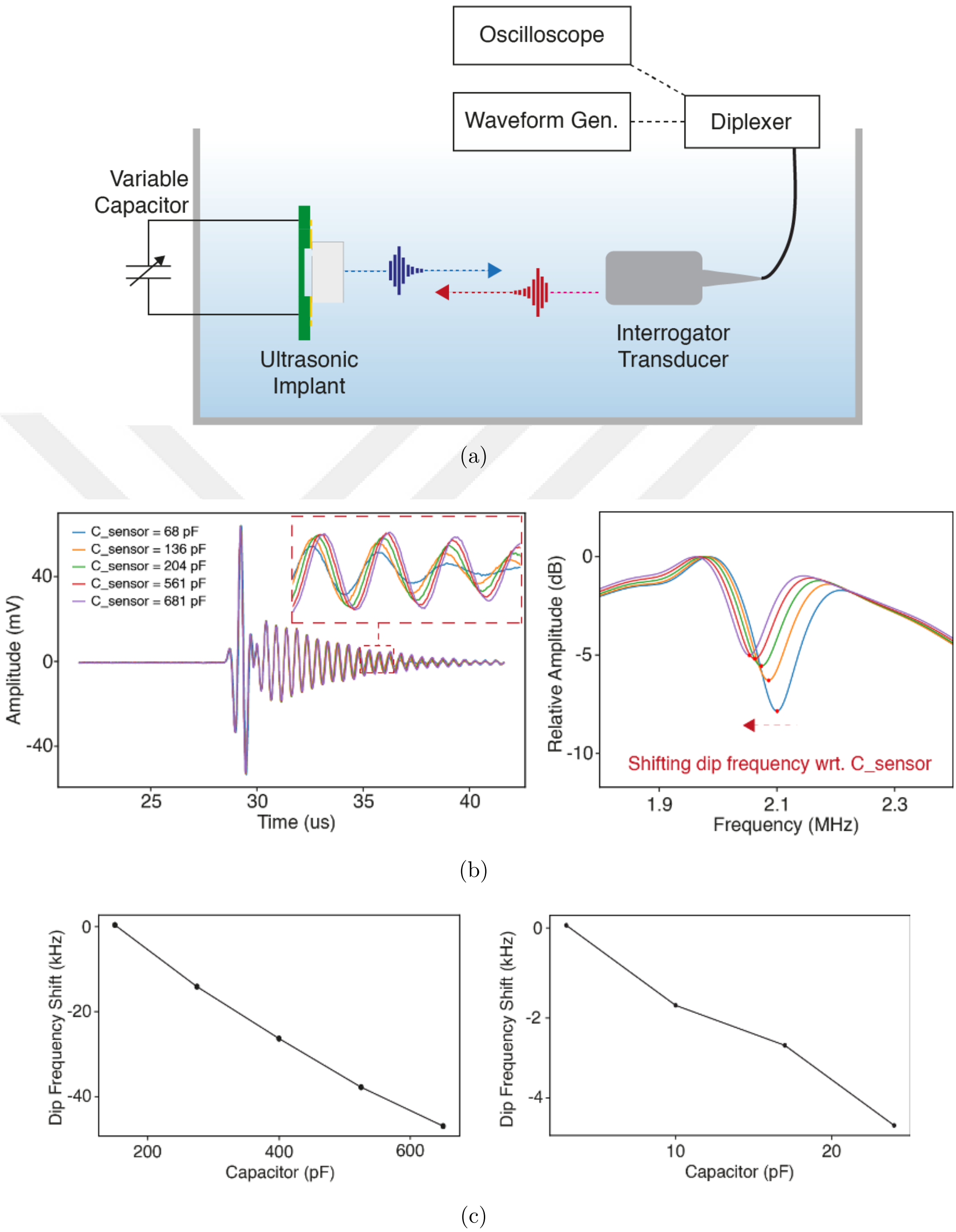

Figure 5.8: In-vitro communication link results: (a) Schematic of the communication setup. (b) Frequency shift in the FFT of the echo caused by the varying load capacitance. (c) Measured frequency shifts caused by varying load capacitance.

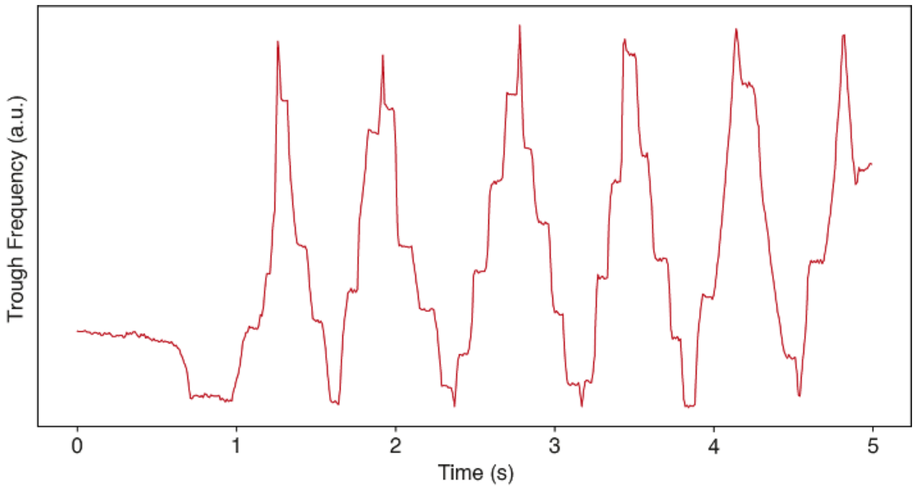

Figure 5.9: Long duration measurements with periodic capacitance changes.

5.4 Discussion

Medical implants often require complex CMOS electronics for effective power and data transfer to monitor vital health parameters deep within the body. Although passive communication with implants is an area of growing interest, electromagnetic-based methods have generally suffered from limited penetration depths. Ultrasound is an emerging and promising technology that overcome such issues, which was the focus of prior works in our group. Nevertheless, previously introduced LIA-based interrogation schemes and slow data rates (approximately 1 Hz) have been a major limitation for integration with wearable ultrasonic devices. To offer a simpler use with wearables and enable dynamic process monitoring, this chapter specifically explored the use of fundamental pulse-echo measurements for extracting information from ultrasonic implants. Extending beyond the diagnostic capabilities, the ability to communicate with sensor-coupled ultrasonic implants could become a core functionality of wearable ultrasonic devices, such as those discussed in earlier chapters.

The proposed method addresses the mentioned challenges by leveraging the frequency spectrum content of the echo signals. Validation of the method was achieved by ECM studies and in-bitro experiments. Compared to prior work, this approach is directly applicable with wearable ultrasonic devices, while preserving the key advantage of the method, which is the ability to couple any capacitive sensor with the implant. Moreover, the time-consuming nature of sweep-based methods has been substantially improved.

Despite the promising proof-of-concept results presented in this chapter, major work is required for a deeper understanding and translation of the method. Firstly, misalignment of the transducers is a major concern, which has to be further characterized and understood. Moreover, the demonstrations utilized a transducer with a relatively high SNR owing to the large aperture. Further work is needed to assess the miniaturization potential of the implant, and its relation to the sensivitity of the method. Ultimately, the findings of the chapter offer a new direction in the passive implant communication field with a huge potential for a wearable device coupled monitoring system.

Chapter 6

CONCLUSION & FUTURE WORK

As evidenced by the impact of wearable continuous glucose monitoring systems on patient lives, wearable technologies are poised to revolotinize healthcare towards a new era of personalized medicine. Among the all exciting breakthroughs, wearable ultrasound has a special place owing to its non-invasive ability for deep tissue penetration, enabling hidden information under the skin. Nevertheless, the transition from the bulky ultrasound equipment is facing major technological hurdles such as device size, power management and wearability. The central goal of this doctoral work is to address these limitations to improve translational capabilities of the technologies and truly enable wearable ultrasound technology.

Initially, building blocks of ultrasound instrumentation were introduced, followed by a closer look at the heart of the technology: the ultrasound probe. Based on this overview, Chapter 2 laid the groundwork and justification for the selection of bulk piezoelectric transducer technology as the key component for subsequent chapters trough the design, fabrication and characterization of single element prototypes.

Building on Chapter 2, Chapter 3 presented the development of a fully integrated wearable ultrasonic device for continuous bladder volume monitoring. By eliminating the need for operators and bulky instruments, the proposed device addressed a critical clinical need in the management of lower uriniary tract dysfunctions. The performance of individual components and apabilities of the device were thoroughly characterized by in-vitro experiments and in-vivo demonstrations on 5 healthy volunteers.

To tackle the major challenges experienced in Chapter 3, Chapter 4 introduced a a paradigm shift and demonstrated US tags: an electronics-free approach to wearable ultrasound powered by inductive coupling. By moving the electronics and the battery away from the transducers, the US tags offer rastically reduced the on-body footprint of the device. Such a miniaturized form factor not only improves user comfort and wearability for existing applications but also enable entirely new applications, such as out-of-clinic ophthalmologic ultrasound.

Finally, Chapter 5 extended the utility of wearable ultrasonic devices by exploring their potential for passive communication with medical implants. To achieve this, the simple pulse-echo measurement was utilized to extract information from sensor-coupled implants, significantly improving the previous schemes. Most importantly, this developed technique is directly compatible with the developed wearable ultrasonic devices from the previous chapters, paving the way for real-time monitoring of internal physiological parameters by wearable ultrasonic systems.

The developed devices and proposed methods in this thesis form a strong basis for the emerging field of wearable ultrasound technology. Nevertheless, future work is essential to improve the capabilites of these technologies and translation to clinical applications. More specifically:

- Despite the less promising results of piezopolymer based PMUTs, exciting improvements are taking place both from a piezoelectric material (e.g. improved coefficients with sputtered PZT or Scandium-doped AlN) and PMUT structure perspective (e.g. bimorph PMUTs). These improvements will most likely enable their integration into wearable devices. When coupled with CMOS electronics, they could offer significantly reduced footprint solutions for applications like the bladder volume monitoring.

- With improvements in the number of elements and packaging of the bladder volume monitoring device, a clinical study including patients with demonstrated LUTD conditions could offer crucial insights in the translation of the device to the clinics.

- Electronics-free US tags offer a new tool in the arsenal of wearable ultrasound technologies. Building on the proof-of-concept studies in this thesis, further optimization on the electronics aspects of the system could offer improved performances. For instance, current interrogation is based on benchtop equipment or an evaluation board of a pulser IC. Development of an external reader coupled to a mobile phone would greatly improve the applicability of the device. In addition, use of multi-layer coils could be utilized to increase the number of transducers to a point that would lead to simple B-mode images.

- A key step in the ultrasound communication with implants is the investigation of the misalignments and developments of the new methods that would compensate for the potential false readings. Conventional feature extraction methods or deep learning techniques could be used for such purpose. In addition, in paralel with the development of PMUT technology, the effect of miniaturization and the aperture of the implant could be further investigated to improve the design space.

BIBLIOGRAPHY

[Abelson et al., 2019] Abelson, B. et al. (2019). Ambulatory urodynamic monitoring: state of the art and future directions. *Nature Reviews Urology*, 16:291–301.

[Akhtar et al., 2021] Akhtar, M. J., Toymus, A. T., Esat, K., and Beker, L. (2021). Frequency-based ultrasonic backscatter modulation for passive sensing applications.

[Allam et al., 2022] Allam, A., Bhardwaj, A., Sabra, K., and Erturk, A. (2022). Piezoelectric transducer design and impedance tuning for concurrent ultrasonic power and data transfer. In Han, J.-H., Shahab, S., and Yang, J., editors, *Active and Passive Smart Structures and Integrated Systems XVI*, page 20. SPIE.

[Awedew et al., 2022] Awedew, A. F. et al. (2022). The global, regional, and national burden of benign prostatic hyperplasia in 204 countries and territories from 2000 to 2019: a systematic analysis for the global burden of disease study 2019. *The Lancet Healthy Longevity*, 3:e754–e776.

[Beker et al., 2025] Beker, L., Toymus, A., Peker, S., Atik, A., Yener, U., Albay, M., Yılgör, E., and Yılgör, (2025). Wirelessly-powered, electronics-free ultrasonic tags for continuous wearable health monitoring in epidermal and ocular applications.

[Bih et al., 1998] Bih, L. I. et al. (1998). Bladder shape impact on the accuracy of ultrasonic estimation of bladder volume. *Archives of Physical Medicine and Rehabilitation*, 79(12):1553–1556.

[Bledsoe and Zimmerman, 2021] Bledsoe, A. and Zimmerman, J. (2021). Ultrasound: The new stethoscope (point-of-care ultrasound). *Anesthesiology Clinics*, 39:537–553.

[Boutry et al., 2019] Boutry, C. M., Beker, L., Kaizawa, Y., Vassos, C., Tran, H., Hinckley, A. C., Pfattner, R., Niu, S., Li, J., Claverie, J., Wang, Z., Chang, J., Fox, P. M., and Bao, Z. (2019). Biodegradable and flexible arterial-pulse sensor for the wireless monitoring of blood flow. *Nature Biomedical Engineering*, 3(1):47–57.

[Bright et al., 2014] Bright, E., Cotterill, N., Drake, M., and Abrams, P. (2014). Developing and validating the international consultation on incontinence questionnaire bladder diary. *European Urology*, 66:294–300.

[Cochran, 2012] Cochran, S. (2012). *Piezoelectricity and basic configurations for piezoelectric ultrasonic transducers*, pages 3–35. Woodhead Publishing Series in Electronic and Optical Materials. Woodhead Publishing.

[de Jong et al., 1985] de Jong, N., Bom, N., Souquet, J., and Faber, G. (1985). Vibration modes, matching layers and grating lobes. *Ultrasonics*, 23:176–182.

[Desilets et al., 1978] Desilets, C., Fraser, J., and Kino, G. (1978). The design of efficient broad-band piezoelectric transducers. *IEEE Transactions on Sonics and Ultrasonics*, 25(3):115–125.

[Dicuio et al., 2005] Dicuio, M. et al. (2005). Measurements of urinary bladder volume: comparison of five ultrasound calculation methods in volunteers. *Archivio italiano di urologia, andrologia*, 77(1):60–62.

[Du et al., 2023] Du, W., Zhang, L., Suh, E., Lin, D., Marcus, C., Ozkan, L., Ahuja, A., Fernandez, S., Shuvo, I. I., Sadat, D., Liu, W., Li, F., Chandrakasan, A. P., Ozmen, T., and Dagdeviren, C. (2023). Conformable ultrasound breast patch for deep tissue scanning and imaging. *Science Advances*, 9(30).

[D'Ancona et al., 2019] D'Ancona, C. et al. (2019). The international continence society (ics) report on the terminology for adult male lower urinary tract and pelvic floor symptoms and dysfunction. *Neurourology and Urodynamics*, 38:433–477.

[Farhoudi et al., 2021] Farhoudi, N., Laurentius, L. B., Magda, J. J., Reiche, C. F., and Solzbacher, F. (2021). In vivo monitoring of glucose using ultrasound-induced resonance in implantable smart hydrogel microstructures. *ACS Sensors*, 6(10):3587–3595.

[Fitzgerald et al., 2022] Fitzgerald, R. C., Antoniou, A. C., Fruk, L., and Rosenfeld, N. (2022). The future of early cancer detection. *Nature Medicine*, 28:666–677.

[Fournelle et al., 2021] Fournelle, M. et al. (2021). Portable ultrasound research system for use in auto- mated bladder monitoring with machine-learning-based segmentation. *Sensors*, 21:6481.

[Gambhir et al., 2021] Gambhir, S. S., Ge, T. J., Vermesh, O., Spitler, R., and Gold, G. E. (2021). Continuous health monitoring: An opportunity for precision health. *Science Translational Medicine*, 13(597):eabe5383.

[Gammie et al., 2020] Gammie, A. et al. (2020). What developments are needed to achieve less-invasive urodynamics? ici-rs 2019. *Neurourology and Urodynamics*, 39:S36–S42.

[Gao et al., 2024] Gao, X., Chen, X., Lin, M., Yue, W., Hu, H., Qin, S., Zhang, F., Lou, Z., Yin, L., Huang, H., Zhou, S., Bian, Y., Yang, X., Zhu, Y., Mu, J., Wang, X., Park, G., Lu, C., Wang, R., Wu, R. S., Wang, J., Li, J., and Xu, S. (2024). A wearable echomyography system based on a single transducer. *Nature Electronics*, 7(11):1035–1046.

[Gijsenbergh et al., 2019] Gijsenbergh, P., Halbach, A., Jeong, Y., Torri, G. B., Billen, M., Demi, L., Huang, C.-H., Cheyns, D., Rottenberg, X., and Rochus, V. (2019). Characterization of polymer-based piezoelectric micromachined ultrasound transducers for short-range gesture recognition applications. *Journal of Micromechanics and Microengineering*, 29:074001.

[Giusti et al., 2023] Giusti, D., Gritti, A., Quaglia, F., Savoia, A. S., Sandoh, H., Klug, G., Hoshino, H., Rahul, D., Rao, V. S., Wee, D. H. S., Wakahara, M., and Shaw, M. (2023). Development of pmut array packaging from characterisation prototypes to customer samples. In *2023 IEEE 73rd Electronic Components and Technology Conference (ECTC)*, pages 1442–1449.

[Goss et al., 1979] Goss, S., Frizzell, L., and Dunn, F. (1979). Ultrasonic absorption and attenuation in mammalian tissues. *Ultrasound in Medicine and Biology*, 5(2):181–186.

[Hannah et al., 2019] Hannah, S., Brige, P., Ravichandran, A., and Ramuz, M. (2019). Conformable, stretchable sensor to record bladder wall stretch. *ACS Omega*, 4:1907–1915.

[Hu et al., 2023a] Hu, H., Huang, H., Li, M., et al. (2023a). A wearable cardiac ultrasound imager. *Nature*, 613:667–675.

[Hu et al., 2023b] Hu, H., Ma, Y., Gao, X., et al. (2023b). Stretchable ultrasonic arrays for the three-dimensional mapping of the modulus of deep tissue. *Nature Biomedical Engineering*, 7:1321–1334.

[Hu et al., 2018] Hu, H., Zhu, X., Wang, C., Zhang, L., Li, X., Lee, S., Huang, Z., Chen, R., Chen, Z., Wang, C., Gu, Y., Chen, Y., Lei, Y., Zhang, T., Kim, N., Guo, Y., Teng, Y., Zhou, W., Li, Y., Nomoto, A., Sternini, S., Zhou, Q., Pharr, M., di Scalea, F. L., and Xu, S. (2018). Stretchable ultrasonic transducer arrays for three-dimensional imaging on complex surfaces. *Science Advances*, 4(3).

[Huang et al., 2024] Huang, H., Wu, R. S., Lin, M., and Xu, S. (2024). Emerging wearable ultrasound technology. *IEEE Transactions on Ultrasonics, Ferroelectrics, and Frequency Control*, 71(7):713–729.

[Huang et al., 2022] Huang, Y., Shu, L., Hu, F., Liu, L., Zhou, Z., Cheng, Y.-Y.-S., Zhang, S., Li, W., Li, Q., Wang, H., Dong, Z., Wei, L., Luo, C., and

Li, J.-F. (2022). Implementing (k, na)nbo3-based lead-free ferroelectric films to piezoelectric micromachined ultrasonic transducers. *Nano Energy*, 103:107761.

[Irwin et al., 2011] Irwin, D. E., Kopp, Z. S., Agatep, B., Milsom, I., and Abrams, P. (2011). Worldwide prevalence estimates of lower urinary tract symptoms, overactive bladder, urinary incontinence and bladder outlet obstruction. *BJU International*, 108:1132–1138.

[Jensen and Svendsen, 1992] Jensen, J. and Svendsen, N. (1992). Calculation of pressure fields from arbitrarily shaped, apodized, and excited ultrasound transducers. *IEEE Transactions on Ultrasonics, Ferroelectrics, and Frequency Control*, 39(2):262–267.

[Jensen, 1997] Jensen, J. A. (1997). Field: A program for simulating ultrasound systems. volume 34, pages 351–353.

[Jo et al., 2021] Jo, H. G. et al. (2021). Forward-looking ultrasound wearable scanner system for estimation of urinary bladder volume. *Sensors*, 21:5445.

[Joseph et al., 2021] Joseph, J., Ma, B., and Khuri-Yakub, B. T. (2021). Applications of capacitive micromachined ultrasonic transducers: A comprehensive review. *IEEE Transactions on Ultrasonics, Ferroelectrics, and Frequency Control*, 69:456–467.

[Kanno et al., 2003] Kanno, I., Kotera, H., and Wasa, K. (2003). Measurement of transverse piezoelectric properties of pzt thin films. *Sensors and Actuators A: Physical*, 107(1):68–74.

[Karuthedath et al., 2023] Karuthedath, C. B., Sebastian, A. T., Helistö, P., Sillanpää, T., and Kärkkäinen, A. (2023). Development of scaln pmuts for medical applications. *Journal of Microelectromechanical Systems*, 32(5):505–512.

[Kenny et al., 2021] Kenny, J.-E. S., Munding, C. E., Eibl, J. K., et al. (2021). A novel, hands-free ultrasound patch for continuous monitoring of quantitative doppler in the carotid artery. *Scientific Reports*, 11(1):7780.

[Koven and Herschorn, 2022] Koven, A. and Herschorn, S. (2022). Nirs: past, present, and future in functional urology. *Current Bladder Dysfunction Reports*, 17:241–249.

[Koydemir and Ozcan, 2018] Koydemir, H. C. and Ozcan, A. (2018). Wearable and implantable sensors for biomedical applications. *Annual Review of Analytical Chemistry*, 11(1):127–146.

[Krimholtz et al., 1970] Krimholtz, R., Leedom, D., and Matthaei, G. (1970). New equivalent circuits for elementary piezoelectric transducers. *Electronics Letters*, 6(13):398–399.

[Kuzmić et al., 2003] Kuzmić, A. C., Brkljacić, B., and Ivanković, D. (2003). The impact of bladder shape on the ultrasonographic measurement of bladder volume in children. *Pediatric Radiology*, 33(8):530–534.

[Launer et al., 2021] Launer, B. M., McVary, K. T., Ricke, W. A., and Lloyd, G. L. (2021). The rising worldwide impact of benign prostatic hyperplasia. *BJU International*, 127:722–728.

[Leach, 1994] Leach, W. (1994). Controlled-source analogous circuits and spice models for piezoelectric transducers. *IEEE Transactions on Ultrasonics, Ferroelectrics, and Frequency Control*, 41(1):60–66.

[Lin et al., 2022] Lin, M., Hu, H., Zhou, S., and Xu, S. (2022). Soft wearable devices for deep-tissue sensing. *Nature Reviews Materials*, 7(11):850–869.

[Lin et al., 2023] Lin, M., Zhang, Z., Gao, X., Bian, Y., Wu, R. S., Park, G., Lou, Z., Zhang, Z., Xu, X., Chen, X., Kang, A., Yang, X., Yue, W., Yin, L., Wang, C., Qi, B., Zhou, S., Hu, H., Huang, H., Li, M., Gu, Y., Mu, J., Yang, A., Yaghi, A., Chen, Y., Lei, Y., Lu, C., Wang, R., Wang, J., Xiang, S., Kistler, E. B., Vasconcelos, N., and Xu, S. (2023). A fully integrated wearable ultrasound system to monitor deep tissues in moving subjects. *Nature Biotechnology*, 42(3):448–457.

[Liu et al., 2024a] Liu, H.-C., Zeng, Y., Gong, C., Chen, X., Kijanka, P., Zhang, J., Genyk, Y., Tchelepi, H., Wang, C., Zhou, Q., and Zhao, X. (2024a). Wearable bioadhesive ultrasound shear wave elastography. *Science Advances*, 10(6).

[Liu et al., 2024b] Liu, J., Liu, N., Xu, Y., Wu, M., Zhang, H., Wang, Y., Yan, Y., Hill, A., Song, R., Xu, Z., Park, M., Wu, Y., Ciatti, J. L., Gu, J., Luan, H., Zhang, Y., Yang, T., Ahn, H.-Y., Li, S., Ray, W. Z., Franz, C. K., MacEwan, M. R., Huang, Y., Hammill, C. W., Wang, H., and Rogers, J. A. (2024b). Bioresorbable shape-adaptive structures for ultrasonic monitoring of deep-tissue homeostasis. *Science*, 383(6687):1096–1103.

[Liu et al., 2022] Liu, Z., Yoshida, S., Horsley, D. A., and Tanaka, S. (2022). Fabrication and characterization of row-column addressed pmut array with monocrystalline pzt thin film toward creating ultrasonic imager. *Sensors and Actuators A: Physical*, 342:113666.

[Maini et al., 2024] Maini, L., Genovés, V., Furrer, R., Cesarovic, N., Hierold, C., and Roman, C. (2024). An in vitro demonstration of a passive, acoustic metamaterial as a temperature sensor with mk resolution for implantable applications. *Nature Microsystems and Nanoengineering*, 10(1).

[Mansoori et al., 2023] Mansoori, A., Hoff, L., Salmani, H., and Halvorsen, E. (2023). Electrode design based on strain mode shapes for configurable pmuts. *IEEE Open Journal of Ultrasonics, Ferroelectrics, and Frequency Control*, 3:88–100.

[Mason, 1964] Mason, W. P., editor (1964). *Physical Acoustics—Vol. 1*. Academic Press.

[Meng and Kiani, 2019] Meng, M. and Kiani, M. (2019). Gastric seed: Toward distributed ultrasonically interrogated millimeter-sized implants for large-scale gastric electrical-wave recording. *IEEE Transactions on Circuits and Systems II: Express Briefs*, 66(5):783–787.

[Moisello et al., 2024] Moisello, E., Novaresi, L., Sarkar, E., Malcovati, P., Costa, T. L., and Bonizzoni, E. (2024). Pmut and cmut devices for biomedical applications: A review. *IEEE Access*, 12:18640–18657.

[Molavi et al., 2013] Molavi, B., Shadgan, B., Macnab, A. J., and Dumont, G. A. (2013). Noninvasive op- tical monitoring of bladder filling to capacity using a wireless near infrared spectroscopy device. *IEEE transactions on biomedical circuits and systems*, 8:325–333.

[Morris and Perkins, 2012] Morris, P. and Perkins, A. (2012). Diagnostic imaging. *The Lancet*, 379:1525–1533.

[Muralt et al., 2005] Muralt, P., Ledermann, N., Paborowski, J., Barzegar, A., Gentil, S., Belgacem, B., Petitgrand, S., Bosseboeuf, A., and Setter, N. (2005). Piezoelectric micromachined ultrasonic transducers based on pzt thin films. *IEEE Transactions on Ultrasonics, Ferroelectrics, and Frequency Control*, 52(12):2276–2288.

[Mutlu et al., 2022] Mutlu, S., Aghakhani, A., and Sitti, M. (2022). Piezo capsule: Ultrasonic way of wireless pressure measurement. *Advanced Intelligent Systems*, 4(10).

[Nair et al., 2023] Nair, V. et al. (2023). Miniature battery-free bioelectronics. *Science*, 382:eabn4732.

[Nieuwhof-Leppink et al., 2019] Nieuwhof-Leppink, A. J., Schroeder, R. P., van de Putte, E. M., de Jong, T. P., and Schappin, R. (2019). Daytime urinary incontinence in children and ado- lescents. *The Lancet Child & Adolescent Health*, 3:492–501.

[Pala and Lin, 2022] Pala, S. and Lin, L. (2022). An improved lumped element model for circular-shape pmuts. *IEEE Open Journal of Ultrasonics, Ferroelectrics, and Frequency Control*, 2:83–95.

[Panicker et al., 2015] Panicker, J. N., Fowler, C. J., and Kessler, T. M. (2015). Lower urinary tract dys- function in the neurological patient: clinical assessment and management. *The Lancet Neurology*, 14:720–732.

[Phe et al., 2016] Phe, V., Chartier-Kastler, E., and Panicker, J. N. (2016). Management of neurogenic bladder in patients with multiple sclerosis. *Nature Reviews Urology*, 13:275–288.

[Piech et al., 2020] Piech, D. K., Johnson, B. C., Shen, K., Ghanbari, M. M., Li, K. Y., Neely, R. M., Kay, J. E., Carmena, J. M., Maharbiz, M. M., and Muller, R. (2020). A wireless millimetre-scale implantable neural stimulator with ultrasonically powered bidirectional communication. *Nature Biomedical Engineering*, 4(2):207–222.

[Redwood, 1961] Redwood, M. (1961). Transient performance of a piezoelectric transducer. *The Journal of the Acoustical Society of America*, 33(4):527–536.

[Roy et al., 2023] Roy, K., Lee, J.-E. Y., and Lee, C. (2023). Thin-film pmuts: a review of over 40 years of research. *Microsystems & Nanoengineering*, 9(1):95.

[Sadeghpour et al., 2022] Sadeghpour, S., Joshi, S. V., Wang, C., and Kraft, M. (2022). Novel phased array piezoelectric micromachined ultrasound transducers (pmuts) for medical imaging. *IEEE Open Journal of Ultrasonics, Ferroelectrics, and Frequency Control*, 2:194–202.

[Schlebusch et al., 2014] Schlebusch, T., Nienke, S., Leonhardt, S., and Walter, M. (2014). Bladder volume estimation from electrical impedance tomography. *Physiological Measurement*, 35:1813.

[Semproni et al., 2022] Semproni, F., Iacovacci, V., and Menciassi, A. (2022). Bladder monitoring systems: State of the art and future perspectives. *IEEE Access*, 10:125626–125651.

[Seo et al., 2016] Seo, D., Neely, R. M., Shen, K., Singhal, U., Alon, E., Rabaey, J. M., Carmena, J. M., and Maharbiz, M. M. (2016). Wireless recording in the peripheral nervous system with ultrasonic neural dust. *Neuron*, 91(3):529–539.

[Sherrit et al., 1999] Sherrit, S., Leary, S., Dolgin, B., and Bar-Cohen, Y. (1999). Comparison of the mason and klm equivalent circuits for piezoelectric resonators in the thickness mode. In *1999 IEEE Ultrasonics Symposium. Proceedings. International Symposium (Cat. No.99CH37027)*, volume 2, pages 921–926 vol.2.

[Shi et al., 2021] Shi, C., Andino-Pavlovsky, V., Lee, S. A., Costa, T., Elloian, J., Konofagou, E. E., and Shepard, K. L. (2021). Application of a sub–0.1-mm 3 implantable mote for in vivo real-time wireless temperature sensing. *Science Advances*, 7(19).

[Shikata et al., 2023] Shikata, K., Koshiba, Y., Horike, S., and Ishida, K. (2023). P(vdf/trfe) thin-film piezoelectric actuators sealed parylene c for medical micropumps. *physica status solidi (a)*, 220(24).

[Shung and Zippuro, 1996] Shung, K. and Zippuro, M. (1996). Ultrasonic transducers and arrays. *IEEE Engineering in Medicine and Biology Magazine*, 15(6):20–30.

[Smith et al., 2013] Smith, A., Bevan, D., Douglas, H. R., and James, D. (2013). Management of urinary incontinence in women: summary of updated nice guidance. *BMJ*, 347.

[Smyth and Kim, 2015] Smyth, K. and Kim, S.-G. (2015). Experiment and simulation validated analytical equivalent circuit model for piezoelectric micromachined ultrasonic transducers. *IEEE Transactions on Ultrasonics, Ferroelectrics, and Frequency Control*, 62(4):744–765.

[Smyth et al., 2017] Smyth, K. M., Sodini, C. G., and Kim, S.-G. (2017). High electromechanical coupling piezoelectric micro-machined ultrasonic transducer (pmut) elements for medical imaging. In *2017 19th International Conference on Solid-State Sensors, Actuators and Microsystems (TRANSDUCERS)*, pages 966–969.

[Sonmezoglu et al., 2021] Sonmezoglu, S., Fineman, J. R., Maltepe, E., and Maharbiz, M. M. (2021). Monitoring deep-tissue oxygenation with a millimeter-scale ultrasonic implant. *Nature Biotechnology*, 39(7):855–864.

[Tang et al., 2024] Tang, H., Yang, Y., Liu, Z., Li, W., Zhang, Y., Huang, Y., Kang, T., Yu, Y., Li, N., Tian, Y., Liu, X., Cheng, Y., Yin, Z., Jiang, X., Chen, X., and Zang, J. (2024). Injectable ultrasonic sensor for wireless monitoring of intracranial signals. *Nature*, 630(8015):84–90.

[Thuroff et al., 2011] Thuroff, J. W. et al. (2011). Eau guidelines on urinary incontinence. *Actas Urológicas Españolas (English Edition)*, 35:373–388.

[Tian et al., 2025] Tian, Y., Yang, Y., Tang, H., Wang, J., Li, N., Cheng, Y., Kang, T., Tang, J., Zhou, M., Chen, W., Yu, Y., Liu, X., Liu, X., Xu, L., Yin, Z., and Zang, J. (2025). An implantable hydrogel-based phononic crystal for continuous and wireless monitoring of internal tissue strains. *Nature Biomedical Engineering*.

[Toymus et al., 2022] Toymus, A. T., Bathaei, M. J., Akinci, S., Pala, S., and Beker, L. (2022). Design and fabrication of a p(vdf - trfe) based piezoelectric micromachined ultrasonic transducer with acoustic cavity. In *2022 IEEE International Ultrasonics Symposium (IUS)*, pages 1–3.

[Toymus et al., 2024] Toymus, A. T., Yener, U. C., Bardakci, E., et al. (2024). An integrated and flexible ultrasonic device for continuous bladder volume monitoring. *Nature Communications*, 15(1):7216.

[van Leuteren, 2020] van Leuteren, P. G. (2020). *Development, validation and implementation of a wearable ultrasonic bladder sensor for pediatric applications*. PhD thesis, University Library/University of Twente.

[van Leuteren et al., 2019] van Leuteren, P. G., Nieuwhof-Leppink, A. J., and Dik, P. (2019). Sens-u: clinical evaluation of a full-bladder notification–a pilot study. *Journal of Pediatric Urology*, 15:381–e1.

[van Neer et al., 2024] van Neer, P. L. M. J., Peters, L. C. J. M., Verbeek, R. G. F. A., Peeters, B., de Haas, G., Hörchens, L., Fillinger, L., Schrama, T., Merks-Swolfs, E. J. W., Gijsbertse, K., Saris, A. E. C. M., Mozaffarzadeh, M., Menssen, J. M., de Korte, C. L., van der Steen, J.-L. P. J., Volker, A. W. F., and Gelinck, G. H. (2024). Flexible large-area ultrasound arrays for medical applications made using embossed polymer structures. *Nature Communications*, 15(1).

[Vostrikov et al., 2025] Vostrikov, S., Tille, J., Benini, L., and Cossettini, A. (2025). Tinyprobe: A wearable 32-channel multimodal wireless ultrasound probe. *IEEE Transactions on Ultrasonics, Ferroelectrics, and Frequency Control*, 72(1):64–76.

[Wang et al., 2022] Wang, C. et al. (2022). Bioadhesive ultrasound for long-term continuous imaging of diverse organs. *Science*, 377:517–523.

[Wang et al., 2018] Wang, C., Li, X., Hu, H., et al. (2018). Monitoring of the central blood pressure waveform via a conformal ultrasonic device. *Nature Biomedical Engineering*, 2:687–695.

[Wang et al., 2021a] Wang, C., Qi, B., Lin, M., et al. (2021a). Continuous monitoring of deep-tissue haemodynamics with stretchable ultrasonic phased arrays. *Nature Biomedical Engineering*, 5:749–758.

[Wang et al., 2021b] Wang, F., Jin, P., Feng, Y., Fu, J., Wang, P., Liu, X., Zhang, Y., Ma, Y., Yang, Y., Yang, A., and Feng, X. (2021b). Flexible doppler ultrasound device for the monitoring of blood flow velocity. *Science Advances*, 7(44).

[Wang et al., 2025] Wang, M., Jia, L., Jia, X., Li, H., and Feng, X. (2025). Flexible circuit-free system via passive modulated ultrasound for wireless thoracic pressure monitoring. *Science Advances*, 11(8).

[Wong et al., 2024] Wong, S. J. Z., Roy, K., Lee, C., and Zhu, Y. (2024). Thin-film piezoelectric micromachined ultrasound transducers in biomedical applications: A review. *IEEE Transactions on Ultrasonics, Ferroelectrics, and Frequency Control*, 71(6):622–637.

[Yener et al., 2025] Yener, U. C., Toymus, A. T., Esat, K., Alem, M., and Beker, L. (2025). Passive ultrasonic communication link for deep-tissue sensor implants. *Device*, page 100755.

[Zhang et al., 2023] Zhang, L., Du, W., Kim, J., Yu, C., and Dagdeviren, C. (2023). An emerging era: Conformable ultrasound electronics. *Advanced Materials*, 36(8).

[Zhang et al., 2024] Zhang, L., Marcus, C., et al. (2024). A conformable phased-array ultrasound patch for bladder volume monitoring. *Nature Electronics*, 7:77–90.

[Zhou et al., 2014] Zhou, Q., Lam, K. H., Zheng, H., Qiu, W., and Shung, K. K. (2014). Piezoelectric single crystal ultrasonic transducers for biomedical applications. *Progress in Materials Science*, 66:87–111.

[Zhou et al., 2024a] Zhou, S., Gao, X., Park, G., Yang, X., Qi, B., Lin, M., Huang, H., Bian, Y., Hu, H., Chen, X., Wu, R. S., Liu, B., Yue, W., Lu, C., Wang, R., Bheemreddy, P., Qin, S., Lam, A., Wear, K. A., Andre, M., Kistler, E. B., Newell, D. W., and Xu, S. (2024a). Transcranial volumetric imaging using a conformal ultrasound patch. *Nature*, 629(8013):810–818.

[Zhou et al., 2024b] Zhou, S., Park, G., Longardner, K., Lin, M., Qi, B., Yang, X., Gao, X., Huang, H., Chen, X., Bian, Y., Hu, H., Wu, R. S., Yue, W., Li, M., Lu, C., Wang, R., Qin, S., Tasali, E., Karrison, T., Thomas, I., Smarr, B., Kistler, E. B., Khiami, B. A., Litvan, I., and Xu, S. (2024b). Clinical validation of a wearable ultrasound sensor of blood pressure. *Nature Biomedical Engineering*.

[Zou et al., 2024] Zou, F., Luo, Y., Zhuang, W., and Xu, T. (2024). A fully integrated conformal wearable ultrasound patch for continuous sonodynamic therapy. *Advanced Materials*.

Appendix A

PMUT NEUTRAL AXIS AND RESONANCE FREQUENCY CALCULATION

```
import numpy as np

# Define layer properties: [E (Pa), v, t (m), rho (kg/m3)]
layers = [
    [70e9, 0.17, 0.1e-6, 2200],      # Structural SiO2
    [168e9, 0.39, 0.35e-6, 21400],  # Bottom Electrode
    [80e9, 0.33, 1e-6, 7500],        # Piezo layer
    [168e9, 0.39, 0.1e-6, 21400],   # Top Electrode
    [8.5e9, 0.34, 50e-9, 1420],      # Polyimide
]
# Neutral axis calculation
def calculate_H_np(E, v, h, h_prev):
    nom = E * (h**2 - h_prev**2) / (1 - v**2)
    denom = E * (h - h_prev) / (1 - v**2)
    return nom, denom

H_np_nom_total = 0
H_np_denom_total = 0
h_prev = 0
for E, v, t, _ in layers:
    h = h_prev + t
    nom, denom = calculate_H_np(E, v, h, h_prev)
    H_np_nom_total += nom
```

```
    H_np_denom_total += denom
    h_prev = h

H_np = 0.5 * (H_np_nom_total / H_np_denom_total)
# Flexural rigidity D and mass per unit area miu
D_i_total = 0
miu_total = 0
h_prev = 0

for E, v, t, rho in layers:
    h = h_prev + t
    D_i = (1/3)*E*((h - H_np)**3-(h_prev-H_np)**3)/(1 - v**2)
    miu_i = t * rho
    D_i_total += D_i
    miu_total += miu_i
    h_prev = h

# Resonance frequency calculations
rad = 50e-6  # m
ro_water = 1000  # kg/m3

f_res_air = np.sqrt(D_i_total/miu_total)*3.19**2/(2*np.pi* rad**2)
f_res_water = f_res_air/np.sqrt(1+0.84*rad*ro_water/miu_total)

print(f"H_np: {H_np:.3e}")
print(f"D: {D_i_total:.3e}")
print(f"miu: {miu_total:.3e}")
print(f"f_res_air: {f_res_air:.3e}")
print(f"f_res_water: {f_res_water:.3e}")
```